Ludwig-Maximilians-University

Master Thesis:

Search for the Higgs boson in the $ZH \to l\bar{l}b\bar{b}$ channel with ATLAS at the LHC

submitted by:	submitted on:	submitted to:
Thomas Maier (#8068310)	26. September 2013	Prof. Dr. Dorothee Schaile

Ludwig-Maximilians-Universität

Master Arbeit:

Suche nach dem Higgs boson im $ZH \to l\bar{l}b\bar{b}$ Kanal mit ATLAS am LHC

abgegeben von:	abgegeben am:	eingereicht bei:
Thomas Maier (#8068310)	26. September 2013	Prof. Dr. Dorothee Schaile

Abstract

This thesis presents the search for a Higgs boson in the $ZH \to l\bar{l}b\bar{b}$ channel with data taken in 2012 by ATLAS at the LHC at a centre-of-mass energy $\sqrt{s} = 8\,\text{TeV}$, corresponding to an integrated luminosity of approximately $20.3\,\text{fb}^{-1}$. A likelihood fit is used to set an upper exclusion limit on the cross-section of a Higgs boson with mass between 110 and 150 GeV in this channel.

In addition, two studies regarding the selection of the jets used for the reconstruction of the Higgs boson are presented. The first study analyses the impact of the correction on jets coming from final state radiation in events with three jets in the signature. The second study compares the selection of anti-k_T jets, which are used in the nominal analysis, with the selection of subjets of jets reconstructed by the Cambridge-Aachen algorithm for high transverse momentum Higgs bosons.

Zusammenfassung

Die vorliegende Arbeit präsentiert die Suche nach einem Higgs Boson im $ZH \to l\bar{l}b\bar{b}$ Kanal mit Daten, die 2012 beim ATLAS Experiment am LHC bei einer Schwerpunktsenergie von $\sqrt{s} = 8\,\text{TeV}$ aufgezeichnet wurden, was einer integrierten Luminosität von $20.3\,\text{fb}^{-1}$ entspricht. Ein Likelihood Fit wird benutzt, um eine obere Ausschlussgrenze für den Wirkungsquerschnitt eines Higgs Bosons in diesem Kanal mit einer Masse zwischen 110 und 150 GeV zu setzen.

Zusätzlich werden zwei Studien bezüglich der Selektion der Jets, die für die Rekonstruktion des Higgs Bosons verwendet werden, vorgestellt. Die erste Studie befasst sich mit den Auswirkungen einer Korrektur auf Jets, die aus Endzustandsstrahlung in Ereignissen mit drei Jets in der Signatur kommen. Die zweite Studie vergleicht die Selektion von anti-k_T Jets, die in der nominellen Analyse verwendet werden, mit der Selektion von Sub-Jets aus Jets, die durch den Cambridge-Aachen Algorithmus rekonstruiert werden, für Higgs Bosonen mit hohem transversalen Impuls.

Contents

Chapter 1

Preface

Ever since the discovery of a new boson on the 4th of July 2012, which is very likely the Higgs boson predicted by the Standard Model (SM) (see Section 2.1), great efforts have been and are put into determining the properties of said new particle. Although this discovery was a very big accomplishment for the ATLAS and CMS collaborations, it was merely the start of determining if this new boson is indeed a Standard Model Higgs boson or if it belongs to a larger theory beyond the Standard Model.

The decay channels which contributed to the discovery ($H \to \gamma\gamma$, $H \to ZZ^* \to 4l$ and $H \to WW^* \to l\nu l\nu$) already allowed to determine the new particle to be a neutral boson and discard the spin-1 hypothesis. After this discovery it is important to also observe a significant evidence of the Higgs boson in other decay channels to further ascertain its properties. Especially interesting for the Higgs research at the LHC are the decays of the Higgs boson into fermions, since the direct coupling of the Higgs boson to fermions has not yet been observed significantly neither at the ATLAS nor the CMS experiment. Apart from the channels in which the Higgs boson decays to two taus, the most promising channels in this regard are the ones in which the Higgs boson decays into a $b\bar{b}$-pair. This holds especially for the production of a Higgs boson in association with a $t\bar{t}$-pair or a vectorboson (see Section 2.3). The latter is the channel which is the subject of this thesis, more specifically the associated production with a Z boson which decays into two leptons.

In the following sections the theory of the Standard Model and the Higgs boson will be explained in detail and the research at the LHC will be pictured with the ATLAS experiment. For this the design of the detector and the methods to reconstruct particles, which are produced in the collision of two high energy protons, will be described. Further on in the second part of this thesis the studies regarding the search of a Higgs boson in associated production with a Z boson decaying into a lepton- and $b\bar{b}$-pair will be presented. The full data recorded in 2012 by ATLAS at a centre-of-mass energy of $\sqrt{s} = 8$ TeV, corresponding to an

integrated luminosity of 20.3 fb^{-1}, is used for this search.

Chapter 2

Introduction

In this chapter the theoretical fundamentals for understanding elementary particles will be described. In this context the emphasis will be placed on explaining the Standard Model of particle physics (Section 2.1), with its particles (Section 2.1.1) and fundamental interactions (Sections 2.1.4, 2.1.5 and 2.1.6), going to the problem of particle masses which one encounters within this theory, and describing how this problem is solved by introducing the Higgs mechanism (Section 2.2.2). Then an overview of the most important production and decay channels for a Standard Model Higgs boson is given (Section 2.3), with the focus on the channel relevant for this thesis and its backgrounds.

2.1 The Standard Model of Particle Physics

The Standard Model of particle physics [1, 2], of which today's version was mainly developed since the 1970s, marks a still ongoing success story and is able to describe almost all fundamental phenomena of the material world. Starting from just describing and categorising new particles observed in nature in the early 20th century, new theories and methods, like the Eightfold Way by Murray Gell-Mann in 1961, allowed to also make predictions on new particles and their properties long before they could be measured in an experiment. But also the fundamental interactions of particles, strong, electromagnetic and weak, are very well described by the Standard Model. Every new discovered particle predicted by the Standard Model enhanced the validity of this theory, with the most recent (and probably the most popular) one being the Higgs boson in 2012.

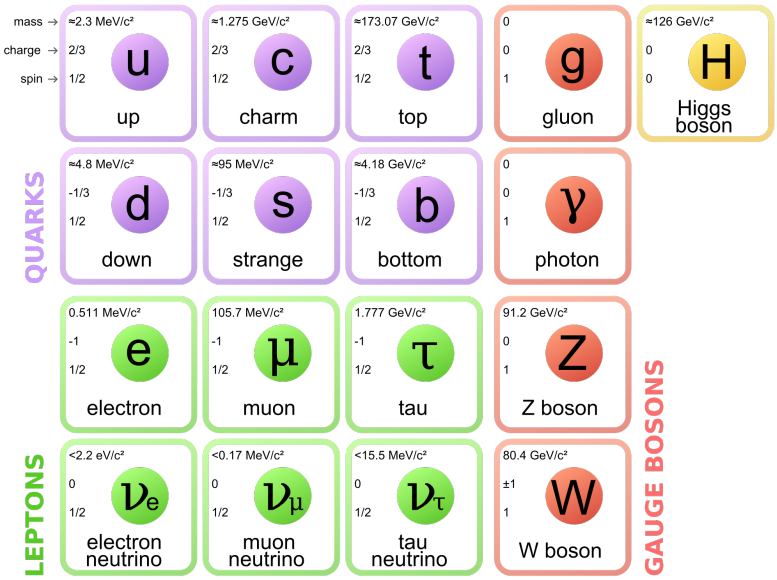

Figure 2.1: Elementary particles in the Standard Model of particle physics [3].

2.1.1 Elementary Particles

The most elementary of particles [1, 2] (at least to knowledge up to the present day) are the leptons and the quarks, which can be divided in three generations. For the leptons it can be distinguished between six leptons according to their lepton flavour and electric charge, resulting in electrons, muons and taus (with charge -1) and their respective neutrinos (with charge 0). In a similar way quarks are discriminated by their charge and flavours, being the up and down quark, the charm and strange quark, and the top and bottom quark.

Additionally to the leptons, the Standard Model also contains elementary bosons originating from the fundamental interactions which are described in more detail in Section 2.1.5, 2.1.6 and 2.2. The description of electroweak interactions gives rise to four spin-1 vectorbosons (Z, W^+, W^-, and the photon) and, with the addition of the Higgs field, one extra scalar (spin-0) Higgs boson. Finally, eight additional bosons originate from strong interactions (gluons).

Every particle also has its respective anti-particle, possessing the same features as its counterpart but having a reversed charge and reversed charge-like quantum numbers. This leads to a total of 12 leptons, 36 quarks (considering that each quark has one of three different colour flavours), 12 mediators (the vectorbosons), and one Higgs boson. An overview of the elementary particles in the Standard Model can be seen in Fig. 2.1.

Particles in general are divided into integral (bosons) and half-integral (fermions) spin particles. Leptons and quarks, by being spin-$\frac{1}{2}$ particles, belong to the lat-

ter while vectorbosons and the Higgs boson (as the name already indicates) belong to the former. In addition to the (presumably) indivisible elementary particles the Standard Model also describes those, which are bound states of quarks. Baryons contain three quarks (or three anti-quarks) and belong to the fermions while mesons contain a quark-anti-quark-pair and belong to the bosons.

2.1.2 Symmetries

A very important method in physics to understand processes without exactly knowing the underlying details is to use symmetries. Emmy Noether made a very important statement in this regard in 1917, when she published her theorem about symmetries and conservation laws [1]. It says, that every symmetry yields a respective conservation law and vice versa.

An easy example would be rotational symmetry, which corresponds to conservation of angular momentum. This manifests itself in the motion of the planets in our solar system. Since they all move on an elliptical trajectory around the sun (conservation of angular momentum), it can be deduced that the gravitational field of the sun has to be symmetric under rotation.

An easy way to describe symmetry in a mathematical way, is to define an operation, which, by applying it to a system, leaves this system invariant. So if a planet is rotated around the sun it will be affected by the same gravitational force as before, due to the symmetry of the suns gravitational field. A set of multiple symmetry operations must have the properties of a mathematical group.

These sets of symmetry operations are called symmetry groups. These groups can be represented by matrices, which apply the respective symmetry operations to a system (see Section 2.1.4). In physics the most used groups are $U(n)$ (represented by unitary $n \times n$ matrices) and $SU(n)$ (represented by unitary $n \times n$ matrices with determinant one). Looking again at the example of rotational symmetry described before, the associated symmetry group would be $SO(3)$ (the same as $SU(n)$ but only containing real matrices). This symmetry not only describes the motion of planets in our solar system but is also almost identical to an $SU(2)$ symmetry, which incidentally is the symmetry which describes the spin of particles. So the symmetry underlying the planetary motions is almost the same as for the spin of particles and (as shown later on) also describes weak interactions in particle physics. In fact a new quantum number is introduced later on similar to the spin, called "isospin", which describes different flavour states of particles. Further on the colour symmetry of strong interactions is represented by an $SU(3)$ (see Section 2.1.5) and the symmetry for electromagnetic interactions by a $U(1)$ group.

For every symmetry group there is a set of non-reducible members which can generate every member of this group, called generators [4]. As an example for an

$SU(2)$ symmetry the generators are

$$T^i = \frac{1}{2}\tau^i; \quad (i = 1, 2, 3), \tag{2.1}$$

with τ^i being the Pauli matrices (2.12).

2.1.3 Quantum Field Theory

Another important method for understanding particle physics is the description of physical processes in a relativistic field theory [1]. In this theory a particle is not described as a discrete object with its space coordinates dependent on time ($x(t)$, $y(t)$, $z(t)$), but rather by one or more fields, which are parametrised by space-time coordinates ($\phi_i(x, y, z, t)$).

A convenient way to describe the behaviour of classical particles is the Lagrangian formalism. The Lagrangian L (which is a function of x, y and z, or q_i with i = 1,2,3 , and their derivatives w.r.t. time t) itself is constructed by subtracting the potential from the kinetic energy of a certain system:

$$L = T - U. \tag{2.2}$$

The equation of motion of this system then can be derived with the Euler-Lagrange-equation:

$$\frac{d}{dt}\left(\frac{\partial L}{\partial \dot{q}_i}\right) = \frac{\partial L}{\partial q_i}; \quad (i = 1, 2, 3). \tag{2.3}$$

Similar to classical mechanics a Lagrangian (or technically a Lagrangian density) $\mathcal{L}$ can be constructed, which is a function of the fields ϕ_i and their x, y, z and t derivatives. The Euler-Lagrange-equation then has the form[1]

$$\partial_\mu\left(\frac{\partial \mathcal{L}}{\partial(\partial_\mu \phi_i)}\right) = \frac{\partial \mathcal{L}}{\partial \phi_i}; \quad (i = 1, 2, 3, ...). \tag{2.4}$$

In this a convenient shortened notation for the derivatives w.r.t. x, y, z and t was used:

$$\partial_\mu \phi_i \equiv \frac{\partial \phi_i}{\partial x^\mu}; \quad (\mu = 1, 2, 3, 4). \tag{2.5}$$

In the following three different Lagrangians will be introduced, which describe different types of particles according to their spin.

[1] Greek letter indices denote a Lorentz four-vector.

Klein-Gordon Lagrangian for a Scalar (Spin-0) Field:
Considering a single scalar field ϕ, the Lagrangian is[2]

$$\mathcal{L} = \frac{1}{2}\left(\partial_\mu \phi\right)\left(\partial^\mu \phi\right) - \frac{1}{2}m^2\phi^2, \tag{2.6}$$

and the respective equation of motion

$$\partial_\mu \partial^\mu \phi + m^2 \phi = 0, \tag{2.7}$$

which is called Klein-Gordon equation.

Dirac Lagrangian for a Spinor (Spin-$\frac{1}{2}$) Field:
Considering a spinor field ψ describing a spin-$\frac{1}{2}$ particle, the Lagrangian is[3]

$$\mathcal{L} = i\overline{\psi}\gamma^\mu \partial_\mu \psi - m\overline{\psi}\psi, \tag{2.8}$$

with the equation of motion being the Dirac equation

$$i\gamma^\mu \partial_\mu \psi - m\psi = 0, \tag{2.9}$$

where γ^μ are the four Dirac γ-matrices[4]

$$\gamma^\mu \equiv (\beta, \beta\boldsymbol{\alpha}); \quad (\mu = 0, 1, 2, 3). \tag{2.10}$$

The matrices β and $\boldsymbol{\alpha}$ have the form

$$\boldsymbol{\alpha} = \begin{pmatrix} 0 & \boldsymbol{\sigma} \\ \boldsymbol{\sigma} & 0 \end{pmatrix}, \quad \beta = \begin{pmatrix} I & 0 \\ 0 & -I \end{pmatrix}, \tag{2.11}$$

where I is the unit 2×2 matrix and $\boldsymbol{\sigma}$ are the Pauli matrices:

$$\sigma_1 = \begin{pmatrix} 0 & 1 \\ 1 & 0 \end{pmatrix}, \quad \sigma_2 = \begin{pmatrix} 0 & -i \\ i & 0 \end{pmatrix}, \quad \sigma_3 = \begin{pmatrix} 1 & 0 \\ 0 & -1 \end{pmatrix} \tag{2.12}$$

Proca Lagrangian for a Vector (Spin-1) Field:
Finally, if a spin-1 vector field A^μ is considered, the Lagrangian is

$$\mathcal{L} = -\frac{1}{4}F^{\mu\nu}F_{\mu\nu} + \frac{1}{2}m^2 A^\nu A_\nu, \tag{2.13}$$

[2]Formulas are given in "natural" (or Heaviside-Lorentz) units where $\hbar$ and c are set to 1.
[3]$\overline{\psi} = \psi^\dagger \gamma^0$
[4]Vectors, which are not Lorentz four-vectors, are indicated by being in **boldface**.

with

$$F^{\mu\nu} \equiv \partial^\mu A^\nu - \partial^\nu A^\mu \tag{2.14}$$

and the equation of motion is known as the Proca equation

$$\partial_\mu F^{\mu\nu} + m^2 A^\nu = 0. \tag{2.15}$$

It should be noted that, in contrast to classical mechanics where the Lagrangian is derived from the kinematic and potential energies of a system, the Lagrangians in a field theory are constructed to satisfy certain properties and are taken as axiomatic. The equations shown in this section describe classical fields as well as quantum ones. The main difference between the classical and the quantum theory case is the interpretation of the different parts of the Lagrangian. In quantum theory the fields are quantised and particles are interpreted as quanta of their associated fields.

In particle physics the properties of processes can be determined by deriving the impact of interactions of particles in a perturbation theory, which leads to the definition of Feynman rules [1, 5]. In this context these rules define how the different terms in the Lagrangian contribute to the calculation of interaction properties, like the decay width Γ or the cross section σ.

The following sections will show how the different fundamental interactions in the SM can be described by a QFT as pictured in this section.

2.1.4 Quantum Electrodynamics

Quantum electrodynamics (QED) [1, 5] is a quantum field theory describing the interactions of electrically charged particles. A very basic electromagnetic interaction of charged fermions, mediated by a photon, can be seen in Fig. 2.2[5]. This describes for example scattering of an electron with another charged fermion or, by switching the direction in time, annihilation of an electron-positron-pair into a (here virtual) photon, which then splits again into another fermion-anti-fermion-pair. The strength of the interaction is given by the coupling constant

$$g_e = \sqrt{4\pi\alpha}, \tag{2.16}$$

which is equal to the elementary charge e (in Heaviside-Lorentz units $\alpha = \frac{e^2}{4\pi} = \frac{1}{137}$).

As stated in Section 2.1.3 the Dirac equation (2.9) describes the behaviour of spin-$\frac{1}{2}$ particles ψ. Here ψ is a Dirac spinor with four components but is explicitly not a Lorentz four-vector.

[5]Time propagation axis points to the right.

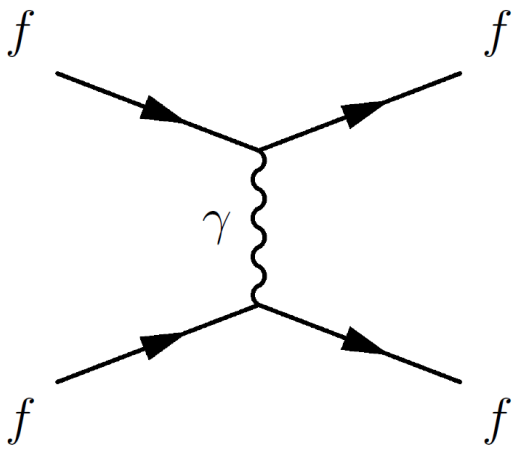

Figure 2.2: Feynman diagram of an electromagnetic interaction.

Four Dirac spinors can be found, which solve the Dirac equation. These can be further merged into two different solutions (each with a spin up and spin down component). One solution represents a state with positive energy, the other one with negative energy. Since physical particles cannot have negative energies, the negative energy solution for a particle is instead interpreted as a solution for an anti-particle with positive energy. Mathematically the sign of the energy and momentum in the negative energy solution is inverted, to get an expression of the anti-particle solutions in its physical energy and momentum.

A convenient way to introduce the coupling of fermions to the photon is to demand local gauge invariance [1, 5] of the Dirac Lagrangian (2.8). It can be easily seen that the Lagrangian (2.8) is invariant under a $U(1)$ global transformation (or symmetry transformation in $U(1)$, see Section 2.1.2)

$$\psi \to U\psi = e^{i\alpha}\psi. \tag{2.17}$$

But if the transformation is made local, it is dependent on the space-time coordinates:

$$\psi \to U\psi = e^{i\alpha(x)Q}\psi. \tag{2.18}$$

The matrix U is a 1×1 unitary matrix with a space-time dependent component $\alpha(x)$ and the charge operator Q as generator of the $U(1)_{em}$ group, which gives the electromagnetic charge of fermions (e.g. -1 for an electron). Upon applying this transformation on the Lagrangian it adds an additional term

$$\mathcal{L} \to \mathcal{L} - (\overline{\psi}\gamma^\mu Q\psi)\partial_\mu\alpha. \tag{2.19}$$

To compensate this difference in the Lagrangian, an extra term has to be added

$$\mathcal{L} = \left[i\overline{\psi}\gamma^\mu\partial_\mu\psi - m\overline{\psi}\psi\right] - g_e\left(\overline{\psi}\gamma^\mu Q\psi\right)A_\mu, \tag{2.20}$$

with the electromagnetic coupling constant g_e (2.16) and A_μ being a new vector field, which transforms under local gauge transformation as

$$A_\mu \to A_\mu - \frac{1}{g_e}\partial_\mu \alpha. \tag{2.21}$$

In QED, A_μ is the electromagnetic field vector, but in context of particle physics it can be interpreted as a vectorboson. The new form of the Lagrangian (2.20) is invariant under local gauge transformation of ψ (2.18), if the boson A_μ transforms according to (2.21). Since every particle needs a term in the Lagrangian which describes its free propagation, the Proca Lagrangian for a free boson (2.13) has to be added. The term $F^{\mu\nu}$ (2.14) is invariant under the transformation (2.21), but $A^\nu A_\nu$ is not. So to preserve local gauge invariance the boson has to be massless. This applies for the photon and also the gluons later on, but becomes a problem when handling vector bosons in weak interactions.

The Lagrangian describing the interaction of fermions with a massless vector field A^μ is then

$$\mathcal{L} = \left[i\overline{\psi}\gamma^\mu\partial_\mu\psi - m\overline{\psi}\psi\right] - \frac{1}{4}F^{\mu\nu}F_{\mu\nu} - g_e\left(\overline{\psi}\gamma^\mu Q\psi\right)A_\mu, \tag{2.22}$$

where the last term describes the coupling of a boson to a fermion. A convenient way to include the coupling to a boson into the free Lagrangian of the fermion, is to replace ∂_μ with the "covariant derivative" $\mathcal{D}_\mu$:

$$\mathcal{D}_\mu \equiv \partial_\mu + ig_e Q A_\mu. \tag{2.23}$$

2.1.5 Quantum Chromodynamics

In the last section it was shown how QED describes the interaction of charged particles and how the photon arises naturally when the formalism of a $U(1)_{em}$ gauge theory is applied. This section will introduce similarly the interaction of coloured particles in form of quantum chromodynamics (QCD) [1, 5].

In QED the interaction of particles is mediated by the photon and the strength of the interaction is given by the coupling constant g_e (2.16). In the same way a strong coupling constant can be defined

$$g_s = \sqrt{4\pi\alpha_s}, \tag{2.24}$$

which gives the strength of interactions in QCD, and the mediators are the gluons. Quarks can have three different colours, "red" (r), "blue" (b) and "green" (g). In QCD, just like in QED, the relevant quantity for interactions is the (colour) charge of the particles, whereas the different flavours of the quarks are irrelevant (except in form of their masses).

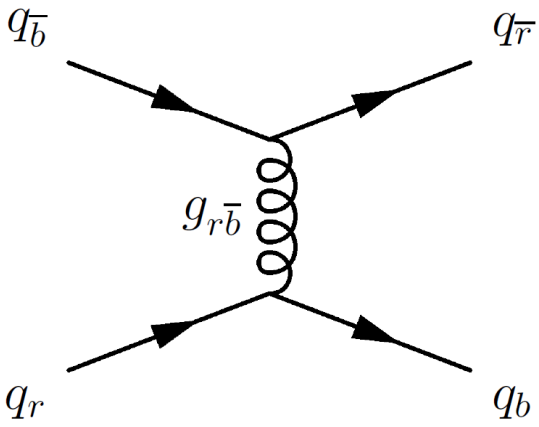

Figure 2.3: Feynman diagram of a strong interaction.

A typical strong interaction can be seen in Fig. 2.3, where the gluon carries the difference of the quarks colour before and after a quark-gluon-vertex. Thus gluons always carry a colour and an anti-colour. This in principle would allow for nine combinations of colours ($r\overline{r}$, $r\overline{b}$, $r\overline{g}$, $b\overline{r}$, $b\overline{b}$, $b\overline{g}$, $g\overline{r}$, $g\overline{b}$ and $g\overline{g}$) and thus nine different gluons. But, as already stated in Section 2.1.2, the underlying symmetry for the colour flavour is an $SU(3)$ symmetry. So the nine possible states actually constitute a "colour octet" and one "colour singlet", which is colourless.

Technically all these different colour states are possible. But actually in nature a coloured quark or gluon has never been observed outside of its bound states with other particles. Thus quarks can only exist in their bound form of hadrons. This leads to a rule called "confinement", which states that coloured particles (quarks and gluons) are confined in colourless hadrons. But the colour singlet state is colourless and thus would have to appear in nature as an observable particle. Actually, since gluons, like photons, have no mass there would be a long-range force with strong coupling. The strong force, however, has only been observed acting on very short range, which empirically forbids the existence of a colour singlet gluon. By hadronisation, high energy quarks or gluons create hadronic showers, which can be detected as jets of particles in a detector.

The strong coupling of quarks can be described in a similar way as in Section 2.1.4 with local gauge invariance of a three particle Lagrangian to account for the three different colours. If the three different colour states of the same fermion are assumed to have the same mass and the spinor ψ is written as

$$\psi \equiv \begin{pmatrix} \psi_r \\ \psi_b \\ \psi_g \end{pmatrix}, \tag{2.25}$$

then the Lagrangian has the same form as the one for a single particle (2.8). Analog to $U(1)$ an $SU(3)$ local gauge transformation of the form

$$\psi \to U\psi = e^{i\boldsymbol{\alpha}(x)\boldsymbol{T}}\psi \tag{2.26}$$

can be applied. The matrix U is a 3×3 unitary matrix parametrised by the generators of the $SU(3)$ group $\boldsymbol{T}$ (which contains a vector of Gell-Mann matrices $\boldsymbol{\lambda}$, analog to the Pauli matrices for $SU(2)$ (2.1)) and group parameters $\boldsymbol{\alpha}(x)$. As in Section 2.1.4 the coupling of gauge bosons $\boldsymbol{G}_\mu$ to fermions can be introduced by replacing the derivative ∂_μ by the covariant derivative $\mathcal{D}_\mu$:

$$\mathcal{D}_\mu \equiv \partial_\mu + ig_s\boldsymbol{T} \cdot \boldsymbol{G}_\mu. \tag{2.27}$$

A transformation rule for $\boldsymbol{G}_\mu$ can be found similar to (2.21) for which the Lagrangian stays invariant under applying (2.26). But since $SU(3)$, in contrast to $U(1)$, is a non-abelian group (meaning members of the group do not commute), an additional term has to be added. The transformation then is

$$\boldsymbol{G}_\mu \to \boldsymbol{G}_\mu - \frac{1}{g_s}\partial_\mu\boldsymbol{\alpha} - (\boldsymbol{\alpha} \times \boldsymbol{G}_\mu)\,, \tag{2.28}$$

where the last term is the $SU(3)$ cross-product of $\boldsymbol{\alpha}$ and $\boldsymbol{G}_\mu$. The modified Lagrangian is invariant under $SU(3)$ local gauge transformation. Adding the terms for massless free spin-1 particles we get the Lagrangian for QCD:

$$\mathcal{L} = i\overline{\psi}\gamma^\mu\partial_\mu\psi - m\overline{\psi}\psi - \frac{1}{4}\boldsymbol{G}^{\mu\nu} \cdot \boldsymbol{G}_{\mu\nu} - g_s\left(\overline{\psi}\gamma^\mu\boldsymbol{T}\psi\right) \cdot \boldsymbol{G}_\mu. \tag{2.29}$$

Analog to $F^{\mu\nu}$ (2.14), $\boldsymbol{G}^{\mu\nu}$ is defined as

$$\boldsymbol{G}_{\mu\nu} = \partial_\mu\boldsymbol{G}_\nu - \partial_\nu\boldsymbol{G}_\mu - g_s\left(\boldsymbol{G}_\mu \times \boldsymbol{G}_\nu\right). \tag{2.30}$$

2.1.6 Electroweak Interactions

The third interaction in the SM describes the coupling of weakly charged particles to the mediators of weak interactions [1, 5], the Z, W^+ and W^- boson. A basic weak process can be seen in Fig. 2.4. Like in QED, this can be seen as scattering of a charged lepton with another weakly charged particle, producing a neutrino under exchange of a W, or as annihilation of a neutrino and a lepton to a W, which then splits again into a pair of weakly charged fermions. The coupling strengths of Z and $W^\pm$ are given by

$$\begin{aligned} g_W &= \frac{g_e}{\sin\theta_w} \\ g_Z &= \frac{g_e}{\sin\theta_w\cos\theta_w} \end{aligned}, \tag{2.31}$$

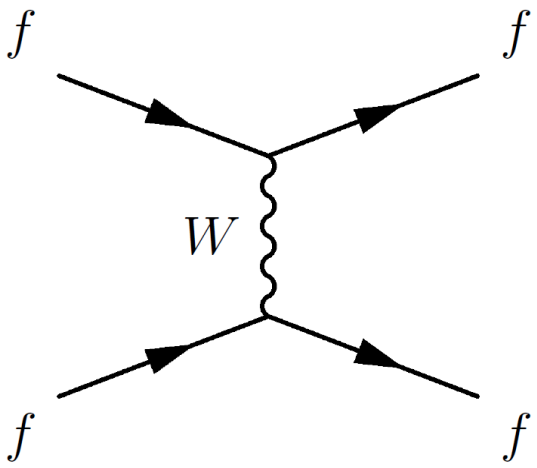

Figure 2.4: Feynman diagram of a weak interaction.

with the "weak mixing" or Weinberg angle θ_w.

Weak interactions for quarks are not flavour conserving, thus an interaction as in Fig. 2.5 is possible. This can be described as interactions of weak eigenstates of the down-like quarks, so that three quark generations of weak interactions can be defined

$$\begin{pmatrix} u \\ d' \end{pmatrix}, \begin{pmatrix} c \\ s' \end{pmatrix}, \begin{pmatrix} t \\ b' \end{pmatrix}, \tag{2.32}$$

where the weak eigenstates and the mass eigenstates of the down-like quarks are related by the Cabibbo-Kobayashi-Maskawa matrix:

$$\begin{pmatrix} d' \\ s' \\ b' \end{pmatrix}_{weak} = \begin{pmatrix} V_{ud} & V_{us} & V_{ub} \\ V_{cd} & V_{cs} & V_{cb} \\ V_{td} & V_{ts} & V_{tb} \end{pmatrix} \begin{pmatrix} d \\ s \\ b \end{pmatrix}_{mass} = V_{CKM} \begin{pmatrix} d \\ s \\ b \end{pmatrix}_{mass} . \tag{2.33}$$

Here each element of the matrix specifies the coupling of the quarks indicated in the index.

Another important property of weak interactions is that they are not invariant under parity transformation (mirror symmetry). This implies additional properties for leptons or fermions in general. When looking at the helicity of a particle (orientation of the spin relative to the direction of motion) a very fundamental observation can be made:

ALL NEUTRINOS ARE LEFT-HANDED, WHILE ALL ANTINEUTRINOS ARE RIGHT-HANDED.

Right-handed means the spin is parallel to the direction of motion and left-handed means it is anti-parallel. In general this rule is true for all fermions in weak interactions. But since only neutrinos are (presumably) massless, this absolute form

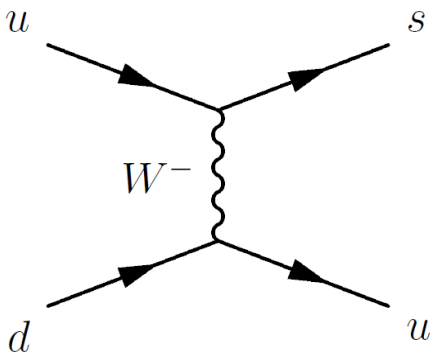

Figure 2.5: Feynman diagram of a weak interaction where flavour of the quarks is not conserved.

only applies to them. For massive fermions the helicity is not Lorentz-invariant. This means that an observer could always find a frame, which travels faster than the fermion. This would lead to a flip of the helicity, thus changing a right-handed fermion into a left-handed one (and vice versa).

To account for the maximal violation of parity symmetry in weak interactions, fermionic fields are written as

$$f_{L,R} = \frac{1}{2}\left(1 \mp \gamma_5\right) f, \tag{2.34}$$

with f being the fermion spinor. The matrix γ_5 is a product of the gamma matrices (2.10):

$$\gamma_5 \equiv i\gamma_0\gamma_1\gamma_2\gamma_3 = \begin{pmatrix} 0 & I \\ I & 0 \end{pmatrix}. \tag{2.35}$$

The spinors $f_{L,R}$ are the "chiral" states of the fermions which are labeled, like helicity, left-handed and right-handed. Although these two quantities are the same for relativistic cases, where mass is negligible, this does not hold in general. Chirality describes a certain state of a particle while helicity only describes the orientation of its spin relative to its momentum (which is, as already stated before, explicitly not Lorentz-invariant).

In a similar way to the spin of a particle the weak isospin defines different weak flavour states of particles. The third component of the weak isospin for left-handed fermions is $I_L^3 = \pm\frac{1}{2}$ and for right-handed fermions $I_R^3 = 0$. This yields three generations of left-handed and right-handed leptons and quarks, with the left-handed fermions being in weak isodoublets and the right-handed fermions in

weak isosinglets:

$$\begin{aligned} \chi_L &= \begin{pmatrix} \nu_l \\ l^- \end{pmatrix}_L, \ \psi_R = l_R^-, \nu_{R,l}; \quad \text{for } l = e, \mu, \tau \\ \chi_L &= \begin{pmatrix} u \\ d \end{pmatrix}_L, \ \psi_R = u_R, d_R; \quad \text{for } u/d = u/d, c/s, t/b \end{aligned} . \tag{2.36}$$

Neutrinos technically have right-handed states, though would be unobservable if they are massless.

The difference in weak coupling to left- and right-handed fermions requires a more specific treatment of weak interactions in terms of a gauge theory than just an $SU(2)$ copy of the Lagrangian derived in QCD (see Section 2.1.5). In fact it was shown by Weinberg and Salam that weak and electromagnetic interactions can be treated in one unified $SU(2)_L \otimes U(1)_Y$ symmetry. This introduces three gauge bosons $\boldsymbol{W}^\mu$ from an $SU(2)$ treatment equivalent to the one done for QCD and one boson B^μ from the $U(1)$ symmetry with coupling to the hypercharge Y (in contrast to the electromagnetic charge Q in Section 2.1.4). The hypercharge is defined as

$$Y = 2Q - 2I^3. \tag{2.37}$$

Since $\boldsymbol{W}^\mu$ only couple to left-handed fermions but B^μ couples to left-handed fermions as well as to right-handed ones, their respective local gauge transformations are different:

$$\begin{aligned} \chi_L &\to e^{i(\boldsymbol{\alpha}(x)\cdot\boldsymbol{T}+\beta(x)Y)}\chi_L \\ \psi_R &\to e^{i\beta(x)Y}\psi_R \end{aligned} . \tag{2.38}$$

Here $\boldsymbol{T}$ are the generators of an $SU(2)_L$ group (2.1), which return $T = \frac{1}{2}$ for left-handed and $T = 0$ for right-handed fermions. The hypercharge Y (2.37) is the generator of a $U(1)_Y$ group. The covariant derivative for the electroweak gauge theory then has the form

$$\mathcal{D}_\mu = \partial_\mu + \frac{i}{2}\left(g\boldsymbol{\tau}\cdot\boldsymbol{W}_\mu + g'YB_\mu\right), \tag{2.39}$$

where $\boldsymbol{W}_\mu$ and B_μ behave like

$$\begin{aligned} \boldsymbol{W}_\mu &\to \boldsymbol{W}_\mu - \frac{1}{g}\partial_\mu\boldsymbol{\alpha} - (\boldsymbol{\alpha}\times\boldsymbol{W}_\mu) \\ B_\mu &\to B_\mu - \frac{2}{g'}\partial_\mu\beta \end{aligned} \tag{2.40}$$

under local gauge transformation. The coupling constants g and g' are fixed by the elementary charge e and the weak mixing angle θ_w:

$$e = g\ \sin\theta_w = g'\ \sin\theta_w. \tag{2.41}$$

The Lagrangian for electroweak interactions then has the form

$$\begin{aligned}\mathcal{L} = & i\overline{\chi}_L\gamma^\mu\left[\partial_\mu + \frac{i}{2}\left(g\boldsymbol{\tau}\cdot\boldsymbol{W}_\mu + g'YB_\mu\right)\right]\chi_L \\ & + i\overline{\psi}_R\gamma^\mu\left[\partial_\mu + \frac{i}{2}g'YB_\mu\right]\psi_R - \frac{1}{4}\boldsymbol{W}_{\mu\nu}\boldsymbol{W}^{\mu\nu} - \frac{1}{4}B_{\mu\nu}B^{\mu\nu}\end{aligned}. \tag{2.42}$$

The observable vectorbosons Z, $\mathrm{W}^\pm$, and the photon are mixed states of the bosons B_μ and $\boldsymbol{W}_\mu$, which is shown in the context of the Higgs mechanism in Section 2.2.2.

As already mentioned in Section 2.1.4 and 2.1.5 the mass terms for the bosons are not invariant under local gauge transformation so that they have to be assumed massless. But also a mass term for the fermions,

$$\begin{aligned}-m_f\overline{f}f &= -m_f\overline{f}\left[\frac{1}{2}\left(1-\gamma^5\right) + \frac{1}{2}\left(1+\gamma^5\right)\right]f \\ &= -m_f\left(\overline{f}_R f_L + \overline{f}_L f_R\right)\end{aligned}, \tag{2.43}$$

would not be invariant since left- and right-handed fermions transform differently (2.38). But even more crucial than the fact that mass terms for the gauge bosons or fermions are not invariant under local gauge transformation, is that the approach of implementing the mass terms by hand makes this theory unrenormalisable. In particle physics divergences appear when treating theories in higher orders of perturbation theory, which can be compensated if the theories are renormalisable. Thus a theory which is not renormalisable is actually meaningless for particle physics. So in an electroweak gauge theory the gauge bosons as well as the fermions would have to be considered massless, which obviously contradicts experimental observations. This problem of particle masses will be addressed in Section 2.2 where the Higgs mechanism is introduced.

2.2 The Higgs Boson

In the last sections it was shown how the different fundamental interactions in the Standard Model, strong and electroweak, can be described and how the mediators of these interactions emerge naturally by local gauge invariance of the Dirac Lagrangian for an $SU(3)_C \times SU(2)_L \times U(1)_Y$ symmetry. In this context a very striking problem arose concerning the masses of said mediators. They had to be set to zero to conserve local gauge invariance. While this property is easily provided by the photon and the gluons, the electroweak gauge bosons Z, W^+ , and W^- are far from massless. This is shown by experiment but also already emerged from Fermi's description of the beta decay [1], which is caused by weak force. His

approach of a point-like weak interaction fails at high energies, forcing the introduction of mediators for weak interactions, which have to have a high mass to ensure the high difference of the strength of weak interactions relative to the one of electromagnetic interactions.

This high mass for the Z, W^+ , and W^- boson contradicts the predictions made by the gauge theories described in the last sections. In the next sections a rather simple, but nonetheless brilliant method will be introduced to give massless particles a mass by coupling to a new scalar field.

2.2.1 Spontaneous Symmetry Breaking

A way to generate the mass of a particle is to reveal its "hidden properties" by "spontaneous symmetry breaking" [1, 5]. This mechanism is first explained in the context of a $U(1)$ theory and then expanded to $SU(2)$ in the next section. A Klein-Gordon Lagrangian (2.6) for a complex scalar field $\phi = (\phi_1 + i\phi_2)/\sqrt{2}$

$$\mathcal{L} = T - V = (\partial_\mu \phi)^* (\partial^\mu \phi) - \left(\mu^2 \phi^* \phi + \lambda (\phi^* \phi)^2\right) \tag{2.44}$$

can be considered, where the last two terms are the potential V for the field. If λ is demanded to be positive then there are two cases left, $\mu^2 > 0$ and $\mu^2 < 0$. The first case just gives a paraboloid which is rotational symmetric in the ϕ_1-ϕ_2-plane with the minimum at zero. But the second case yields a far more interesting behaviour. If the Lagrangian (2.44) is rewritten in terms of ϕ_1 and ϕ_2, it has the form

$$\mathcal{L} = \frac{1}{2}(\partial_\mu \phi_1)^2 + \frac{1}{2}(\partial_\mu \phi_2)^2 - \left(\frac{1}{2}\mu^2 \left(\phi_1^2 + \phi_2^2\right) + \frac{1}{4}\lambda \left(\phi_1^2 + \phi_2^2\right)^2\right). \tag{2.45}$$

The minima of the potential V in the ϕ_1-ϕ_2-plane are located on a circle with radius v, such that

$$\phi_1^2 + \phi_2^2 = v^2 \qquad \text{with} \qquad v^2 = -\frac{\mu^2}{\lambda}, \tag{2.46}$$

which can be seen in Fig. 2.6. The field ϕ can be parametrised by expansion around the ground state, which can be chosen with $\phi_1 = v$ and $\phi_2 = 0$ (any discrete point of the minima is as valid as the other without losing generality due to the rotational symmetry of V). The Lagrangian (2.45) then can be expanded with new fields η and ξ using

$$\phi_1(x) = \frac{1}{\sqrt{2}}\left[v + \eta(x) + i\xi(x)\right] \tag{2.47}$$

to get

$$\begin{aligned} \mathcal{L} = {} & \frac{1}{2}(\partial_\mu \xi)^2 + \frac{1}{2}(\partial_\mu \eta)^2 + \mu^2 \eta^2 \\ & + (\text{constant or higher order terms in } \eta \text{ and } \xi). \end{aligned} \tag{2.48}$$

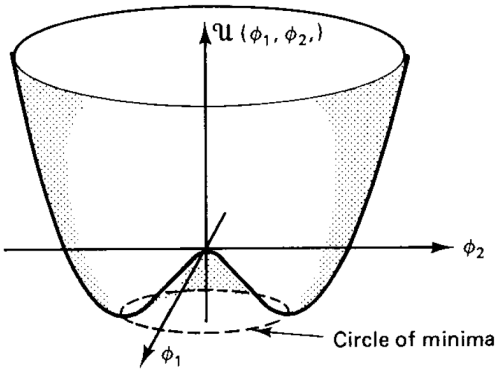

Figure 2.6: The Higgspotential [1].

The term $\mu^2\eta^2$ has the form of a mass term for the field η if the mass is $m_\eta = \sqrt{2\lambda v^2}$. As a reminder μ^2 has been set to be negative, which is the reason why in (2.44) the mass term actually has the wrong sign (it always has to have the form $(-\frac{1}{2}m^2\phi^2)$, see (2.6)), but has the correct sign in (2.48).

The Lagrangian (2.48) describes the same physical system as (2.45). The only change happened by rewriting the field in the Lagrangian in terms of fluctuations about a particular ground state. This change to a different notation gives the correct picture of physics, whereas the original one does not.

2.2.2 The Higgs Mechanism

To finally find a solution for the problem which occurred in Section 2.1.6 the last step is to combine the principle of spontaneous symmetry breaking, described in last the section, with local gauge invariance [1, 5, 6]. For the Lagrangian (2.44) to be invariant under

$$\phi \to e^{i\alpha(x)}\phi, \tag{2.49}$$

∂_μ has to be replaced, as done in Section 2.1.4, with the covariant derivative $\mathcal{D}_\mu$ (2.23) where A_μ transforms according to (2.21) under local gauge transformation. If the procedure of spontaneous symmetry breaking is applied to the new Lagrangian

$$\mathcal{L} = \left(\partial^\mu + ig_e A^\mu\right)\phi^*\left(\partial_\mu - ig_e A_\mu\right)\phi - \mu^2\phi^*\phi - \lambda\left(\phi^*\phi\right)^2 - \frac{1}{4}F_{\mu\nu}F^{\mu\nu}, \tag{2.50}$$

a new Lagrangian in terms of the field η and ξ is obtained:

$$\begin{aligned}\mathcal{L} = &\frac{1}{2}\left(\partial_\mu \xi\right)^2 + \frac{1}{2}\left(\partial_\mu \eta\right)^2 - v^2\lambda\eta^2 + \frac{1}{2}g_e^2 v^2 A_\mu A^\mu \\ &- g_e v A_\mu \partial^\mu \xi - \frac{1}{4}F_{\mu\nu}F^{\mu\nu} + (\text{interaction terms}).\end{aligned} \tag{2.51}$$

This describes a massive scalar boson η, a massless Goldstone boson ξ but, most importantly, also a massive vector boson A_μ, where the mass terms are

$$m_\xi = 0, \qquad m_\eta = \sqrt{2\lambda v^2}, \qquad m_A = g_e v.$$

So the mass for the gauge field was dynamically generated but there is still the Goldstone boson ξ in the Lagrangian. The field ϕ, however, can be written in lowest order of ξ as

$$\phi = \frac{1}{\sqrt{2}}\left(v + \eta + i\xi\right) \approx \frac{1}{\sqrt{2}}\left(v + \eta\right) e^{i\xi/v}. \tag{2.52}$$

The Lagrangian (2.51) was generated by demanding invariance under (2.49), so if α is chosen to be $\alpha(x) = -i\xi(x)/v$ then ξ is eliminated from (2.51). Renaming η to h (for obvious reasons) the Lagrangian for a spontaneously broken $U(1)$ gauge theory of a scalar field is

$$\begin{aligned}\mathcal{L} = &\frac{1}{2}\left(\partial_\mu h\right)^2 - \lambda v^2 h^2 + \frac{1}{2}g_e^2 v^2 A_\mu A^\mu - \lambda v h^3 - \frac{1}{4}\lambda h^4 \\ &+ \frac{1}{2}g_e^2 A_\mu A^\mu h^2 + v g_e^2 A_\mu A^\mu h - \frac{1}{4}F_{\mu\nu}F^{\mu\nu}\end{aligned}, \tag{2.53}$$

which describes the interaction of a massive gauge boson A_μ and a massive scalar boson h, called Higgs boson. The Goldstone boson ξ which occurs inevitably when applying spontaneous symmetry breaking has been eliminated and thus has given mass to A_μ, which is the "Higgs mechanism". The terms h^3, h^4, $A_\mu A^\mu h^2$, and $A_\mu A^\mu h$ describe the self-coupling of the Higgs boson and its coupling to the boson A_μ.

As already mentioned in Section 2.1.6 a crucial property of this theory should be that it is renormalisable, which was one of the problems of just implementing mass terms by hand. This can be shown for the Higgs theory but would vastly exceed this thesis.

If the procedure of spontaneous symmetry breaking is expanded to an $SU(2)_L \times U(1)_Y$ symmetry as treated by Weinberg and Salam (see Section 2.1.6) masses can be given to the Z, W^+ , and W^- boson while the photon stays massless. Similar to the $U(1)$ case the coupling of a doublet of complex scalar fields ϕ to the gauge

bosons is accomplished by demanding local gauge invariance while the mass terms then are generated by spontaneous symmetry breaking.

The bosons Z_μ, $W_\mu^\pm$, and photon A_μ are the mass eigenstates of the Weinberg-Salam theory. They can be written as superpositions of the bosons introduced by the electroweak gauge theory $\boldsymbol{W}_\mu$ and B_μ (see Section 2.1.6):

$$W_\mu^\pm = \frac{1}{\sqrt{2}}\left(W_\mu^1 \mp i W_\mu^2\right) \tag{2.54}$$

$$A_\mu = \cos\theta_w B_\mu + \sin\theta_w W_\mu^3 \tag{2.55}$$

$$Z_\mu = -\sin\theta_w B_\mu + \cos\theta_w W_\mu^3 \tag{2.56}$$

The mass of the W^+ and W^- boson (2.54) is then

$$M_W = \frac{1}{2} v g, \tag{2.57}$$

while the theory also yields the massless photon A_μ (2.55) and the mass of the Z boson (2.56)

$$M_Z = \frac{1}{2} v \sqrt{g^2 + g'^2}. \tag{2.58}$$

With the couplings g and g' being connected by (2.41), M_Z can be written in terms of M_W and the weak mixing angle θ_w:

$$M_Z = \frac{M_W}{\cos\theta_w}. \tag{2.59}$$

The parameter v can be derived from observation of weak interactions

$$v = \frac{1}{\sqrt{\sqrt{2} G_F}} = 246\ \mathrm{GeV}, \tag{2.60}$$

with Fermi's weak-interaction coupling constant G_F. Thus the masses of the W bosons and the Z boson can be determined to be

$$M_W = \frac{37.3\ \mathrm{GeV}}{\sin\theta_w}, \qquad M_Z = \frac{74.6\ \mathrm{GeV}}{\sin(2\theta_w)}. \tag{2.61}$$

The parameter λ is a free parameter of the theory, thus the mass of the Higgs boson has to be determined by experiment and cannot be derived from theory.
Finally, if gauge-invariant Yukawa interaction terms are introduced for the leptons (and in a similar way for the quarks)

$$\mathcal{L}_{Yukawa,l} = -\lambda_l \left[\left(\overline{\psi}_{L,l}\phi\right)\psi_{R,l} + \overline{\psi}_{R,l}\left(\phi^\dagger \psi_{L,l}\right)\right], \tag{2.62}$$

then the Higgs mechanism also provides masses for the fermions. Here ϕ is a doublet of complex scalar fields, as used before for the electroweak description of the Higgs mechanism. The mass of fermions then is

$$m_f = \frac{1}{\sqrt{2}}\lambda_f v, \tag{2.63}$$

where λ_f is the Yukawa coupling of fermions. For each fermion type in the Standard Model one Yukawa term and thus one Yukawa coupling parameter λ_f is needed. Like the mass of the Higgs boson, these coupling terms cannot be derived by theory and thus the masses of fermions are free parameter in the Standard Model, which have to be determined by experiment.

2.3 Production and Decay of the Higgs Boson and Backgrounds

In the last section the Higgs mechanism was introduced and how this mechanism gives mass to the electroweak gauge bosons as well as to fermions by the formalism of Yukawa coupling. The couplings of the Higgs boson with the massive vector-bosons and fermions in the SM determine the different possible production and decay channels of the Higgs boson. The channels, which are relevant for proton-proton-collisions at particle colliders, such as the LHC (see Section 3.1), will be discussed. Then the backgrounds which are relevant for the studies presented in Chapter 4 are introduced.

2.3.1 Higgs Signal

For a proton-proton collider the most relevant production channels [7] for a Higgs boson can be seen in Fig. 2.7, being the gluon-gluon fusion, the vectorboson-fusion, and the associated production with a vectorboson or with two top-quarks. The cross-sections σ for these production modes, depending on the mass of the Higgs boson at a centre-of-mass energy $\sqrt{s} = 8\,\text{TeV}$, can be seen in Fig. 2.8. For a Higgs boson with mass around 125 GeV the gluon-gluon-fusion is by far the most dominant production channel, followed by the vectorboson-fusion and the associated production channels.

For the discovery of a Higgs boson in 2012 [9] the relevant channels were the decay into two leptonically decaying vectorbosons (Fig. 2.9) and the decay into two photons (Fig. 2.10). Since these decays give a very good leptonic or electromagnetic signature for discrimination against the huge QCD-background they can be used in conjunction with the gluon-gluon-fusion production mode. This QCD-background,

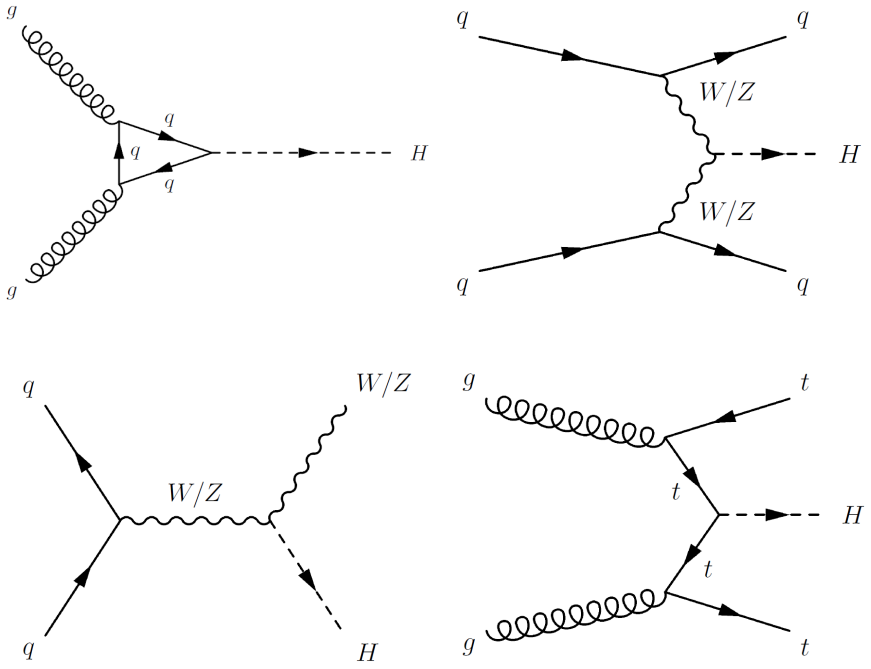

Figure 2.7: Different production processes for a Higgs boson at the LHC: gluon-gluon-fusion (top left), vectorboson-fusion (top right), associated production with a vectorboson (bottom left) and with two top-quarks (bottom right).

which is present at high energy proton-proton-collisions, mainly consists of multijet events.

Fig. 2.8 also shows the cross-sections for the different decay channels for a Higgs boson with mass between 80 and 200 GeV. For a Higgs boson with a mass of 125 GeV the most dominant channel is actually the decay into a $b\bar{b}$-pair [10]. The problem of this decay is that when used in junction with gluon-gluon-fusion, the QCD-background becomes too overwhelming, since there is no lepton in the final state to give a clean signature. An analysis for this decay mode has to use the associated production channels to get a significant discrimination of the signal from the background. The full production and decay channel, which is the subject of this thesis, is the production of the Higgs boson, decaying into two b-quarks in association with a Z boson, which decays into two electrons or muons (see Fig. 2.11). This decay mode has a lower production cross-sections than the production with a W boson, but has a cleaner signature with a better suppression of the QCD-background and the background coming from top-quark decays. The signature contains the two leptons from the Z boson decay and two jets from the showering of the b-quarks. The jets can be tagged by exploiting the long lifetime of

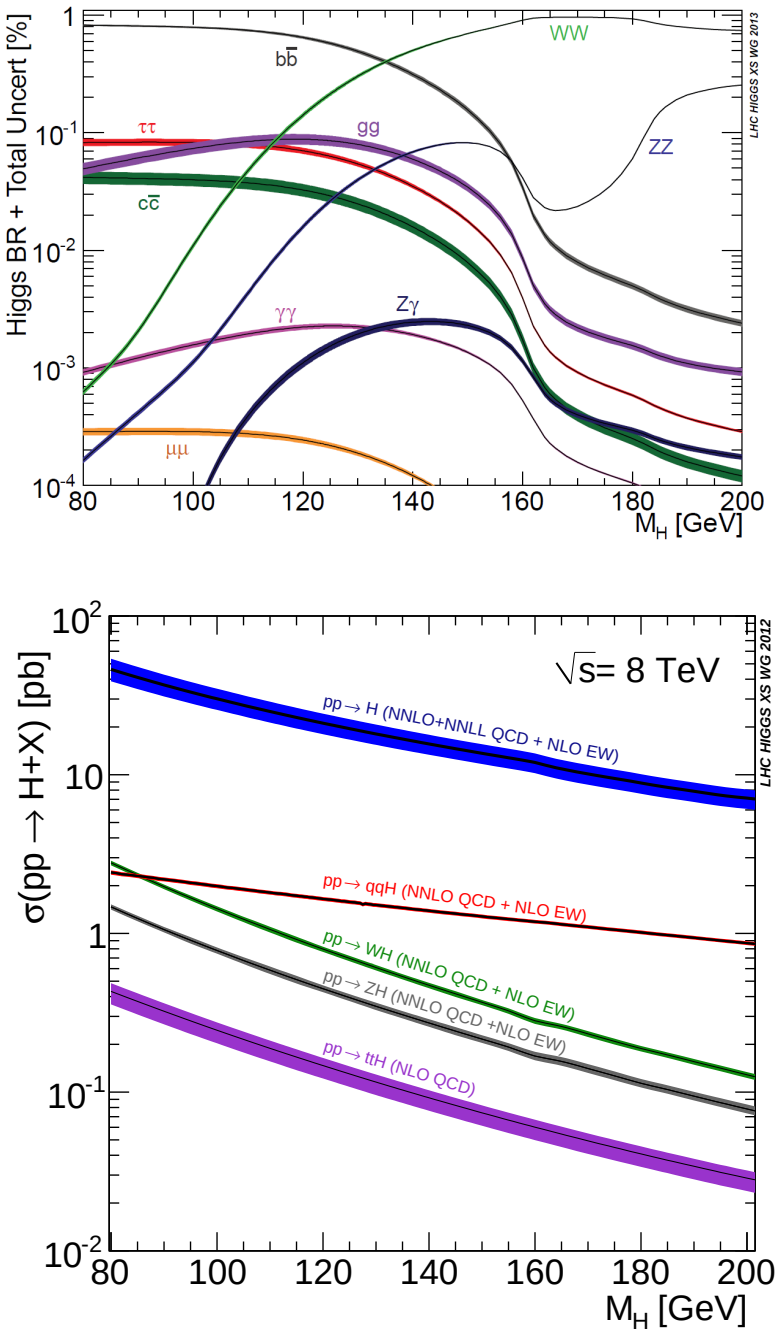

Figure 2.8: Production (bottom) and decay (top) channels for different Higgs masses (LHC Higgs Cross Section Working Group [8]).

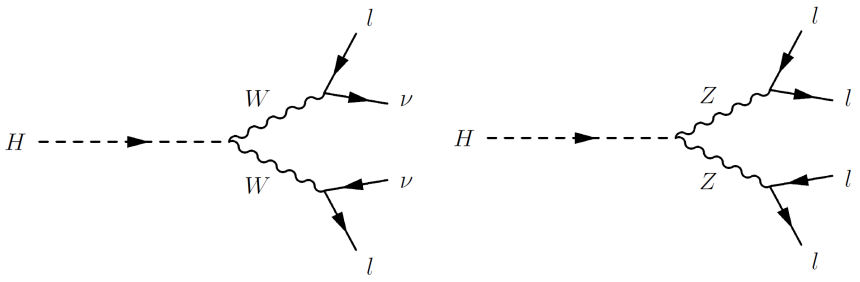

Figure 2.9: Decays of a Higgs boson into leptonically decaying W bosons (left) and Z bosons (right).

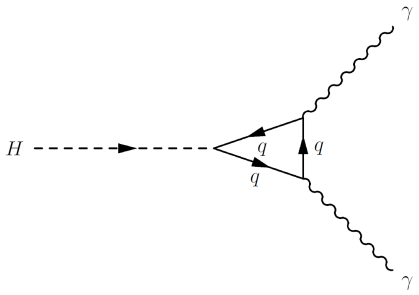

Figure 2.10: Decay of a Higgs boson into photons.

the B-hadrons (see Section 3.3.2) coming from the hadronisation of the b-quarks, which strongly suppresses Z+jets backgrounds containing jets from light quarks.

Neutrinos can only appear in the signal signature by leptonic decays of B- or C-hadrons in the jets, thus only a small missing transverse energy (see Section 3.3.5) is to be expected. This can be used to suppress QCD-background and backgrounds from top quark decays. The invariant mass of the two leptons also can be used to identify the signal, since its distribution peaks at the Z boson mass.

In the following sections the backgrounds relevant for the $ZH \rightarrow l\bar{l}b\bar{b}$ channel will be discussed in more detail.

2.3.2 Z+Jets Background

The most dominant background for a search in the ZH channel are events with a leptonically decaying Z boson in conjunction with jets. An example for this decay is given in Fig. 2.12. The jets from the gluon splitting, either jets from real b-quarks or mistagged lighter jets, are used for the Higgs boson reconstruction. Since there is a real Z boson in the decay, the signal cannot be discriminated from the background

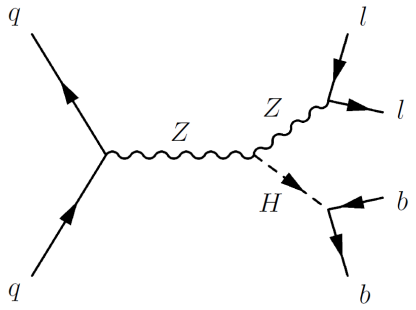

Figure 2.11: Production and decay of a Higgs boson in the ZH channel.

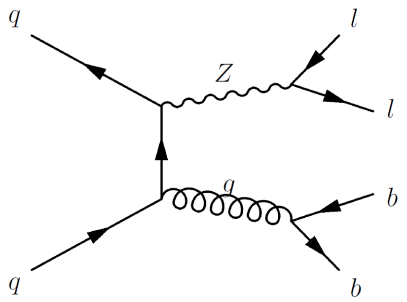

Figure 2.12: Background coming from Z+jets events.

with the invariant mass of the leptons. In addition, the lack of missing transverse energy makes this background almost identical to the signal. One variable, which can be used for suppression of the Z+jets background, is the distance ΔR (see Section 3.2.1) between the two selected jets used for the reconstruction of the Higgs boson. Since the jets in the signal decay come from the massive Higgs boson, they will be less collimated than the jets coming from the gluon splitting. Additionally, as already mentioned in Section 2.3.1, b-tagging suppresses the huge background contributions coming from Z+jets events containing jets from hadronisation of light quarks.

2.3.3 Top Background

An example for the background coming from $t\bar{t}$ events can be seen in Fig. 2.13. Top quarks decay into a W boson and a b-quark with a probability of almost 100%. A decay of two top quarks provides the two b-quarks for the Higgs boson reconstruction. If the W bosons decay leptonically the signature also contains two leptons which can misinterpreted as a Z boson. Since there are also two neutrinos in the signature, however, a significant amount of missing transverse energy is

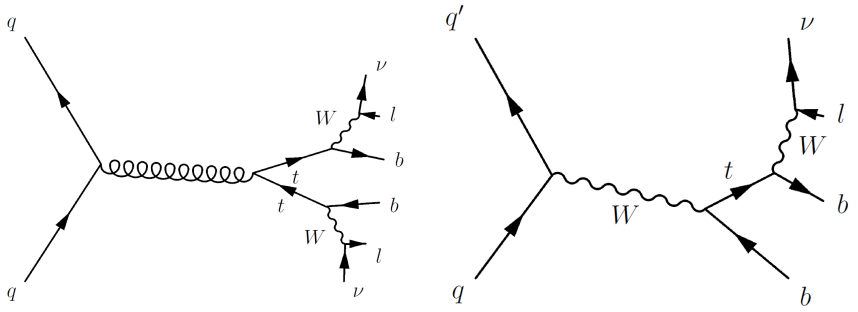

Figure 2.13: Background coming from $t\bar{t}$ (left) and single top (right) events.

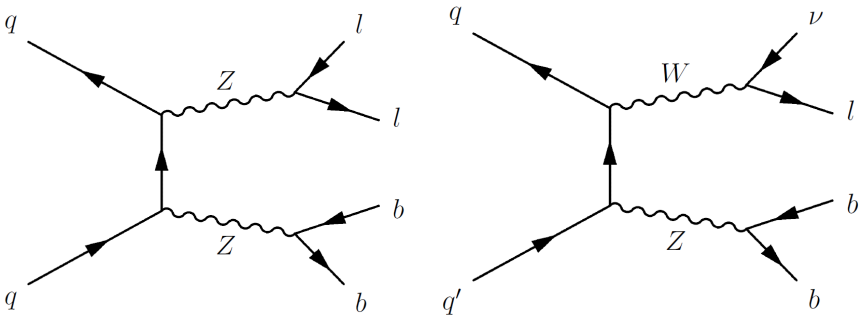

Figure 2.14: Background coming from ZZ (left) and WZ (right) events.

expected for $t\bar{t}$ decays. Another deviation from the signal signature is the lack of a Z-peak in the distribution of the invariant mass of the two leptons. Finally, the fact can be exploited, that most $t\bar{t}$ pairs are essentially produced at rest. Therefore the b-jets originating from the top quarks have a large angular separation, meaning the ΔR between the two jets tends to higher values. These three properties provide good cut parameters for the suppression of this background. Another contribution from top decays, although a very small one, comes from events with a single top decay. An example for such a decay is also given in Fig. 2.13. It also provides two b-quarks, but only one lepton and one neutrino. If there is one additional jet in the event, which is misidentified as an electron, or a muon coming from a jet decay, it can contribute a small amount to the background from top decays.

2.3.4 Diboson Background

The smallest background contribution comes from events with two vectorbosons. Two examples are the dominant background decay of two Z bosons and the decay of a W and Z boson (see Fig. 2.14). If one of the two Z bosons decays leptonically and the other one hadronically, the signal signature is reconstructed similar to the

Z+jets background in Section 2.3.2. The invariant mass of the two selected jets also gives a peak at the mass of the Z boson. An additional falsely reconstructed lepton (as mentioned in the previous section) in the WZ-decay can also lead to a small contribution for the diboson background.

Chapter 3

Experimental Setup

In this section the LHC (Section 3.1) and the ATLAS detector (Section 3.2) will be introduced with all its different detector parts and its trigger system. Then a brief outline of the reconstruction methods (Section 3.3) for different particles in the detector will be given.

3.1 The Large Hadron Collider

The Large Hadron Collider (LHC) [12, 13] is a 26.7 km long superconducting ring collider for proton-proton collisions and collisions of heavy ions (fully stripped lead ions). It is located at CERN, the European Laboratory for Particle Physics, in the tunnel which housed its predecessor LEP (Large Electron-Positron collider). The LHC itself is filled by particles coming from a complex of multiple accelerators, which accelerate the particles in a chain to an energy at which the LHC can start its operation. The first data was taken in 2008. The data used in Section 4 was taken in 2012 at a centre-of-mass energy $\sqrt{s} = 8\,\text{TeV}$. After a two year shutdown period, which started early 2013, the LHC is anticipated to run with its design energy of $\sqrt{s} = 14\,\text{TeV}$.

Four experiment sites are located at the LHC ring. The two main experiments, ATLAS and CMS, house general-purpose detectors which cover a wide range of physics, like search for the Higgs boson and particles beyond the Standard Model. The other two experiments are designed to study physics of strongly interacting matter at extreme energy densities with heavy-ion collisions (ALICE), and to investigate the slight discrepancies between matter and antimatter by studying decays of the B-hadrons (LHCb). An overview of the LHC with the accelerators and different detector sites can be seen in Fig. 3.1.

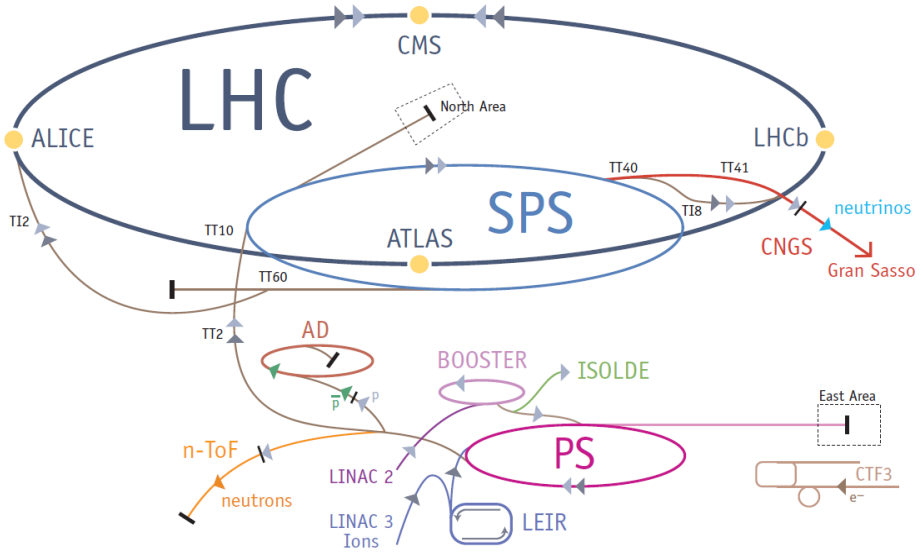

Figure 3.1: Overview of the LHC and the smaller accelerators at CERN [11].

3.2 The ATLAS Detector

The ATLAS detector [14] is a particle detector located at one of the four main sites at the LHC. Its design contains four separate detectors and two magnet systems, which are installed around the centre (where the collision point lies) in separate layers. The complete overview of the detector is given in Fig. 3.2.

Around the interaction point of the two proton beams the inner detector (ID) allows for measurement of the vertices created in the collision, measurement of momenta of charged particles, and identification of electrons. A solenoid magnet system surrounding the ID provides a 2 T magnetic field for deflexion of the charged particles.

An electromagnetic calorimeter, covering the pseudorapidity range $|\eta| < 3.2$, measures energy coming from electromagnetic showers and thus detects electrons and photons. A hadronic calorimeter, surrounding the electromagnetic one, provides measurement of energy coming from hadronic showers. Forward calorimeters allow for electromagnetic and hadronic energy measurements up to $|\eta| = 4.9$.

Around the calorimeter system the muon spectrometer provides precise measurement of the momentum of muons. A toroidal magnet system generates strong magnetic fields for the bending of the muon tracks.

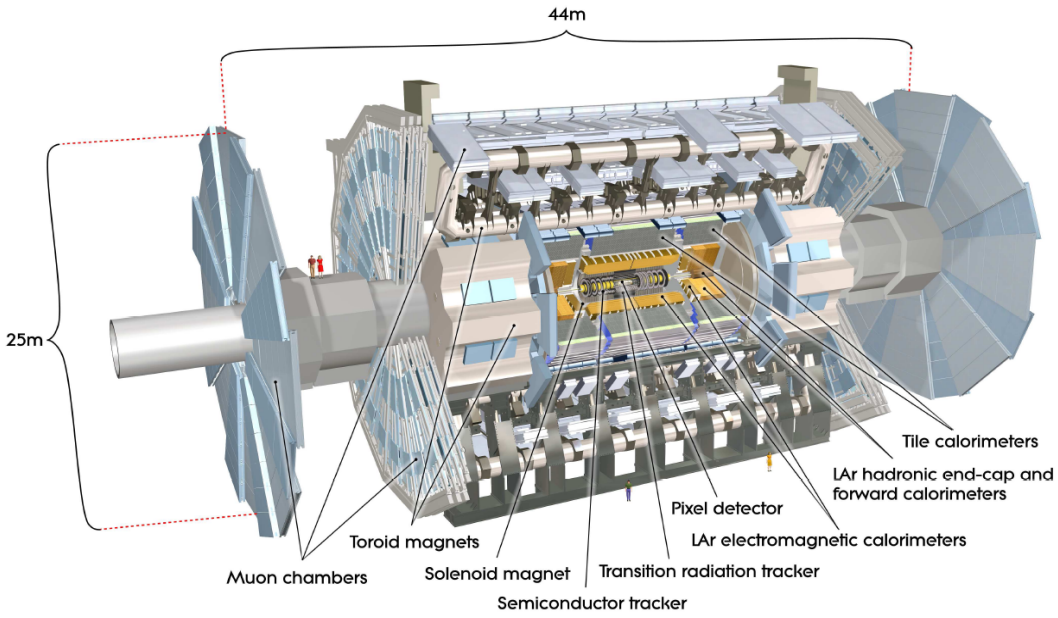

Figure 3.2: Overview of the ATLAS detector [14].

3.2.1 Coordinate System

Before discussing the design of the ATLAS detector in more detail, the coordinate system [14] and nomenclature used to describe it will be introduced, since they are not only used in this section about the ATLAS detector, but also later on in the analysis part of this thesis. The origin of the right-handed coordinate system is set in the centre of the detector, which is placed as close as possible to the nominal interaction point of the proton beam. The z-axis is defined to point in direction of the beam, while the x, y plane is transverse to it. The x-axis points to the centre of the LHC ring, whereas the y-axis points upwards. The rotational angle around the z-axis is ϕ and the polar angle θ is the angle from the beam axis. The pseudorapidity η is defined as

$$\eta = -\ln \tan\left(\frac{\theta}{2}\right) \tag{3.1}$$

and for massive objects the rapidity y is

$$y = \frac{1}{2} \ln \left[\frac{E + p_z}{E - p_z}\right]. \tag{3.2}$$

The transverse momentum p_T, transverse energy E_T, and the missing transverse energy E_T^{miss} are the projections of the respective particle properties on the x, y

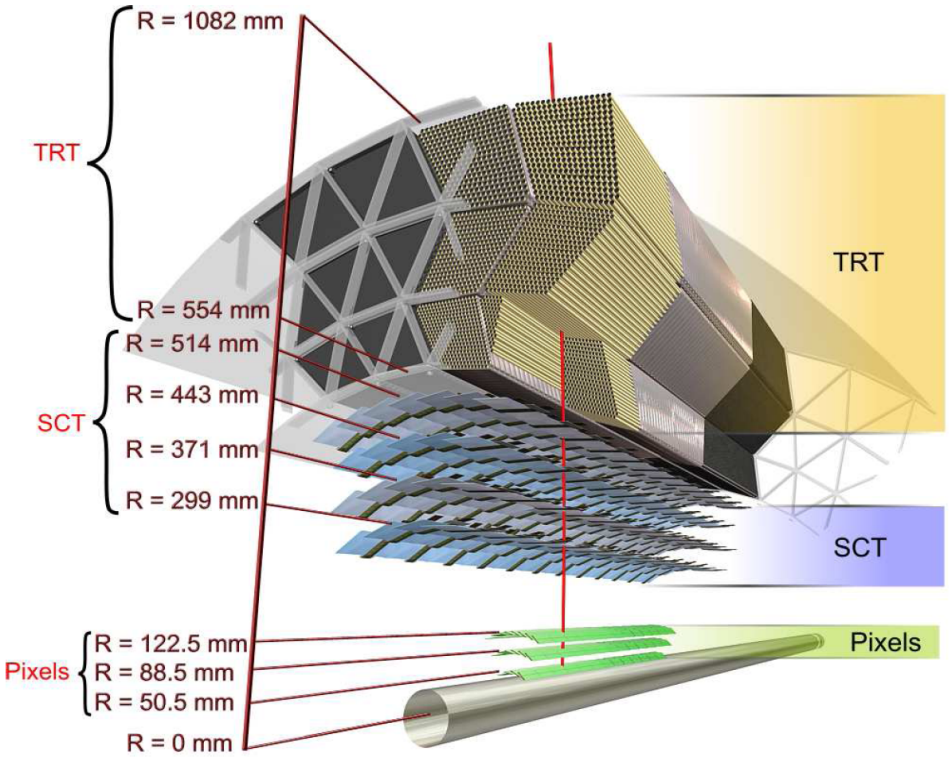

Figure 3.3: Overview of the inner detector [14].

plane. The distance ΔR in the pseudorapidity-azimuthal angle space is defined as

$$\Delta R = \sqrt{\Delta\eta^2 + \Delta\phi^2}. \tag{3.3}$$

3.2.2 Inner Detector

An overview of the ID [14] is shown in Fig. 3.3. It consists of a combination of three independent detectors. Silicon pixel and silicon microstrip (SCT) layers are installed at inner radii, while many layers of gaseous straw tubes of the transition radiation tracker (TRT), which are interleaved with transition radiation material, are located at larger radii. The two inner detectors provide high-resolution space point measurement over $|\eta| < 2.5$, while the high number of average hits (36) in the outer detector provide additional measurements to improve momentum resolution over a range $|\eta| < 2.0$ and electron identification to complement the measurement of the calorimeter. The TRT also enhances the pattern recognition of the pixel and SCT detectors.

The two inner detectors are cylindrically arranged in the barrel region around the beam axis. In the end-cap regions they are located on disks perpendicular to

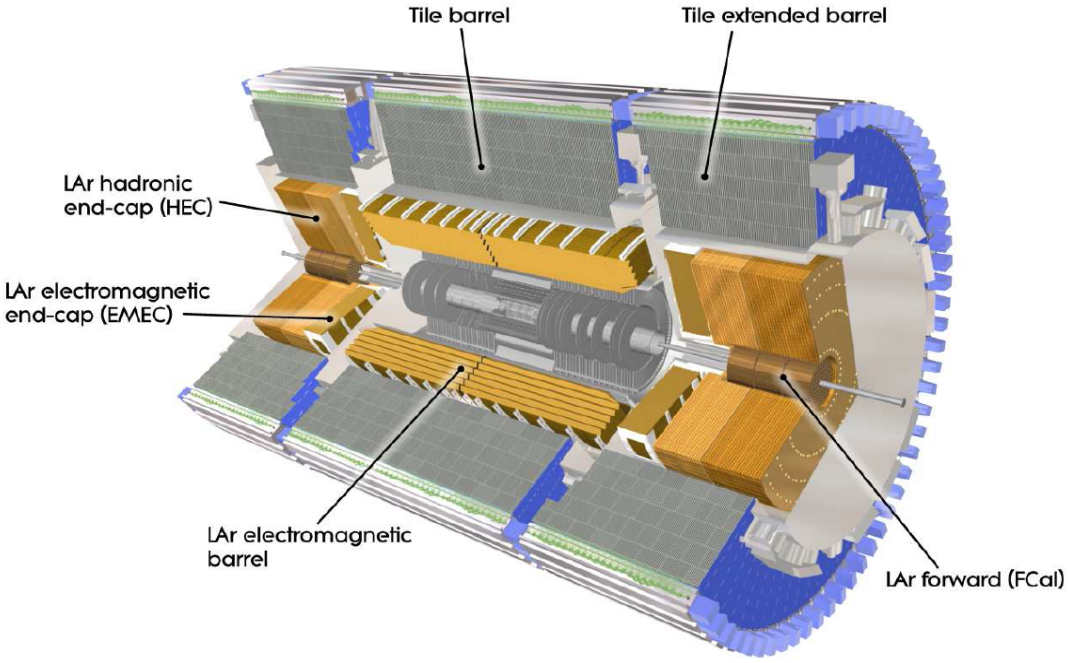

Figure 3.4: Overview of the calorimeter system [14].

the beam axis. The pixel sensors have an intrinsic accuracy in the barrel of 10 μm in the projection to the plane of the radius r and ϕ (r-ϕ-plane) and 115 μm in the z-direction. For the disks the accuracies are 10 μm (r-ϕ) and 115 μm in radial (r) direction.

Accuracies for each module of the SCT in the barrel are 17 μm (r-ϕ) and 580 μm (z), and 17 μm(r-ϕ) and 580 μm (r) in the disks. Around the pixel and SCT detectors, the TRT, arranged in 4mm diameter straw tubes, provides tracking information in r-ϕ only, with an intrinsic accuracy of 130 μm per straw.

3.2.3 Calorimeter System

The calorimeter system [14] is divided into two main layers of sampling calorimeters. The layer closest to the beamline consists of a barrel region and two end-cap regions. A cryostat in the barrel region, used for the cooling of the liquid argon in these calorimeters, houses the electromagnetic barrel calorimeter. Cryostats in the two end-cap regions each contain an electromagnetic end-cap calorimeter, a hadronic end-cap calorimeter (HEC), and a forward calorimeter, which measures electromagnetic as well as hadronic showers. In all these calorimeters liquid argon is used as the active detector medium. The electromagnetic calorimeters use lead as absorber material, whereas copper is used for the HEC and copper-tungsten for

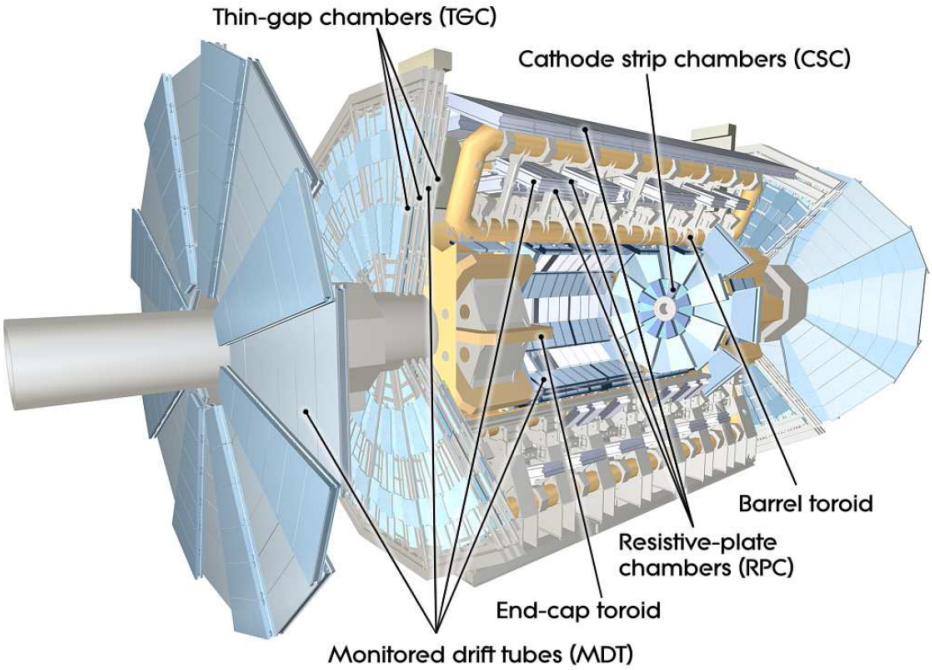

Figure 3.5: Overview of the muon spectrometer [14].

the forward calorimeter. In the range $|\eta| < 2.5$ (precision-measurement region) the electromagnetic calorimeter has three active layers in depth, while it has two layers over $2.5 < |\eta| < 3.2$. The forward calorimeter provides a full electromagnetic coverage up to $|\eta| < 4.9$.

The second layer consists of the hadronic calorimeter, which is divided into one central barrel and two extended barrels. For this detector the sampling medium consists of scintillator tiles and it has steel as absorber medium. This tile calorimeter covers a range of $|\eta| < 1.7$, which, with the addition of the end-cap calorimeters, gives a full hadronic coverage over $|\eta| < 4.9$.

3.2.4 Muon Detector

The outer part of the ATLAS detector is formed by the muon spectrometer [14], which is outlined in Fig. 3.5. It detects muons, which pass the calorimeter system of the detector with minimal absorption, and measures their momenta up to a range of $|\eta| < 2.7$. Muon momenta down to approximately 3 GeV can be measured by the spectrometer alone, while it was also designed to provide adequate momentum resolution in very high momenta regions (~ 3 TeV).

The precision-tracking chambers in the barrel region ($|\eta| < 1.05$) are embedded

into and onto the coils of the barrel toroid magnet system, whereas the end-cap chambers lie behind the end-cap toroid magnets. The muon chambers are ϕ-symmetrical arranged in eight sections, which themselves are subdivided into two slightly overlapping sectors of different size to reduce gaps in the coverage of the detector. In total, three layers of chambers in the barrel region are installed at different radii. In the end-cap regions large wheels, perpendicular to the beam axis, house the muon chambers at different distances from the interaction point. In the centre of the muon system a service shaft for the solenoid magnet, the calorimeters and the inner detector has been left free. Due to this gap in the muon detector, a high momentum track is not recorded in all three layers in ranges between $|\eta| < 0.04$ and $|\eta| < 0.08$.

In the range of $|\eta| < 2.7$ Monitored Drift Tube chambers (MDT's) provide the precision measurement of the muon momentum. Three to eight layers of drift tubes are installed in each chamber, which provide an average resolution of 80 μm per tube, and in total 35 μm per chamber.

Due to their higher rate capability and time resolution, Cathode-Strip Chambers (CSC) are installed in the range of $2 < |\eta| < 2.7$ in the tracking layer closest to the beam axis. They provide a resolution of 40 μm in the bending (η) plane and 5 mm in the transverse plane.

In addition to the MDT's and CSC, fast trigger chambers have been added to provide the capability to trigger on muon tracks in the detector. In the barrel region, Resistive Plate Chambers (RPC) were used, whereas Thin Gap Chambers (TGC) were chosen for the end-cap region ($1.05 < |\eta| < 2.4$).

3.2.5 Trigger

In physics, triggers are used to make a decision on the readout of measurements in an experiment, if a continuous data collection is not possible, due to technical limitations. This is vital for experiments, where an overwhelming number of events occur, which makes it impossible to store all information of every single event. This is the case for the experiment at the ATLAS detector, where high energy proton-proton collisions generate huge amounts of interactions per second, which results in very high event rates. The trigger system [14] of the ATLAS detector filters these events to identify those with interesting properties for the research at the LHC, which are then written to disk. For this purpose decision criteria of event selection for the readout system at different trigger stages are defined. The trigger system is split into three different trigger levels, being the L1 and L2 trigger on the level of detector processing, and the event filter, which selects on the basis of offline analysis procedures. Each stage refines the decisions of the previous one and applies additional criteria if necessary, gradually reducing the event rate. The L1 trigger responds to high transverse-momentum muons, electrons, photons,

jets, τ-leptons decaying into hadrons, and high missing or total transverse energy. It uses limited amounts of detector information to make decisions in a fraction of a second, reducing the event rate significantly. The L1 trigger also defines Regions-of-Interest (RoI's), meaning regions in η and ϕ, where the selection process identifies interesting properties. These RoI's are passed to the L2 trigger, which uses the full data information in them for additional selections, further reducing the event rate. The final stage applies offline analysis procedures on fully-built events to reduce the event rate to one which can be recorded for subsequent offline analysis.

3.3 Particle Reconstruction

This section will give a brief overview of techniques used for reconstruction of particles in the detector. The focus will be on particles relevant for the study described in Chapter 4, which are electrons, muons, jets, and neutrinos in form of E_T^{miss}. For the jets, the two algorithms used, the anti-k_T and the Cambridge-Aachen algorithm, and the important tool of b-tagging will be introduced.

3.3.1 Jets

The reconstruction of jets [15], which can be used for analysis, can be divided into multiple stages: clustering of cell signals in the calorimeter system, jet reconstruction by jet finder algorithms, and calibration to particle and interaction level.

There are two concepts for combining the signals coming from the cells of the hadronic calorimeter system into larger objects with physical four-momenta, being *signal towers* and *topological cell clusters*. For the signal towers the cells are projected on a grid in η and ϕ with tower size (bin size of the grid) $\Delta\eta \times \Delta\phi = 0.1 \times 0.1$. The signal of projected cells which completely fit into one tower is fully added to the tower. Signals from projective cells bigger than the towers or from non-projective cells are distributed to multiple towers according to the overlap fraction of their coverage. The cell signals are reconstructed on a basic electromagnetic energy scale. For the topological cell clusters one seed cell is picked that satisfies the condition for the signal-to-noise ratio $\Gamma = \frac{E_{cell}}{\sigma_{cell,noise}} > 4$. All neighbouring cells in every direction from this cell are added to the cluster. Neighbours of these added cells are also considered if the added cells have $\Gamma > 2$. Then a ring of guard cells, which fulfil $\Gamma > 0$, are added as a last step. These formed clusters are scanned for signal maxima and, if more than one are found, split according to these maxima. Additionally to the basic electromagnetic energy

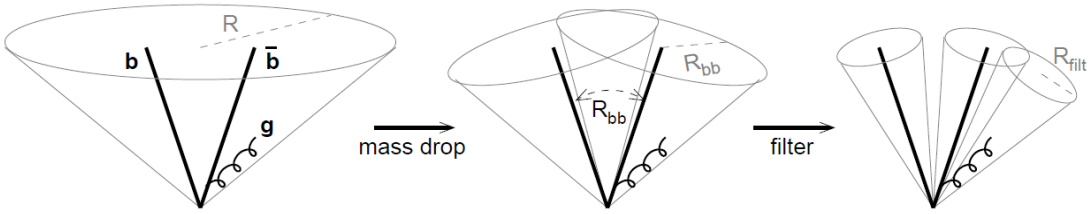

Figure 3.6: The different steps of subjet division with a jet reconstructed by the Cambridge-Aachen algorithm [16].

scale, the cluster can be calibrated to a local hadronic energy scale. In contrast to the signal towers not all calorimeter cells are used for the clustering.

The next step is to reconstruct jets with a jet finder algorithm. In general different algorithms satisfy different topologies of interest. Two algorithms, the anti-k_T and the Cambridge-Aachen (CA) algorithm, are used in Chapter 4 and will be briefly introduced in the following.

The **Cambridge-Aachen** algorithm [16] takes the angular distance

$$(\Delta R_{ij})^2 = (y_i - y_j)^2 + (\phi_i - \phi_j)^2 \tag{3.4}$$

between all pairs of entities (particles, pseudojets) i and j, recombines the closest pair, recalculates the ΔR_{ij} and repeats until all entities are separated by a $\Delta R_{ij} > R$, with R being the cone in which the objects are clustered.

In an additional treatment, the resulting CA jet j with radius R is then subdivided in two subjets by introducing two dimensionless parameters μ and y_{cut} by the following steps. First the jet is divided into two subjets j_1 and j_2, with $m_{j_1} > m_{j_2}$, by undoing the last step of the clustering done by the CA algorithm. If the conditions

$$m_{j_1} < \mu m_j \tag{3.5}$$

$$y_{cut} < \frac{\min\left(p_{T,j_1}^2, p_{T,j_2}^2\right)}{m_j^2} \left(\Delta R_{j_1,j_2}\right)^2 \tag{3.6}$$

are fulfilled the procedure stops. If they are not fulfilled, j is set to be j_1 and the procedure is repeated. In a last step the neighbourhood of j_1 and j_2 is further filtered (see Fig. 3.6) by reducing their radii R_{bb} to $R_{filt} < R_{bb}$ and taking the three hardest subjets which appear by this procedure. This allows to take radiation from the two subjets into account at high p_T of the jet j, while reducing contributions from underlying events. This approach of using the subjets of a CA jet is stated to be very promising for the search of a Higgs boson in the ZH and WH channels in the boosted regime [16].

For the **anti-k_T** algorithm [15, 17] first two distances d_{ij} between entities i and j and d_{iB} between entity i and the beam B are defined:

$$d_{ij} = \min\left(p_{T,i}^{2p}, p_{T,j}^{2p}\right) \frac{\left(\Delta R_{ij}\right)^2}{R^2} \tag{3.7}$$

$$d_{iB} = p_{T,i}^{2p} \tag{3.8}$$

The clustering is performed by finding $\min\left(d_{ij}, d_{iB}\right)$ and, if this is d_{ij}, combining the entities i and j. If the smallest distance is d_{iB}, i is defined as a jet and removed from the list of entities. The radius R is defined like for the CA algorithm, while the parameter p is to control the relative power of the energy against the angular (ΔR_{ij}) scale. The choice of p defines the different clustering approaches. In fact, choosing $p = 0$ is equivalent to the CA algorithm described before, while $p = 1$ corresponds to the inclusive k_T-algorithm, which will not be further investigated. For the anti-k_T algorithm p is set to -1.

After applying the jet finder algorithm, the jets are further calibrated by weighting to a hadronic energy scale (if not done before in case of the topological cell clusters). Finally, calibrations to particle and interaction level are applied to account for different factors like noise, pile-up from multiple vertices in the event, algorithm effects, underlying events or physics environment.

3.3.2 B-Tagging

A tool, which is very important for the analysis presented in Chapter 4, is b-tagging [15]. It exploits certain properties of B-hadron decays to distinguish them from decays originating from lighter quarks. The B-hadron retains a large proportion of the b-quark momentum of about 70%. The mass of B-hadron is also relatively high (> 5 GeV), so that the decay products have a large p_T with respect to the jet axis. The most important property of B-hadrons is their long lifetime, which results in a flight path length of several millimetres for high p_T b-jets. This results into secondary vertices in the detector, which can be identified by spatial b-tagging, either explicitly reconstructing the displaced secondary vertex, or measuring the impact parameters d_0 and z_0 of the B-hadron decay products. Another approach is to tag the lepton in the b-jet coming from semi-leptonic decays of the B-hadrons. Due to high momenta and high mass of the B-hadrons, the lepton will have relatively high p_T as well as a high p_T relative to the jet axis. This is called soft lepton tagging, due to the significantly lower p_T of these leptons compared to the ones coming from decays of vectorbosons.

3.3.3 Electrons

Electrons [15] can be reconstructed using information from the electromagnetic calorimeter and the ID combined ($|\eta| < 2.5$) and from the electromagnetic calorimeter only for forward electrons ($|\eta| > 2.5$). There are two methods to reconstruct electrons for the combined approach. The standard one is to start from clusters reconstructed in the calorimeter and then construct the identification variables from information coming from the ID and the EM calorimeter. The second one starts from tracks in the ID, but the variables are built in the same way as the first one. This second method is optimised for electrons with low energies by selecting good quality tracks and matching them with energy deposits, which are relatively isolated. The standard method will be described in more detail in the following.

The standard algorithm takes a seed electromagnetic tower with E_T above approximately 3 GeV and searches for a matching track which does not originate from a photon-conversion pair in the ID. The extrapolated track then must match the energy cluster within a $\Delta\eta \times \Delta\phi$ window of 0.05×0.10, while the ratio of the energy from the calorimeter and the momentum of the ID has to be smaller than 10. These electron candidates can be discriminated from jets and background electrons by applying different identification methods combining information from the calorimeter and track properties.

Electrons which are outside the coverage of the ID can still be reconstructed, by using only the inner wheel of the end-cap from the EM calorimeter and the forward calorimeter. But since these electrons cannot be distinguished from photons, due to the missing track measurements from the ID, they can only be identified cleanly for certain topologies like $Z \to ee$ or $H \to eeee$.

3.3.4 Muons

Since muons only lose a small fraction of their energy in the calorimeter system, they pass on through to the muon spectrometer, which is the main detector system for their reconstruction. Multiple methods can be applied to reconstruct muons [15], using different parts of the detector. *Standalone* muons are only reconstructed by track hits in the muon spectrometer and extrapolation to the beam line. Standalone muons which are matched to a track in the ID are called *combined* muons, which use information from both detector systems. By extrapolating tracks from the ID to the muon system and matching them to nearby hits, *tagged* muons are obtained. Finally, muons can also be reconstructed by using the energy deposits left by the muons in the calorimeter system, which complements reconstruction of muons with low p_T and in regions of the muon system with low acceptance (mostly $\eta \sim 0$).

The different algorithms are categorised in two different families, so that each

family has an algorithm for most of the methods mentioned above. The two families are called Staco and Muid. The common family for physics analysis is the former one, but for the analysis in Chapter 4 the latter is used.

3.3.5 Missing Transverse Energy

In general E_T^{miss} [15] is the energy which remains after summing up the energy vectors of all detectable particles produced in the event. Since the energy in the transverse plane of the detector has to be conserved, this remaining energy component can be identified as particles which cannot be seen in the detector, like neutrinos or particles beyond the Standard Model. This approach of reconstructing E_T^{miss} requires to minimise impacts from the limited detector coverage, the finite detector resolution, the presence of dead regions in the detector and sources of noise which leads to false E_T^{miss}. Thus the measurement of E_T^{miss} is directly dependent on the quality of particle reconstruction in all parts of the ATLAS detector.

Two different algorithms for the reconstruction of E_T^{miss} are used at ATLAS, a cell-based and an object-based one. The cell-based algorithm starts with the energy deposits in cells of the calorimeter system. The cells are first calibrated by global weights depending on the energy density, and then according to the reconstructed objects to which they are assigned to. Corrections also have to be applied for muons, since they pass through the calorimeter, and the energy lost in the cryostats. The object-based algorithm takes the calibrated, reconstructed objects in the event and applies further corrections for the energies outside of these objects, which are classified and calibrated as low p_T deposits from pions.

Chapter 4

Search for Higgs Production in the ZH $\rightarrow l\bar{l}b\bar{b}$ channel

In this chapter a search for a Higgs boson in the ZH $\rightarrow l\bar{l}b\bar{b}$ channel (see Section 2.3.1) will be presented. For the analysis, the full dataset, corresponding to an integrated luminosity of approximately $20.3\,\text{fb}^{-1}$, collected by ATLAS (see Section 3.2) in 2012 at a centre-of-mass energy of $\sqrt{s} = 8\text{TeV}$ was used. First the simulated data samples, which were used to estimate the signal and background contributions to the measurement, are introduced. Then the criteria for the selection of the different objects used in the analysis (electrons, muons, and jets) and the selection of events are outlined. This is followed by an overview of the estimation and modelling of the background contributions mentioned in Section 2.3.2, 2.3.3 and 2.3.4, which introduces the control regions used in the analysis and the corrections applied to account for mismodellings in the data samples. Then the sources of systematic uncertainties considered, which are used in the exclusion limit fit in the last section of this chapter, are described. The last section presents the results of the analysis. A binned profile likelihood fit is performed to set an upper exclusion limit on the production cross-section of a Higgs boson in the ZH $\rightarrow l\bar{l}b\bar{b}$ channel. In addition, the results of two studies regarding the selection of the jets used for the reconstruction of the Higgs boson are presented.

4.1 Data and Monte Carlo Simulation Samples

This section will outline the different data samples used for the studies presented in this thesis. Data taken in 2012 is considered for the analysis, thus events produced by proton-proton collisions at $\sqrt{s} = 8$ TeV are taken into account and are simulated in Monte Carlo (MC) samples, which are used to estimate signal and background contributions to the measurements. For all samples local copies

of reduced size have been produced to reduce processing time of the analysis. Unused variables have been excluded and single- and dilepton cuts have been applied. Events must have at least two leptons with $p_T > 7$ GeV and at least one lepton with $p_T > 20$ GeV. These leptons also have to pass basic quality requirements (see Section 4.2.1). The cuts were chosen to not interfere with the final selection cuts applied in Section 4.2.1.

For the signal and the backgrounds (see Section 2.3) different MC samples are used. In total nine samples, which are produced by the MC generator Pythia8 [18], are used for the $ZH \to l\bar{l}b\bar{b}$ signal (see Section 2.3.1) for a Higgs boson with mass between 110 and 150 GeV to provide an analysis over this mass range around 125 GeV. MC samples for the top background (see Section 2.3.3) are divided in one $t\bar{t}$ and three single top samples to account for the different channels. The samples for $t\bar{t}$ and the single top Wt- and s-channel use the Powheg generator [19], while the AcerMC generator [20] was chosen for the single top t-channel. Backgrounds coming from diboson decays (see Section 2.3.4) are taken into account by two samples for WZ and ZZ decays. For these samples the Herwig generator [21] was used. Finally, the dominant Z+jets background is simulated using the Sherpa generator [22]. Samples for this background are divided into regions of the p_T of the Z boson and also in different regions selected by applying a selection on B- and C-hadrons. To account for mismodelling of the Z+jets decays in the MC Sherpa samples, which will be further discussed in Section 4.3.2, this background is divided into the different flavours of hadrons with $p_T > 5$ GeV within the jets selected for the Higgs boson reconstruction. The analysis distinguishes between decays with at least one of the two jets containing a B-hadron (Zb), at least one jet containing a C-hadron if there is none with a B-hadron (Zc), and with no jet containing a B- or C-hadron (Zl). To gain more statistics for the crucial higher p_T^Z regions (see Section 4.2.2) the samples are also divided into different regions of the p_T of the Z boson. Finally the samples are also split into the lepton flavour of the decay products of the Z boson (electrons, muons, taus). This leads to a total of 54 samples for the Z+jets background. Background contributions coming from multijet events are shown to be negligible for the analysis in the $ZH \to l\bar{l}b\bar{b}$ channel [10].

To assure the correct normalisation for the different signal and background contributions, the events extracted from the MC samples have to be scaled to the integrated luminosity $\left(\int Ldt\right)_{data}$ of the recorded data used. The respective scale factors can be calculated by

$$f_{MC} = k \cdot \epsilon_{filter} \cdot \epsilon_{skim} \cdot \frac{\left(\int Ldt\right)_{data} \sigma_{MC}}{N_{MC}}, \tag{4.1}$$

with the k-factor k, the filter efficiency ϵ_{filter}, the skim efficiency ϵ_{skim} (coming from the cuts applied to the local versions of the MC samples described in this section),

the cross-section σ_{MC} of the process, and the number of events N_{MC} in the MC sample. The k-factor accounts for corrections to the cross-section coming from next-to-leading order (NLO) calculations. The cross-sections, k-factors and filter efficiencies for all MC samples used are listed in Tab. A.1, A.2 and A.3. The skim efficiencies are taken from information of read and written events gathered from the processing jobs of the samples. Finally, N_{MC} is determined by the analysis itself.

4.2 Selection

This section introduces the selection criteria for the different objects and the event topology in the analysis. All cuts applied are optimised for the search for a Higgs boson at mass $m_H = 125\,\text{GeV}$.

4.2.1 Object Selection

The selection for the objects [10] in the analysis contains different criteria for jets, electrons and muons. The objects are divided in two categories, *loose* and *signal*, passing different levels of cuts.

Muons are reconstructed using the Muid algorithms (see Section 3.3.4). They must pass basic quality requirements and cuts on the impact parameters (see Section 3.3.2). Three different types of muons are chosen to select loose muons, to cover different acceptances of the detector. In the forward region ($|\eta| > 2.5$) no information from the ID can be used (see Section 3.2.2), and at $|\eta| < 0.1$ there is a gap in the muon spectrometer (see Section 3.3.4). For $|\eta| < 2.7$ combined muons are used, the range $2.5 < |\eta| < 2.7$ is also covered by standalone muons, and calorimeter muons are selected for $|\eta| < 0.1$. Lower p_T cuts of 10GeV, for combined and standalone muons, and 20 GeV, for calorimeter muons, are applied. Finally, the scalar sum of all track p_T within a cone of $\Delta R = 0.2$ around a selected loose muon has to be smaller than 10% of the muon p_T. This variable will be denoted as *ptcone*20 in the following. In addition to these loose muon requirements, signal muons must also fulfil $|\eta| < 2.5$ and $p_T > 25\,\text{GeV}$.

Electrons also must pass basic quality requirements and impact parameter cuts. A lower E_T cut of 10 GeV and an upper $|\eta|$ cut of 2.47 has to be passed by loose electrons. Equal to muons, *ptcone*20 has to be smaller than 10% of the loose electron p_T. Signal electrons have to pass additional requirements on track quality and shower shape in the calorimeter and must have a E_T value higher than 25 GeV.

For **jet** reconstruction, topological cell clusters and two different jet finder algorithms, anti-k_T and Cambridge-Aachen, are used (see Section 3.3.1). For

the nominal analysis anti-k_T jets with $R = 0.4$ are selected, whereas the study in Section 4.5.3 uses Cambridge-Aachen jets with $R = 1.2$. The selection of the latter will be described in the respective section (4.5.3). The anti-k_T jets are corrected for pile-up interactions and calibrated with p_T- and η-dependent correction factors. To reduce contributions from pile-up, at least 50% of the scalar sum of track p_T matched to a selected jet has to come from tracks originating from the primary vertex of the event. This cut is only applied if the jet has a $p_T < 50$ GeV and $|\eta| < 2.4$. Loose jets have to fulfil $p_T > 20$ GeV for $|\eta| < 2.5$ and $p_T > 30$ GeV for $2.5 < |\eta| < 4.5$. Signal jets, which are used for the reconstruction of the Higgs candidate, are selected for $|\eta| < 2.5$.

For all objects in the analysis (electrons, muons and jets) overlap removals are applied, to ensure that leptons coming from decays within a jet are not chosen for the reconstruction of the Z boson. In addition electrons which are in the vicinity of a reconstructed muon are removed, since muons occasionally radiate a photon, which in combination with the muon track is identified as an electron.

Jets, which originate from b-quarks, are selected by b-tagging using the MV1 algorithm, which combines information of different algorithms based on spatial b-tagging (see Section 3.3.2). A lower cut on the MV1 tagging weight, which is the output variable of the algorithm, of 0.8119 is applied. This is equivalent to a tagging efficiency of 70% for b-jets, determined in simulated $t\bar{t}$ events, and rejection factors of 5 for c-jets and 150 for jets originating from lighter quarks.

For the background contributions Zc and Zl (see Section 4.1) very few simulated events pass the cut on the tagging weight, due to the high suppression of the MV1 algorithm. Thus these backgrounds cannot be described correctly by cutting on the tagging weight. In these cases a different approach is chosen to get the correct description. Probabilities for jets to be b-tagged, parametrised by functions of p_T and η, are used to weight the event [10]. In the following this method is called truth-tagging.

For the reconstruction of the E_T^{miss} the cell-based approach is used (see Section 3.3.5). The E_T^{miss} is further corrected according to energies of clusters associated with objects in the event by using their calibrations.

For the simulation samples corrections are applied to account for discrepancies to data for object identification and reconstruction efficiency and for object energy and momentum calibrations and resolutions. These corrections are provided by ATLAS performance groups.

4.2.2 Event Selection

Events are selected by single- or di-lepton (electron or muon) triggers. For the reconstruction of the Z boson exactly two loose leptons with same flavour and opposite charge are selected, with at least one also passing the signal lepton re-

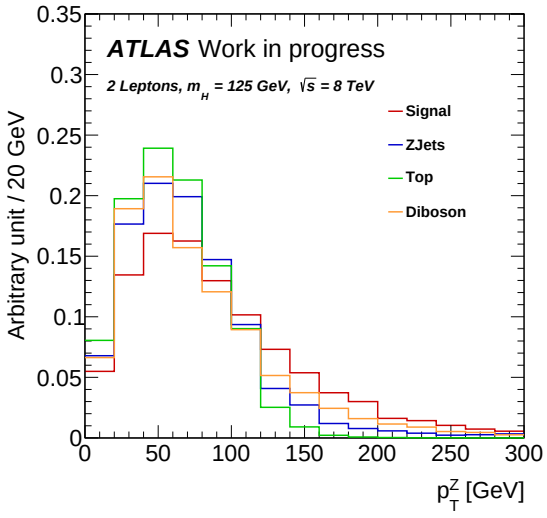

Figure 4.1: Distribution of p_T^Z for the signal and the different backgrounds. Normalisations have been scaled to one.

quirements. The invariant mass reconstructed from the two selected leptons must be in a window around the Z mass between 83 and 99 GeV. The E_T^{miss} in the event must be lower than 60 GeV. At least two signal jets have to be selected, with exactly two of them being b-tagged, which are used for the reconstruction of the Higgs boson. As already mentioned in Section 4.2.1, instead of directly b-tagging with the MV1 algorithm, truth-tagging is applied for the Zc and Zl background. For these backgrounds all signal jets in the event are considered to determine a probability of the event containing two b-tagged jets, which is used to weight the event. Since every event is considered by this treatment it assures high statistics for these backgrounds. The leading b-tagged jet is required to have a p_T of at least 45 GeV.

As mentioned in Section 4.1, the analysis is split into five regions of the p_T^Z to account for the higher sensitivity for the signal in the regions of high p_T^Z. This difference in sensitivity becomes apparent in Fig. 4.1, where the p_T^Z for the signal and the different backgrounds is shown. Additional cuts on the angular distance ΔR_{bb} between the two selected b-jets are applied, dependent on the p_T of the reconstructed Z boson. An overview of these cut values can be seen in Tab. 4.1. The lower and upper cut reduce background contributions coming from Z+jets (see Section 2.3.2) and $t\bar{t}$ (see Section 2.3.3) events. The upper cut is reduced with higher values of p_T^Z to exploit the increasing collimation of the two selected jets in signal events. This increasing collimation is also the reason for the removal of the lower cut for the highest p_T^Z bin. The distributions of m_{ll} and E_T^{miss} before the

p_T^Z [GeV]	0-90	90-120	120-160	160-200	> 200
ΔR_{bb}	> 0.7	> 0.7	> 0.7	> 0.7	
	< 3.4	< 3.0	< 2.3	< 1.8	< 1.4

Table 4.1: ΔR_{bb} cuts for different p_T^Z ranges.

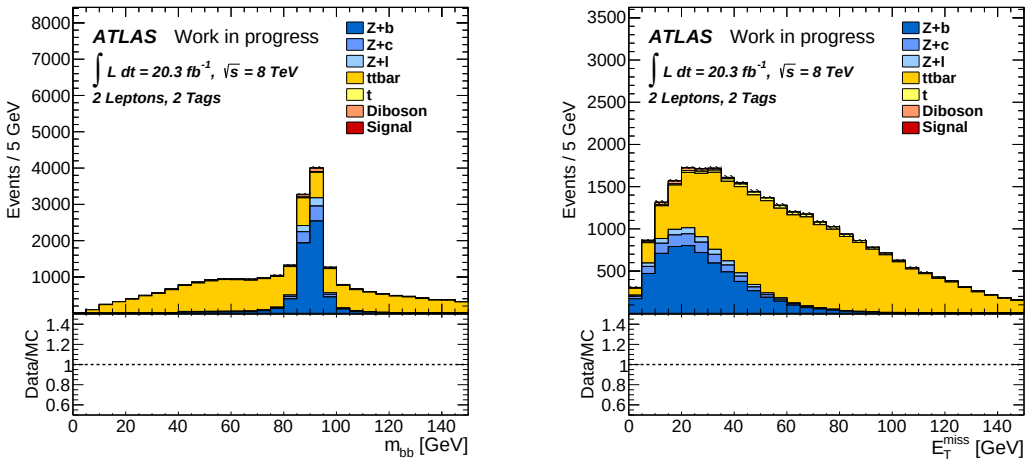

Figure 4.2: Distributions of m_{ll} (left) and E_T^{miss} (right) before the ΔR_{bb}, m_{ll}, and E_T^{miss} cuts.

ΔR_{bb}, m_{ll}, and E_T^{miss} cuts are shown in Fig. 4.2. Fig. 4.3 shows the distributions of ΔR_{bb} for the different p_T^Z regions before the cuts in Tab. 4.1 are applied.

After all selection cuts are applied the p_T of the two selected b-jets is corrected for reconstructed muons within the jet and discrepancies of the reconstructed jet p_T to the true jet p_T at low values, as described in [10]. The first correction takes muons which are dropped by the overlap removal (see Section 4.2.1) and takes their energy into account for the jet. For the correction to the truth jet p_T, scale factors are applied to compensate these discrepancies. These scale factors were developed from the discrepancy between the truth and reconstructed p_T of selected b-jets [10]. The truth p_T and muon in jet correction is only applied in the regions with two b-tagged jets selected (see Section 4.3.1).

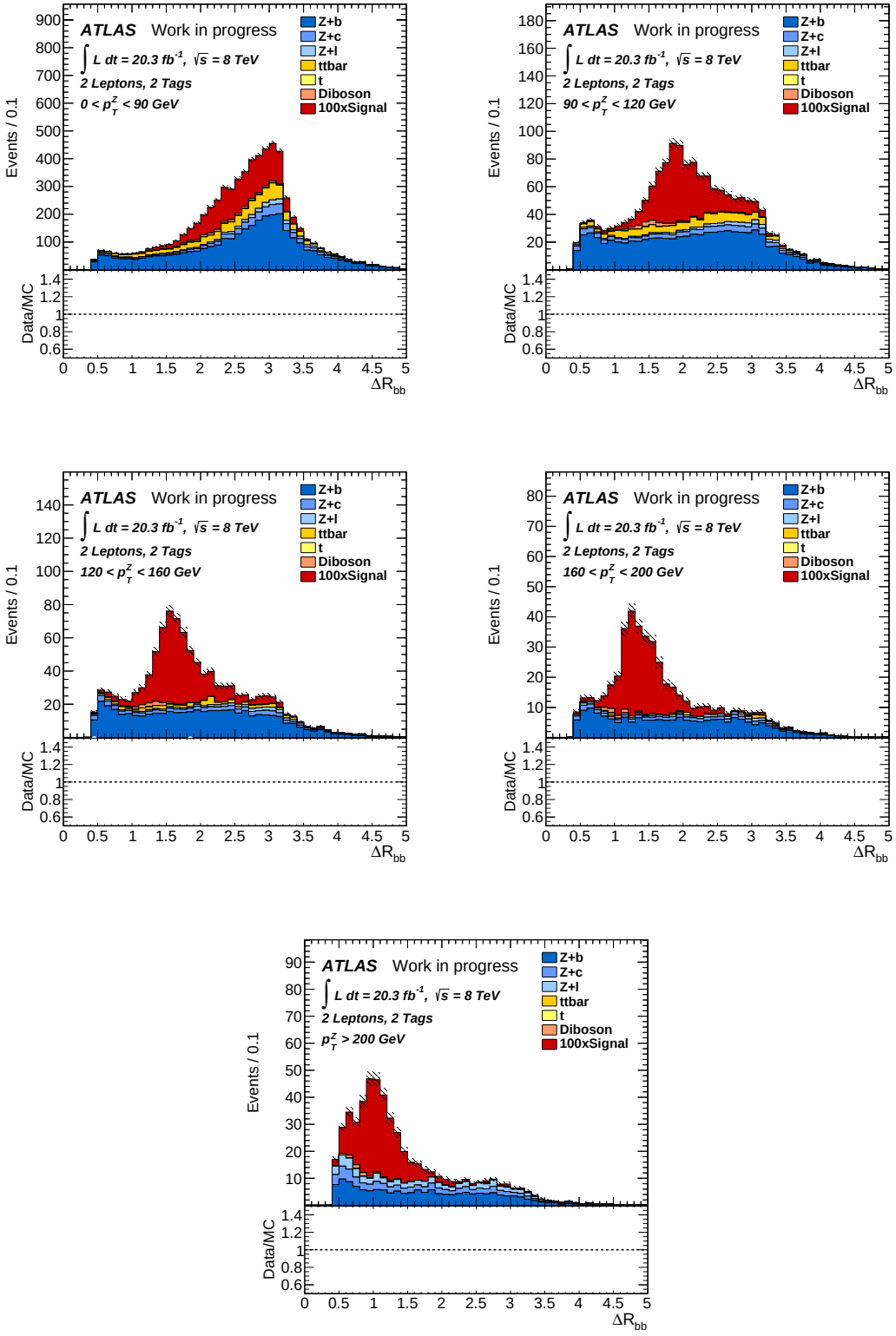

Figure 4.3: Distribution of ΔR_{bb} for each p_T^Z region before the cuts in Tab. 4.1. The signal distributions have been scaled by 100.

4.3 Signal and Background Estimation and Modelling

In this section the estimation and modelling of the signal and the different backgrounds is described. The estimation of signal and all background processes for the $ZH \to l\bar{l}b\bar{b}$ channel are taken from Monte Carlo simulation samples and normalised as described in Section 4.1. The definition of different signal and control regions will be given, which are used to produce the results presented in Section 4.5. Some backgrounds, coming from the different flavour contributions of Z+jets and the $t\bar{t}$ contribution, have to be normalised by fitting them to data, since these backgrounds are not expected to be perfectly described by MC. Finally, a kinematic correction to the contribution coming from the Z+jets Sherpa samples has to be applied, to account for a mismodelling of p_T^Z for this background in the MC samples.

4.3.1 Signal- and Controlregions

For this analysis multiple regions are defined according to jet and b-jet multiplicity and in regions of p_T^Z. The signal region is defined by the criteria described in Section 4.2.2 and is split into a 2-jet and a 3-jet region, with two and three signal jets respectively in the selection. The dominant background in this region is Zb with small contributions of Zc, Zl, $t\bar{t}$ and diboson decays, while single top events are near to negligible. The distributions of the main discriminant of the analysis, the invariant mass m_{bb} of the two selected b-jets, for the two signal regions is shown in Fig. 4.4.

Additionally to the signal regions, multiple control regions are defined, to be able to put constraints on the main backgrounds. Two regions are used to get varied contributions of jet flavours in the Z+jets background, by reducing the b-tagged jet multiplicity to one (1-tag) and zero (0-tag). For the 1-tag region, the second jet for the Higgs boson reconstruction is the non b-tagged jet with the highest p_T. The two jets with the highest p_T are used to reconstruct the Higgs boson in the 0-tag region. Apart from the difference in b-tagged jet multiplicity the selection is the same as for the signal regions. For both, the 0-tag and the 1-tag region, only events with two signal jets are considered. In both regions the background consists almost exclusively of Z+jets events, with mostly Zb and Zc in the 1-tag and Zl in the 0-tag region. The respective distributions of m_{jj} can be seen in Fig. 4.5.

Two additional regions provide a very high contribution of top backgrounds, mostly coming from $t\bar{t}$ decays. For one of these two top regions the flavour of the two selected leptons is required to be different, thus selecting one muon and one

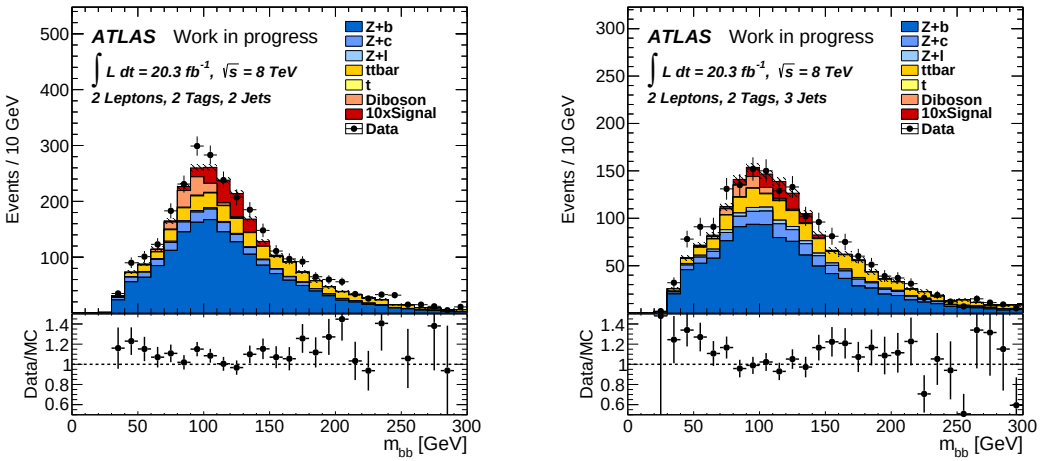

Figure 4.4: Distribution of m_{bb} for the signal regions with two (left) and three (right) jets in the selection. The signal distribution has been scaled by 10.

electron ($e+\mu$ top region). For the other region the selection is altered by removing the cut on E_T^{miss} and selecting the sidebands of the Z-peak, $40 < m_{ll} < 83$ GeV and $m_{ll} > 99$ GeV (sidebands top region). The $e + \mu$ top region is used as a control region, while the sidebands top region is a validation region, which is used to confirm the correct modelling of the background. The m_{bb} distributions of both top regions is also shown in Fig. 4.5.

4.3.2 Flavour Fit

The distributions of m_{jj} for the different signal and control regions, which can be seen in Fig 4.4 and 4.5, show a mismodelling of the backgrounds in MC. This leads to a significant discrepancy between data and MC. This mismodelling is assumed to originate from incorrect fractions of Zb and Zc in the Z+jets MC samples, and an incorrect normalisation of $t\bar{t}$. To account for these wrong modellings, the normalisations of the Zb, Zc, and $t\bar{t}$ background are kept floating in a likelihood fit, which is described in Section 4.5.1. The control regions (see Section 4.3.1) provide the necessary data to correctly describe these backgrounds within the fit. The shapes of the respective background m_{jj} distributions are assumed to be correctly described by MC.

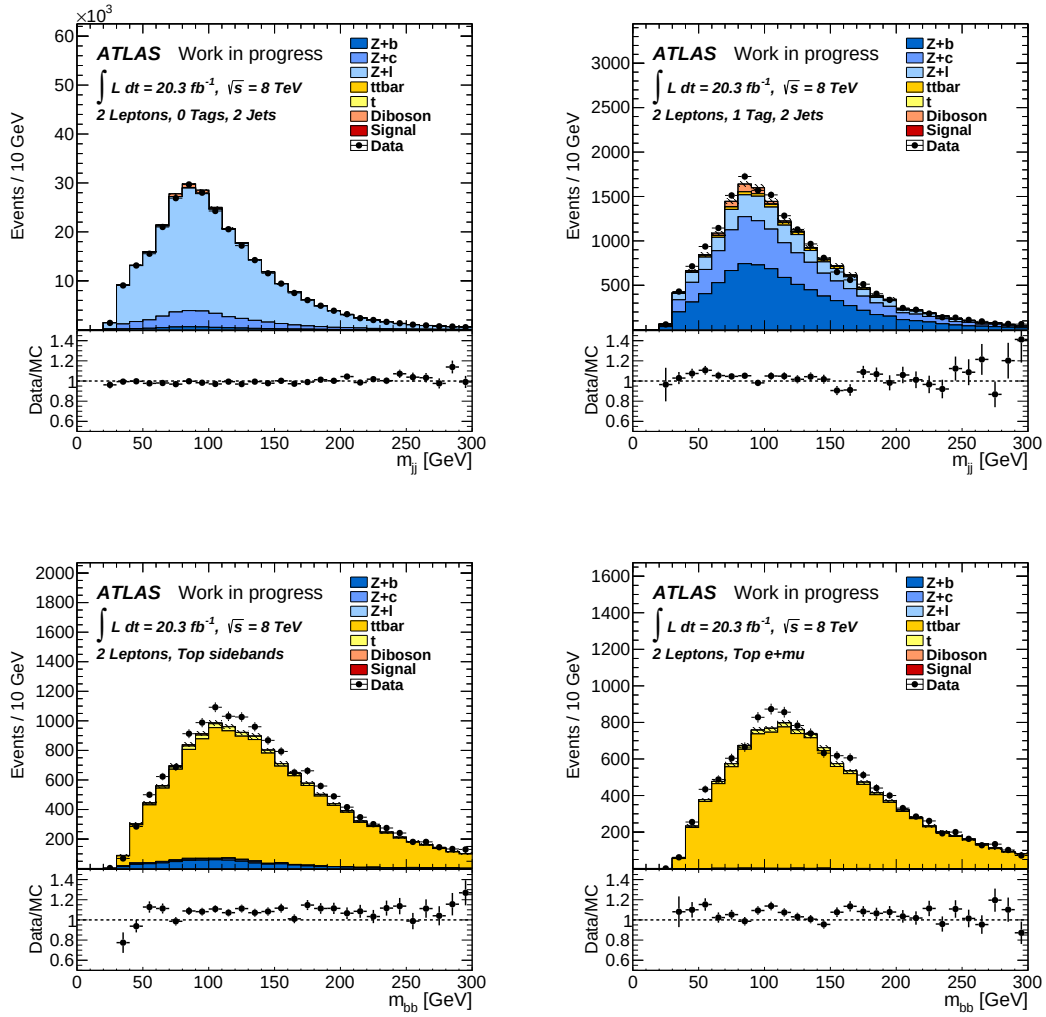

Figure 4.5: Distribution of m_{jj} for the 0-tag (top left) and 1-tag (top right) region and m_{bb} for the sidebands (bottom left) and $e + \mu$ (bottom right) top region.

4.3.3 Z+Jets Corrections

For the Z+jets Sherpa samples a mismodelling of the $\Delta\phi$ between the two selected jets for the Higgs boson reconstruction, and the p_T^Z can be observed. This is mostly present in the 0-tag and 1-tag region. The respective distributions for the 2-jet region can be seen in Fig. 4.6, where the discrepancies between data and MC is clearly visible with the slope in the data/MC ratio. The effect on the distributions of m_{jj} for the 0-tag and 1-tag 2-jet regions can also be seen in Fig. 4.6. To correct the mismodelling in $\Delta\phi$, reweighting factors are applied in the analysis, which are obtained by comparing data and MC $\Delta\phi_{jj}$ distributions of the Z+jets background in the 0-tag region [10]. This correction on $\Delta\phi$ also corrects the mismodelling of the p_T^Z since these two variables are highly correlated. Upon applying the correction factors, the data/MC agreement improves significantly for the $\Delta\phi$ and p_T^Z (see Fig. 4.7) as well as for the m_{jj} distributions (see Fig. 4.5).

4.4 Systematic Uncertainties

The fit described in Section 4.5.1 is performed considering statistical uncertainties only and also after taking dominant sources of systematic uncertainties into account. As systematic uncertainty sources, uncertainties coming from the modelling of the background processes and the most important experimental uncertainties are considered, which affect the normalisation and/or shape of the m_{jj} distributions. For modelling, uncertainties for the normalisations and flavour contributions of the different backgrounds in addition to the floating normalisations for Zb, Zc and $t\bar{t}$ (see Section 4.3.2) are added, as well as an uncertainty on the integrated luminosity of the recorded 2012 data. For experimental uncertainties the ones coming from the calibration of the jet energy scale (JES) and the b-tagging efficiencies are taken into account, since they are found to have the largest contribution to the total systematic uncertainty [10].

These uncertainties are provided to the fit as additional input distributions, which are produced by applying the one σ variations of the respective corrections instead of the nominal values. The one σ variations, like the nominal corrections, are provided by ATLAS performance groups. The m_{jj} distributions in the fit are allowed to float within the range given by the $\pm$ one σ distributions and the nominal one. In the fit described in Section 4.5.1 the uncertainties are included into the likelihood functions as additional free nuisance parameter θ, which represent the variation of their respective systematic uncertainty within the function. In total 14 systematic variations are considered for the b-tagging efficiency, split into the flavour of the tagged jet. For the JES 24 systematic variations are given, address-

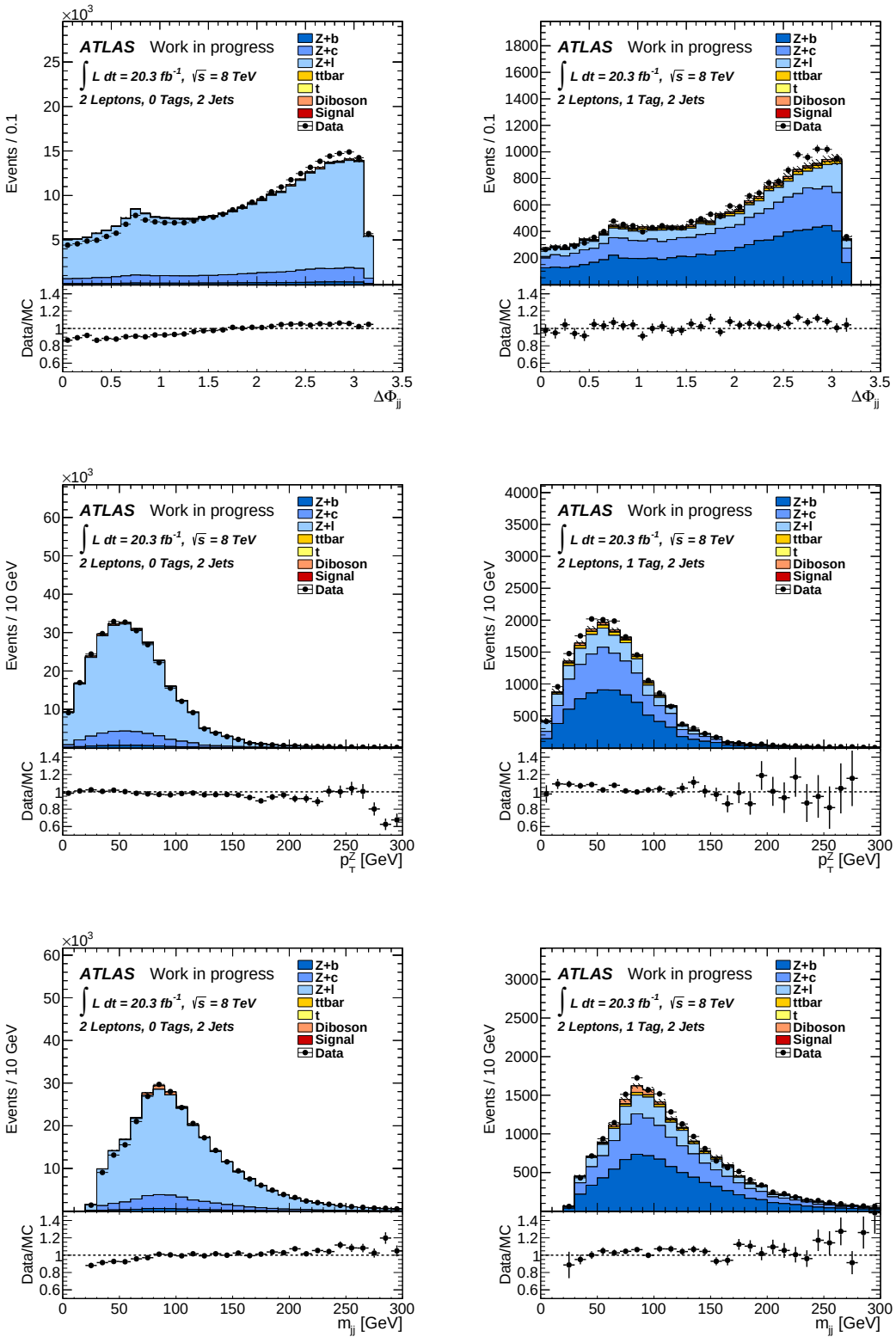

Figure 4.6: Distributions of $\Delta\phi_{jj}$ (top), p_T^Z (middle) and m_{jj} (bottom) for the 0-tag (left) and 1-tag (right) 2-jet region before applying the $\Delta\phi$ correction described in the text.

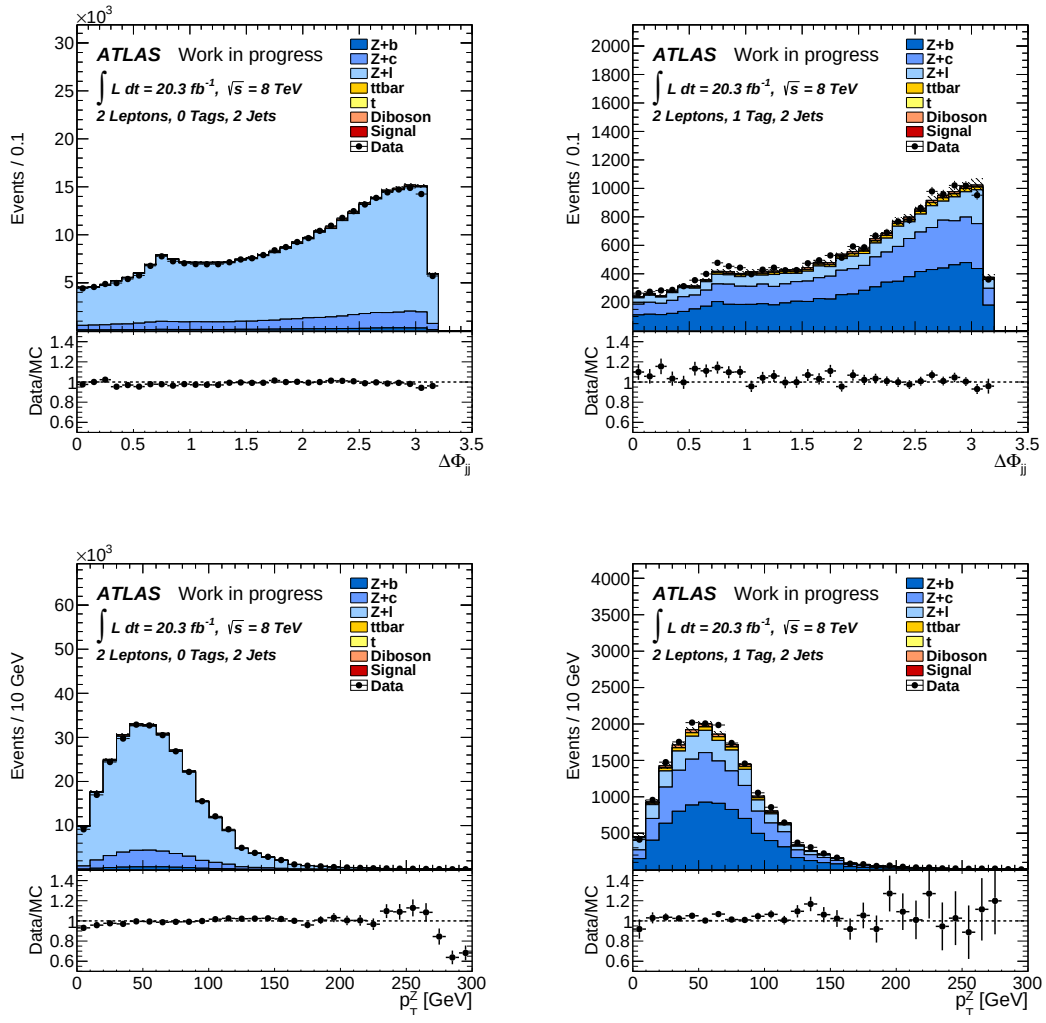

Figure 4.7: Distributions of $\Delta\phi_{jj}$ (upper) and p_T^Z (lower) for the 0-tag (left) and 1-tag (right) 2-jet region after applying the $\Delta\phi$ correction described in the text.

2-tag, 2-jet					
p_T^Z [GeV]	0-90	90-120	120-160	160-200	> 200
BTag	$\pm 4.9\%$	$\pm 4.8\%$	$\pm 5.2\%$	$\pm 5.8\%$	$\pm 8.6\%$
JES	$\pm 3.2\%$	$\pm 3.7\%$	$\pm 4.4\%$	$\pm 4.6\%$	$\pm 4.4\%$
Combined	$\pm 5.9\%$	$\pm 6.0\%$	$\pm 6.8\%$	$\pm 7.4\%$	$\pm 9.6\%$
2-tag, 3-jet					
p_T^Z [GeV]	0-90	90-120	120-160	160-200	> 200
BTag	$\pm 5.1\%$	$\pm 4.6\%$	$\pm 5.3\%$	$\pm 5.5\%$	$\pm 8.7\%$
JES	$\pm 6.8\%$	$\pm 3.7\%$	$\pm 6.5\%$	$\pm 7.0\%$	$\pm 4.0\%$
Combined	$\pm 8.5\%$	$\pm 5.9\%$	$\pm 8.4\%$	$\pm 9\%$	$\pm 9.6\%$

Table 4.2: Estimated systematic uncertainties on the $ZH \to l\bar{l}b\bar{b}$ signal for $m_H = 125\,\text{GeV}$ for the 2-jet and 3-jet signal regions for the systematic variations coming from b-tagging and JES. The combined systematic uncertainties are given as well.

ing detector uncertainties, modelling and theory uncertainties, and uncertainties coming from methods used in the calibrations.

In general, varying the nuisance parameters within the one σ deviations provides a reasonable result of the fit. If the parameters are varied much larger than one σ or the variations are too one-sided, the fit most likely behaves in an unwanted way or does not converge, which affects the result negatively.

The systematic uncertainties for the sources mentioned above are estimated for the different p_T^Z regions of the 2-jet and 3-jet signal region, assuming the uncertainties for b-tagging and JES respectively are not correlated. The uncertainties on the $ZH \to l\bar{l}b\bar{b}$ signal with $m_H = 125\,\text{GeV}$ and on the total background are considered separately. The results for the estimated systematic uncertainties can be seen in Tab. 4.2 and 4.3.

Fig. 4.8, Fig. 4.9, Fig. 4.10, and Fig. 4.11 show the b-tagging and JES systematic variations for the m_{bb} distributions in the 2-jet and 3-jet signal regions, which have been found to have the largest contribution to the systematic uncertainties shown in Tab. 4.2 and 4.3. The relative deviations from the nominal distribution (zero-line) for the one σ up and down variation are shown.

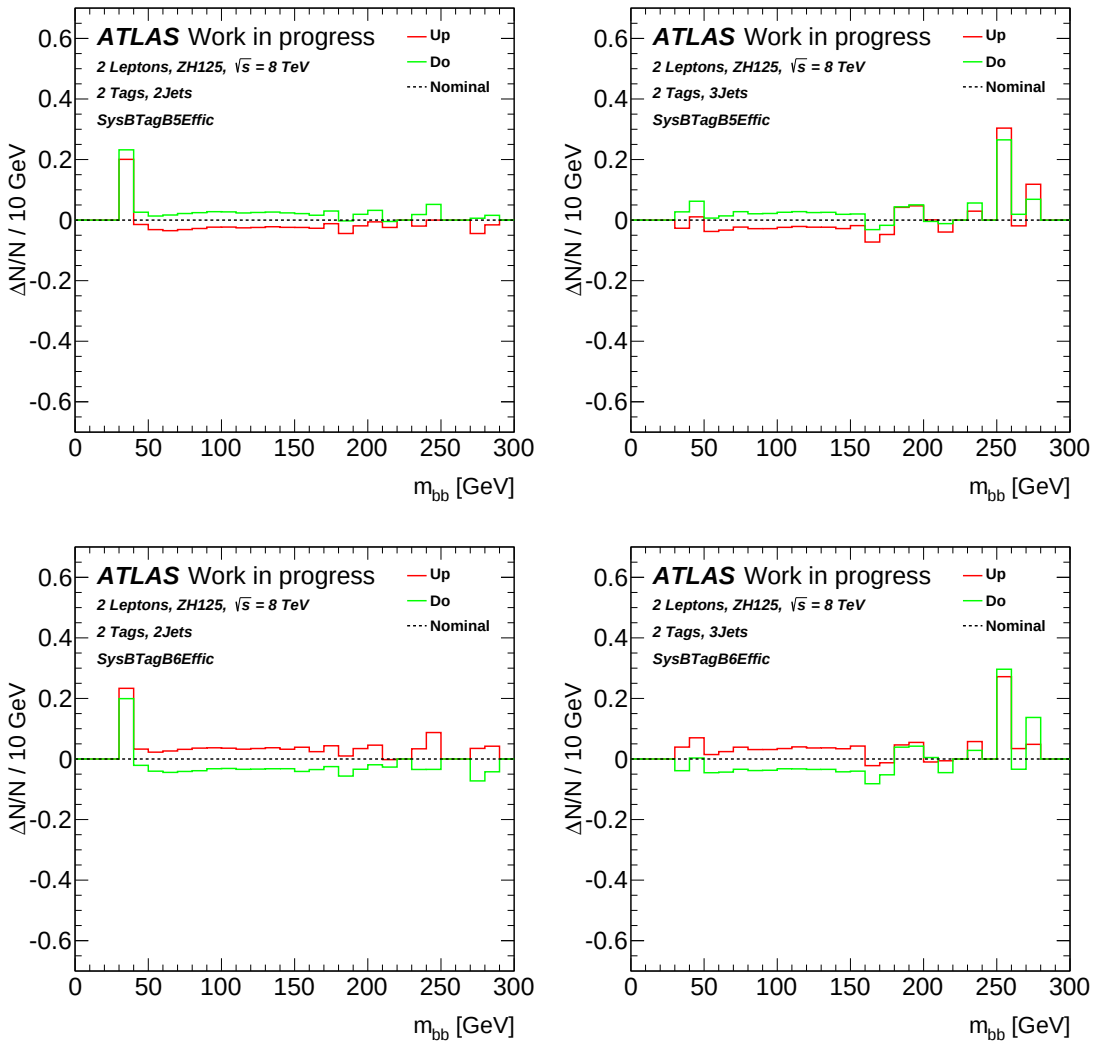

Figure 4.8: Relative one σ deviations for the b-tagging systematic variations on the $ZH \to l\bar{l}b\bar{b}$ signal for $m_H = 125$ GeV with the highest contribution to the systematic b-tagging uncertainty, taken from the m_{bb} distributions in the 2-jet (left) and 3-jet (right) signal regions.

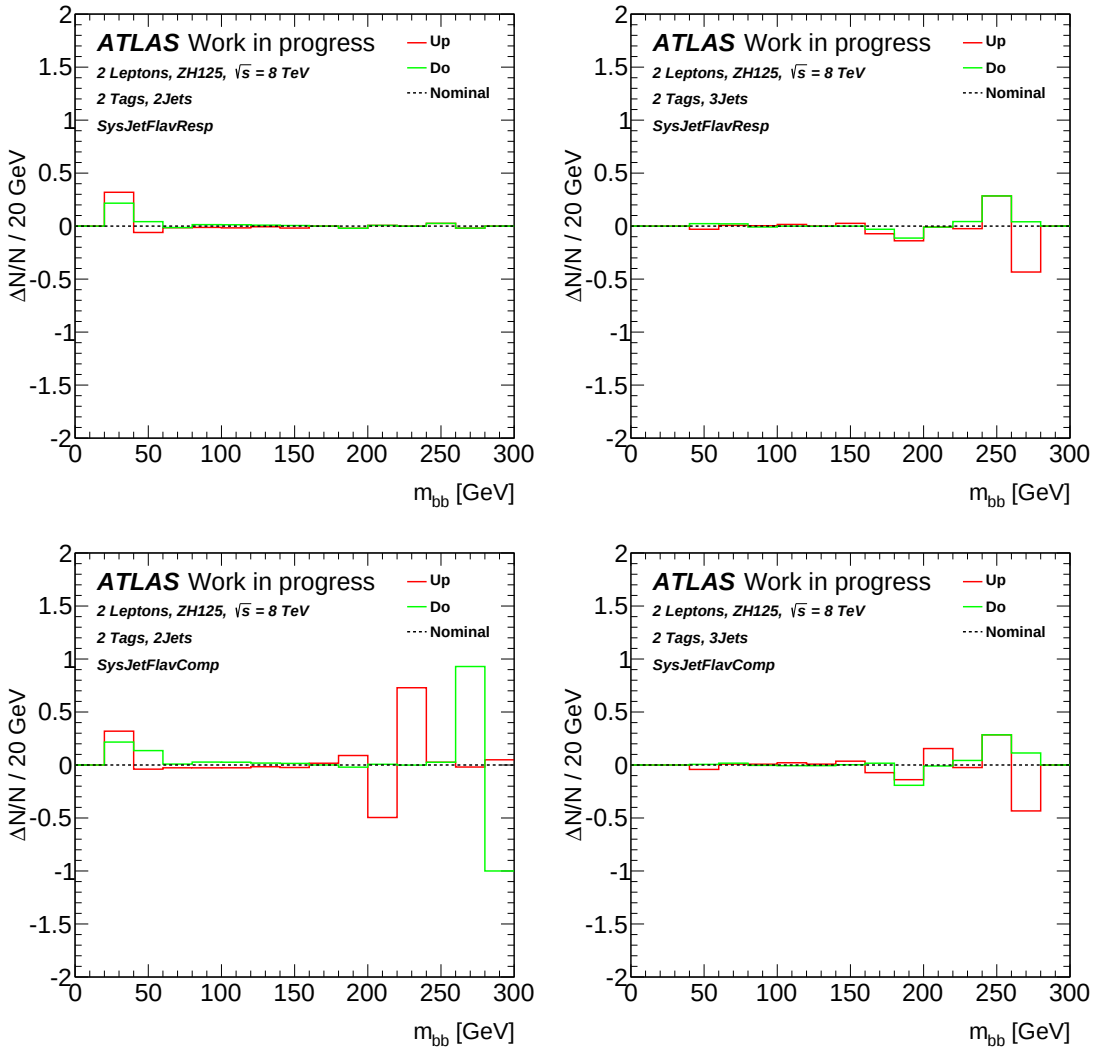

Figure 4.9: Relative one σ deviations for the JES systematic variations on the $ZH \to l\bar{l}b\bar{b}$ signal for $m_H = 125\,\text{GeV}$ with the highest contribution to the systematic JES uncertainty, taken from the m_{bb} distributions in the 2-jet (left) and 3-jet (right) signal regions.

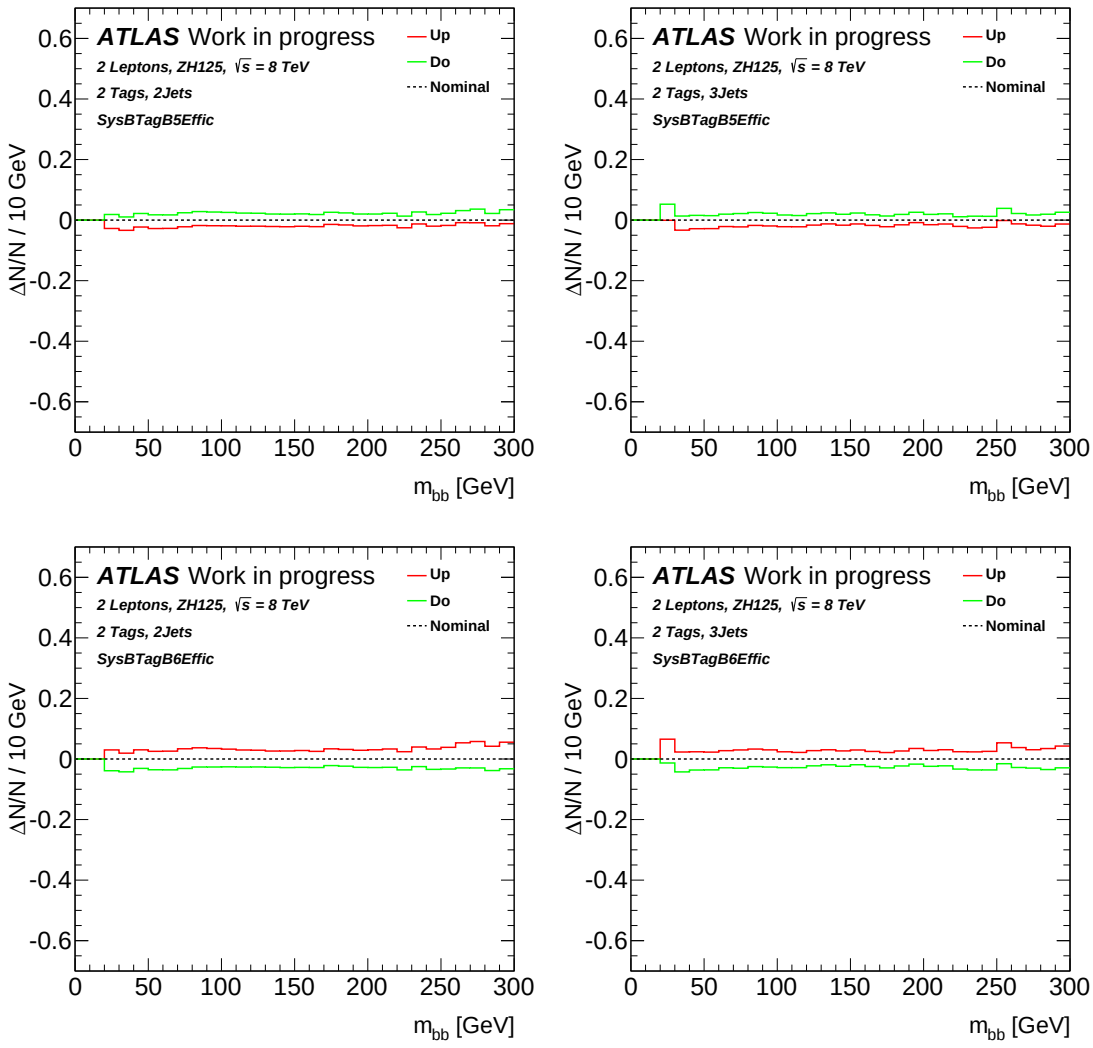

Figure 4.10: Relative one σ deviations for the b-tagging systematic variations on the total background with the highest contribution to the systematic b-tagging uncertainty, taken from the m_{bb} distributions in the 2-jet (left) and 3-jet (right) signal regions.

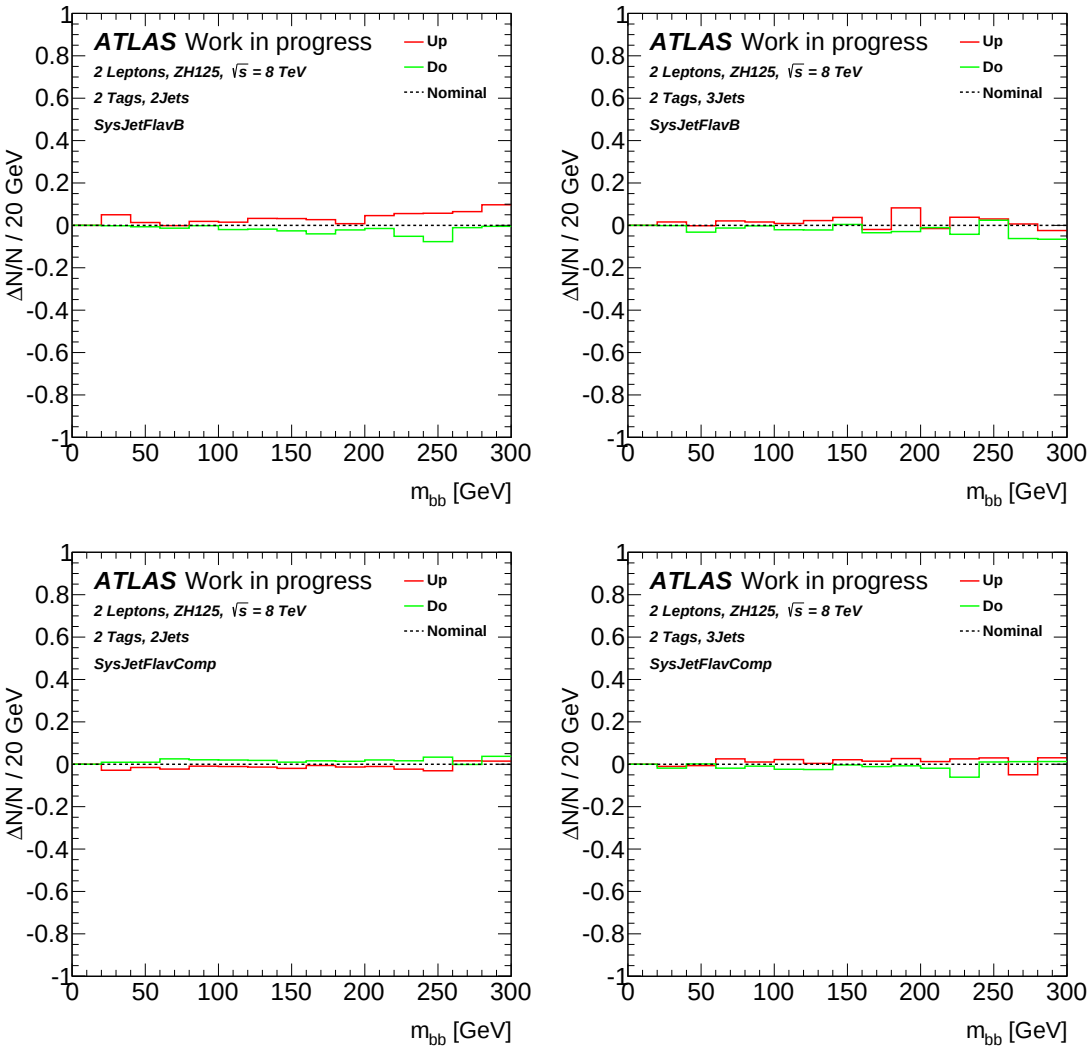

Figure 4.11: Relative one σ deviations for the JES systematic variations on the total background with the highest contribution to the systematic JES uncertainty, taken from the m_{bb} distributions in the 2-jet (left) and 3-jet (right) signal regions.

2-tag, 2-jet					
p_T^Z [GeV]	0-90	90-120	120-160	160-200	> 200
BTag	$\pm 4.5\%$	$\pm 4.5\%$	$\pm 4.3\%$	$\pm 5.1\%$	$\pm 8.2\%$
JES	$\pm 3.6\%$	$\pm 2.6\%$	$\pm 2.7\%$	$\pm 5.5\%$	$\pm 4.5\%$
Combined	$\pm 5.8\%$	$\pm 5.2\%$	$\pm 5.1\%$	$\pm 7.5\%$	$\pm 9.4\%$
2-tag, 3-jet					
p_T^Z [GeV]	0-90	90-120	120-160	160-200	> 200
BTag	$\pm 4.1\%$	$\pm 4.1\%$	$\pm 4.1\%$	$\pm 4.5\%$	$\pm 6.9\%$
JES	$\pm 7.3\%$	$\pm 6.3\%$	$\pm 1.7\%$	$\pm 2.6\%$	$\pm 7.2\%$
Combined	$\pm 8.3\%$	$\pm 7.6\%$	$\pm 4.4\%$	$\pm 5.2\%$	$\pm 10\%$

Table 4.3: Estimated systematic uncertainties on the total background for the 2-jet and 3-jet signal regions for the systematic variations coming from b-tagging and JES. The combined systematic uncertainties are given as well.

4.5 Results

In the following sections the studies and their results of the search for a Higgs boson in the $ZH \to l\bar{l}b\bar{b}$ channel with data taken at the ATLAS detector in 2012 will be outlined. These studies include the nominal analysis in Section 4.5.1 following the one described in [10], and two studies regarding the jet-selection for the reconstruction of the Higgs boson in Section 4.5.2 and 4.5.3.

4.5.1 Signal Strength

This section presents the results for the analysis of the $ZH \to l\bar{l}b\bar{b}$ channel at $\sqrt{s} = 8$ TeV. The main variable to determine if there is a significant contribution of the signal coming from the Higgs boson in the $ZH \to l\bar{l}b\bar{b}$ decay is the invariant mass of the two jets used to reconstruct the Higgs boson. As already mentioned in Section 4.3.1 this signal region obtained by the selection described in Section 4.2.1 and 4.2.2 is divided in two regions with two and three signal jets in the event topology, which are shown in Fig. 4.4. The respective event yields for these two regions for signal and background events can be seen in Tab. 4.4. The yields for the signal events are taken from the MC sample with a Higgs mass of 125 GeV. The ratio of signal to background $\frac{S}{B}$, which can be used to estimate the sensitivity of the analysis to the signal in the different regions, is also given. The combined statistical and systematic relative uncertainties for the total background in Tab. 4.4 are outlined in Tab. 4.5.

From these numbers no significant excess for a Higgs boson is expected with the data considered for this analysis. But an upper limit on the cross-section σ for

2-tag, 2-jet					
p_T^Z [GeV]	0-90	90-120	120-160	160-200	> 200
$ZH \to l\bar{l}b\bar{b}$	10	2.6	2.0	1.0	1.1
Zb	1252	266	98	21	15
Zc	149	27	10	2.5	5.7
Zl	17	2.8	1.1	0.3	3.9
Top	335	59	13	0.3	0.2
Diboson	76	14	8.5	3.7	3.4
Total background	1829 ± 106	369 ± 20	131 ± 7.2	28 ± 2.3	28 ± 2.8
Data	2186	437	140	40	20
$\frac{S}{B}$	0.005	0.007	0.01	0.04	0.04
2-tag, 3-jet					
p_T^Z [GeV]	0-90	90-120	120-160	160-200	> 200
$ZH \to l\bar{l}b\bar{b}$	4.6	1.4	1.1	0.6	0.6
Zb	771	162	78	22	20
Zc	130	27	12	3.7	9.5
Zl	34	6.2	2.7	0.9	7.6
Top	243	41	11	1.1	0.1
Diboson	29	6.8	4.6	2.2	2.2
Total background	1207 ± 102	243 ± 19	108 ± 5.4	30 ± 1.9	39 ± 4.1
Data	1384	252	137	32	26
$\frac{S}{B}$	0.004	0.006	0.01	0.02	0.01

Table 4.4: Event yields for signal and background samples and recorded 2012 data for the signal 2-jet and 3-jet regions. Signal yields are taken from the MC sample with a Higgs mass of 125 GeV. The errors correspond to the combined statistical and systematic relative uncertainties on the total background as outlined in Tab. 4.5.

a Higgs boson with mass around 125 GeV in the $ZH \to l\bar{l}b\bar{b}$ channel can be placed to confirm the validity of the predictions made by the Standard Model. For this purpose a binned likelihood fit [10, 23] is used to set an upper exclusion limit on the signal strength $\mu = \frac{\sigma}{\sigma_{SM}}$ at 95% Confidence Level (C. L.), with σ_{SM} being the cross-section of the $ZH \to l\bar{l}b\bar{b}$ signal predicted by the Standard Model. The fit is performed by a tool, which is also used in the analysis described in [10].

For the fit, binned likelihood functions $\mathcal{L}(\mu, \theta)$ are constructed by multiplication of terms of Poisson probabilities, using the input m_{jj} distributions from all signal and control regions mentioned in Section 4.3.1. These inputs are provided for the $ZH \to l\bar{l}b\bar{b}$ signal, the nine backgrounds (see Section 4.1) and the recorded 2012 data. To describe the impact of systematic uncertainties, the likelihood func-

p_T^Z [GeV]	0-90	90-120	120-160	160-200	> 200
2Jet	$\pm 5.8\%$	$\pm 5.3\%$	$\pm 5.5\%$	$\pm 8.4\%$	$\pm 10\%$
3Jet	$\pm 8.4\%$	$\pm 7.8\%$	$\pm 5.0\%$	$\pm 6.6\%$	$\pm 11\%$

Table 4.5: Combined statistical and systematic uncertainties on the total background for the 2-jet and 3-jet signal region. Systematic uncertainties estimated in Section 4.4 and statistical uncertainties taken from the MC m_{bb} distributions are taken into account.

Zb	Zc	$t\bar{t}$
1.19 ± 0.017	0.83 ± 0.017	1.06 ± 0.0098

Table 4.6: Rescaling factors for the main backgrounds after the fit with statistical uncertainties only.

tion $\mathcal{L}(\mu, \theta)$ is parametrised by the respective nuisance parameters θ (see Section 4.4), in form of Gaussian or log-normal priors. The test statistic

$$q_\mu = -2 \ln \frac{\mathcal{L}(\mu, \hat{\hat{\theta}})}{\mathcal{L}(\hat{\mu}, \hat{\theta})} \tag{4.2}$$

is used to determine the compatibility of the background-only hypothesis with the observed data and to determine exclusion limits with the CL_s method [23] for a Higgs boson over the mass range 110 - 150 GeV. The parameters $\hat{\mu}$ and $\hat{\theta}$ maximise the likelihood $\mathcal{L}(\hat{\mu}, \hat{\theta})$, with the constraint $0 \leq \hat{\mu} \leq \mu$ on $\hat{\mu}$ for a test value μ of the signal strength. The nuisance parameters $\hat{\hat{\theta}}$ maximise the likelihood $\mathcal{L}(\mu, \hat{\hat{\theta}})$ for a given value of μ. The normalisations of the backgrounds Zb, Zc, and $t\bar{t}$ are kept floating to allow the fit to correct their normalisations to agree with the measurement of the recorded data (see Section 4.3.2).

The fit is first done with statistical uncertainties only, which are provided by the input distributions, and then also including the systematic uncertainties mentioned in Section 4.4. The rescaling factors for the backgrounds from the fit performed with statistical uncertainties only can be seen in Tab. 4.6. These numbers are comparable to the scaling factors mentioned in [10].

When performing the fit with the systematic uncertainties mentioned in Section 4.4, some issues occur which affect the result for the exclusion limit. The fit does not converge properly and some nuisance parameters are varied quite heavily. The scaling factors of Zb, Zc, and $t\bar{t}$ (see Tab. 4.7) get much larger errors indicating heavy correlations with the nuisance parameters. These correlations, of course, also affect the exclusion limits.

Zb	Zc	$t\bar{t}$
1.34 ± 0.091	0.59 ± 0.15	1.13 ± 0.054

Table 4.7: Rescaling factors for the main backgrounds after the fit with systematic uncertainties included.

	stat. unc. only	with syst. unc.
exp.	$3.17^{+1.24}_{-0.88}$	$3.85^{+1.51}_{-1.08}$
obs.	2.66	2.40

Table 4.8: Expected and observed exclusion limits on μ at 95% C. L. for a Higgs boson with mass 125 GeV in the $ZH \to l\bar{l}b\bar{b}$ channel, for statistical uncertainties only and with systematic uncertainties included.

Finally, the expected and observed exclusion limit on μ at 95% C. L. for a Higgs boson with mass 125 GeV in the $ZH \to l\bar{l}b\bar{b}$ channel for $20.3\,\text{fb}^{-1}$ of recorded 2012 data is shown in Tab. 4.8.

The expected and observed exclusion limits for a Higgs boson with mass between 110 and 150 GeV is shown in Fig. 4.12, for the statistical uncertainties only fit. Cross-sections for a Higgs boson produced in the $ZH \to l\bar{l}b\bar{b}$ channel above these limits times the cross-section predicted by the Standard Model can be excluded at 95% C. L. . The expected limit is obtained by assuming that the recorded data is equal to the background expectations, to get an estimate on how sensitive the analysis is [23]. If the exclusion limit for a Higgs boson of a certain mass is found to be significantly smaller than one, a Standard Model Higgs boson with this mass can be excluded for the considered channel. The distributions for the different regions (see Section 4.3.1) with the scale factors in Tab. 4.6 applied are shown in Fig. 4.13 and 4.14.

The good agreement of data and MC again validates the results gained from the fit with statistical uncertainties only. The event yields for the 2-jet and 3-jet signal region with the scale factors applied is shown in Tab. 4.9.

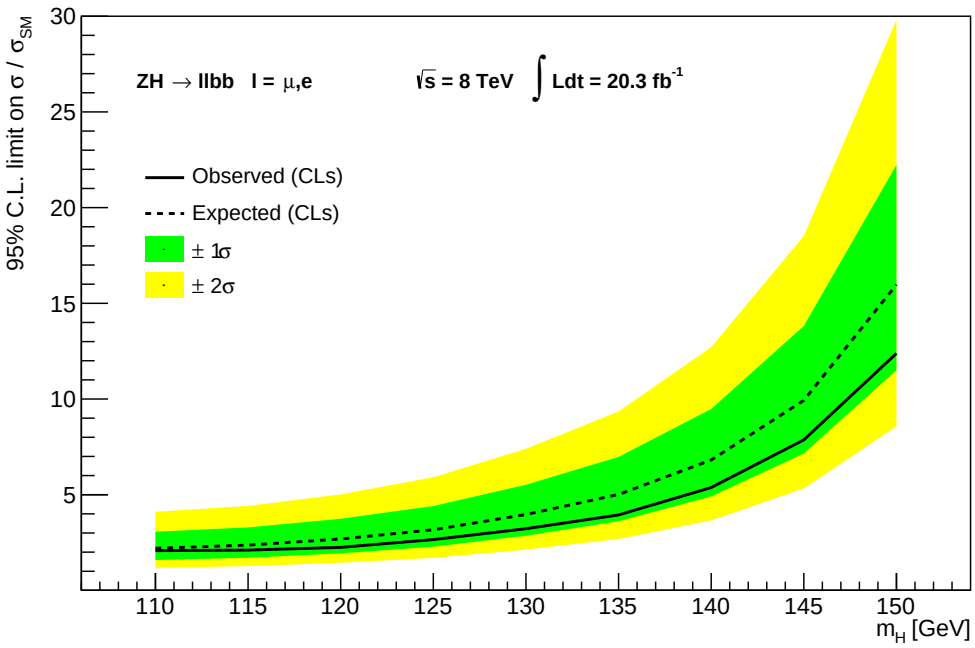

Figure 4.12: Expected (dotted line) and observed (straight line) limit for μ at 95% C. L. in the ZH $\rightarrow$ l$\bar{\text{l}}$b$\bar{\text{b}}$ channel for 20.3 fb^{-1} of recorded data. Only statistical uncertainties are taken into account. The one and two σ deviations are indicated as green and yellow bands around the expected limit.

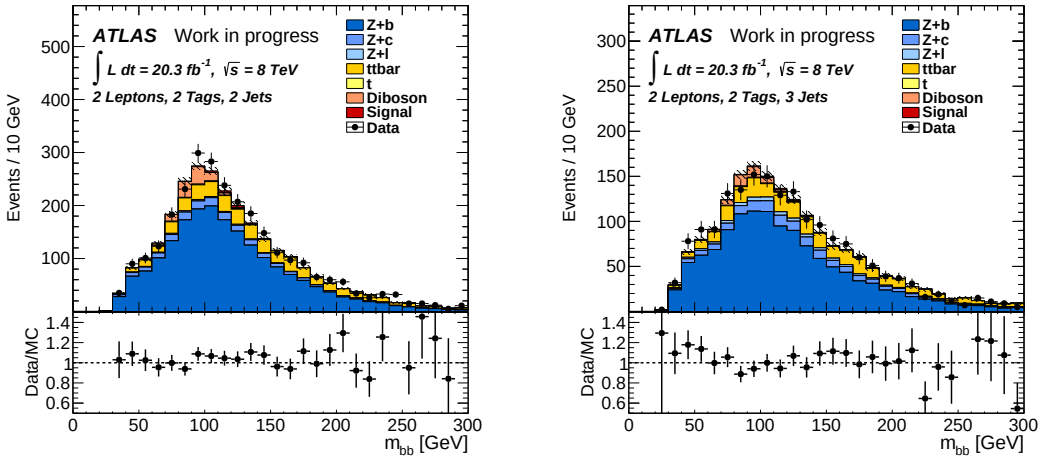

Figure 4.13: Signal regions with two (left) and three (right) jets in the selection after applying the factors in Tab. 4.6.

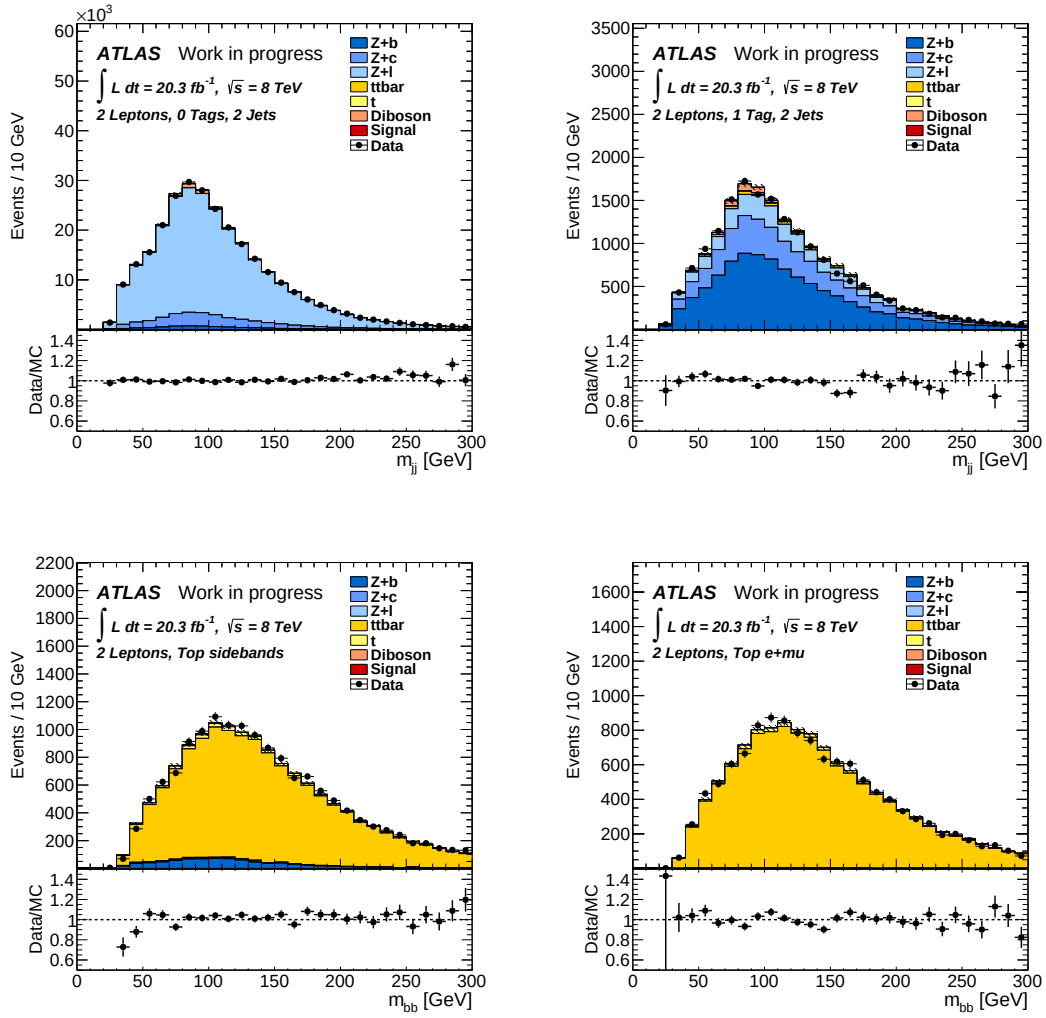

Figure 4.14: 0-tag (top left) and 1-tag (top right) region and top control regions from selection on m_{ll} sidebands (bottom left) and on one muon and one electron (bottom right) after applying the factors in Tab. 4.6.

2-tag, 2-jet					
p_T^Z [GeV]	0-90	90-120	120-160	160-200	> 200
$ZH \to l\bar{l}b\bar{b}$	10	2.6	2.0	1.0	1.1
Zb	1490	316	116	25	18
Zc	124	22	8.6	2.1	4.7
Zl	17	2.8	1.1	0.3	3.9
Top	355	62	14	0.4	0.2
Diboson	76	14	8.5	3.7	3.4
Total background	2062 ± 120	417 ± 22	148 ± 8.2	32 ± 2.6	30 ± 3.0
Data	2186	437	140	40	20
$\frac{S}{B}$	0.005	0.006	0.01	0.03	0.04
2-tag, 3-jet					
p_T^Z [GeV]	0-90	90-120	120-160	160-200	> 200
$ZH \to l\bar{l}b\bar{b}$	4.6	1.4	1.1	0.6	0.6
Zb	918	193	93	26	23
Zc	108	22	9.9	3.1	7.9
Zl	34	6.2	2.7	0.9	7.6
Top	257	43	11	1.2	0.1
Diboson	29	6.8	4.6	2.2	2.2
Total background	1346 ± 113	271 ± 21	121 ± 6.0	33 ± 2.2	41 ± 4.3
Data	1384	252	137	32	26
$\frac{S}{B}$	0.003	0.005	0.009	0.02	0.01

Table 4.9: Event yields for signal and background samples and recorded 2012 data for the signal 2-jet and 3-jet regions after applying the factors in Tab. 4.6. Signal yields are taken from the MC sample with a Higgs mass of 125 GeV. The errors correspond to the combined statistical and systematic relative uncertainties on the total background as outlined in Tab. 4.5.

4.5.2 Further Study of an FSR Correction for 3-Jet Events

In this section a study regarding the signal topology with three jets is presented. Tab. 4.9 shows, that there is a significant contribution of these 3-jet events for the $ZH \to l\bar{l}b\bar{b}$ signal. The third jet can originate from multiple processes, being initial state radiation (ISR), final state radiation (FSR), or different modes for the production of the initial Z boson in the ZH channel. ISR and FSR come from gluons which can be radiated from quarks as shown in Fig. 4.15. An example for different production modes of the Z boson can be seen in Fig. 4.16. The contribution of these modes with a quark and a gluon in the initial state is expected to be the dominant one, since quark-gluon interactions are more likely to occur in high

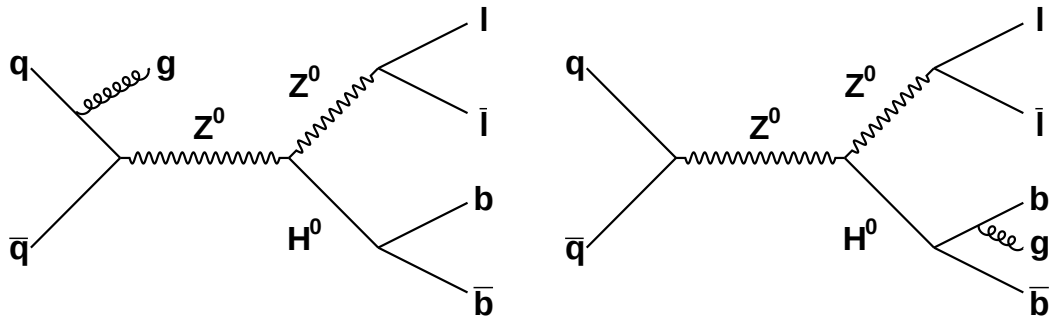

Figure 4.15: Examples for 3-jet events originating from ISR (left) and FSR (right) events.

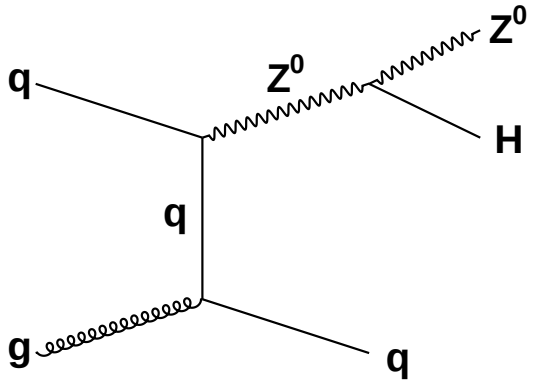

Figure 4.16: Example for 3-jet events originating from different production modes of the initial Z boson.

energy proton-proton-collisions than quark-anti-quark interactions.

The m_{bb} distributions of the 2-jet and 3-jet signal region for the signal sample of a Higgs boson with mass 125 GeV (see Fig. 4.17) show a significant shift to lower masses if there is an additional jet in the signature. This can be due to the contribution of FSR events, where the third jet is not taken into account for the Higgs boson reconstruction. To correct for these missing contributions it can be attempted to find parameters to discriminate FSR processes from the other 3-jet processes. These parameters would allow to take the third jet into account for the Higgs boson mass, thus improving the Higgs mass resolution.

One property of a third jet coming from FSR, which can be exploited, is its small angular distance to one of the two b-jets from the Higgs boson, since it originates from one of these jets. The angular distance of the third jet to the

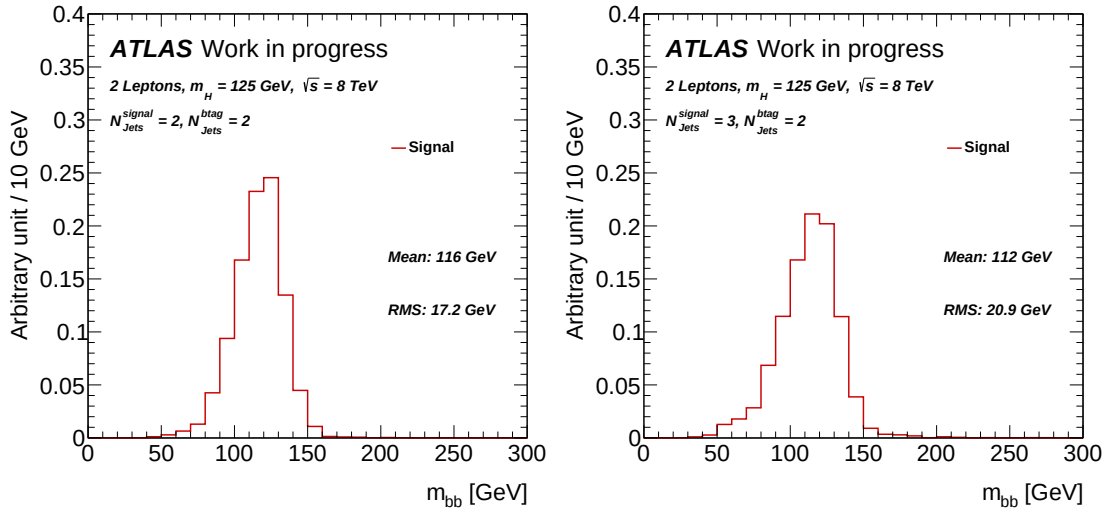

Figure 4.17: Distribution of m_{bb} for the 2-jet (left) and 3-jet (right) signal region. Normalisations have been scaled to one.

nearest of the two b-jets b_1 and b_2 can be defined as

$$\Delta R_{min}^{3rd\,jet} = \min\left(\Delta R(j_{3rd}, b_1), \Delta R(j_{3rd}, b_2)\right). \tag{4.3}$$

Fig. 4.18 shows the distribution of the invariant mass m_{bbj} reconstructed from the two b-jets and a third jet for the $ZH \to l\bar{l}b\bar{b}$ signal sample with $m_H = 125$ GeV with different upper cut values on $\Delta R_{min}^{3rd\,jet}$. By reducing the cut value to lower values the contributions not coming from FSR get more suppressed and the distribution narrows to a peak between 120 and 130 GeV, which is to be expected for a Higgs boson with mass 125 GeV. A cut value of $\Delta R_{min}^{3rd\,jet} < 0.8$ is found to be most suitable for the discrimination of jets coming from FSR. Comparing the m_{bbj} distribution with the m_{bb} one taken from 3-jet events (see Fig. 4.19), the expected shift to higher masses to the peak around 125 GeV can be seen. The addition of the third jet, however, also leads to high mass contributions, which results in a large tail in the distribution. These contributions most likely originate from non-FSR processes which pass the $\Delta R_{min}^{3rd\,jet}$ cut. To further suppress these contributions an additional constraint on the p_T of the third jet is applied. This constraint demands that

$$p_T^{3rd\,jet} < \min\left(p_T^{b_1}, p_T^{b_2}\right), \tag{4.4}$$

since $p_T^{3rd\,jet}$ is expected to be smaller than the p_T of the b-jets (from which it originates). The comparison between the distributions of m_{bbj} for constrained and unconstrained $p_T^{3rd\,jet}$ are shown in Fig. 4.20. The constraint reduces the tail of the

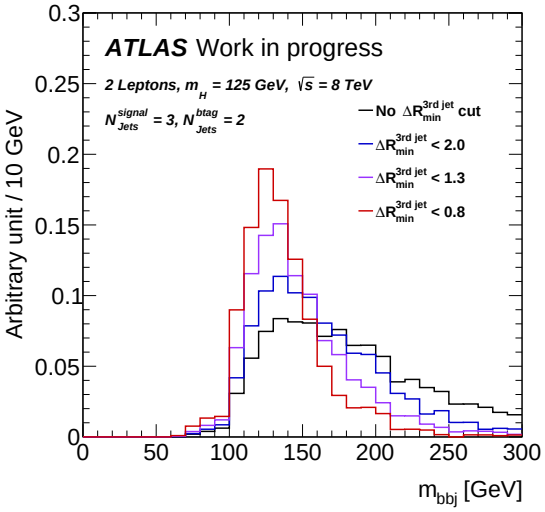

Figure 4.18: Distributions of m_{bbj} for different cuts on $\Delta R_{min}^{3rd\,jet}$. Normalisations have been scaled to one.

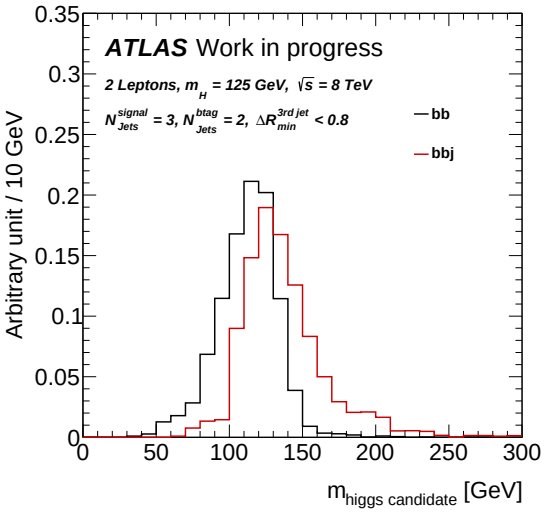

Figure 4.19: Distribution of m_{bb} (black) for all 3-jet events and m_{bbj} (red) for 3-jet events which pass $\Delta R_{min}^{3rd\,jet} < 0.8$. Normalisations have been scaled to one.

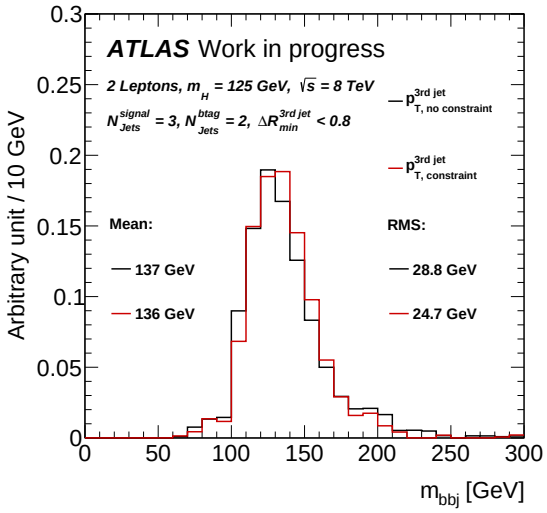

Figure 4.20: Distribution of m_{bbj} with (red) and without (black) constraint on $p_T^{3rd\,jet}$. Normalisations have been scaled to one.

	2/3-jet	3-jet	$\Delta R_{min}^{3rd\,jet} < 0.8$
$ZH \to l\bar{l}b\bar{b}$	25	8.4 (34%)	1.5 (6.0%)
Z+Jets	3106	1257 (40%)	171 (5.3%)
Top	681	284 (42%)	40 (5.8%)
Diboson	150	45 (30%)	6.2 (4.1%)
$\frac{S}{B}$	0.006	0.005	0.007

Table 4.10: Event yields for the 2-jet and 3-jet signal regions combined, the 3-jet signal region and the FSR corrected 3-jet region.

distribution and narrows the distribution in general, which can also be seen in the Root Mean Square (RMS) of the distribution dropping from 28.8 to 24.7 GeV.

The signal and background m_{bb} distributions for the 3-jet signal region, where $\Delta R_{min}^{3rd\,jet} < 0.8$ is fulfilled (with and without the constraint on $p_T^{3rd\,jet}$), can be seen in Fig. 4.21. These distributions show the main problem of this correction of FSR jet events, which is the small contribution of events which fulfil the FSR cut to the 3-jet events. This also becomes apparent when looking at event yields in Tab. 4.10 for the $ZH \to l\bar{l}b\bar{b}$ signal with $m_H = 125$ GeV and the different backgrounds. The contribution to the combined 2-jet and 3-jet region is only $\sim 6\%$ for both the signal and the backgrounds. Due to this, only a small improvement (if any) can be expected from this correction and the statistical description of the FSR region is limited by high statistical uncertainties. Fig. 4.22 shows how the different background m_{bb} distributions shift relative to the signal one when moving from the

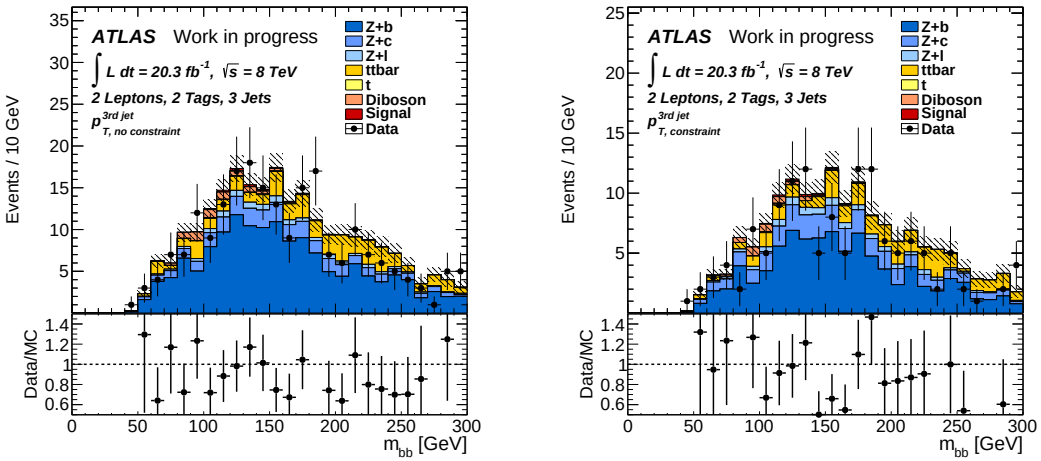

Figure 4.21: Distributions of m_{bb} for the 3-jet signal region, where $\Delta R_{min}^{3rd\,jet} < 0.8$ is fulfilled, without (left) and with (right) the constraint on $p_T^{3rd\,jet}$.

nominal 3-jet signal region to the FSR region. The backgrounds shift in the same way as the signal, except for the top background, which is shifted more out of the peak-window of the signal. This also indicates that there is no significant improvement to be expected, since the dominant Z+jets background is not shifted out of the window around the signal mass peak.

The impact of this treatment to the 3-jet distribution of the reconstructed Higgs mass can be seen in Fig. 4.23 for the approach with and without the constraint on $p_T^{3rd\,jet}$. The correction shifts the mass distribution to higher values, which is in better agreement with the distribution coming from 2-jet events (see Fig. 4.17).

To estimate the impact of the FSR correction on the nominal analysis, the limit fit, which is described in Section 4.5.1, is performed with this correction applied. For this purpose the 3-jet signal region is split into two regions, one where the third jet fulfils $\Delta R_{min}^{3rd\,jet} < 0.8$, with m_{bbj} as input, and one where this cut is not passed, using m_{bb} as input. The fit is performed with statistical uncertainties only. The results for the expected and observed exclusion limit with the FSR correction applied with and without $p_T^{3rd\,jet}$ constraint are shown in Tab. 4.11. As already expected from the event yields in Tab. 4.10 no significant improvement is achieved by applying the FSR correction in 3-jet signal events.

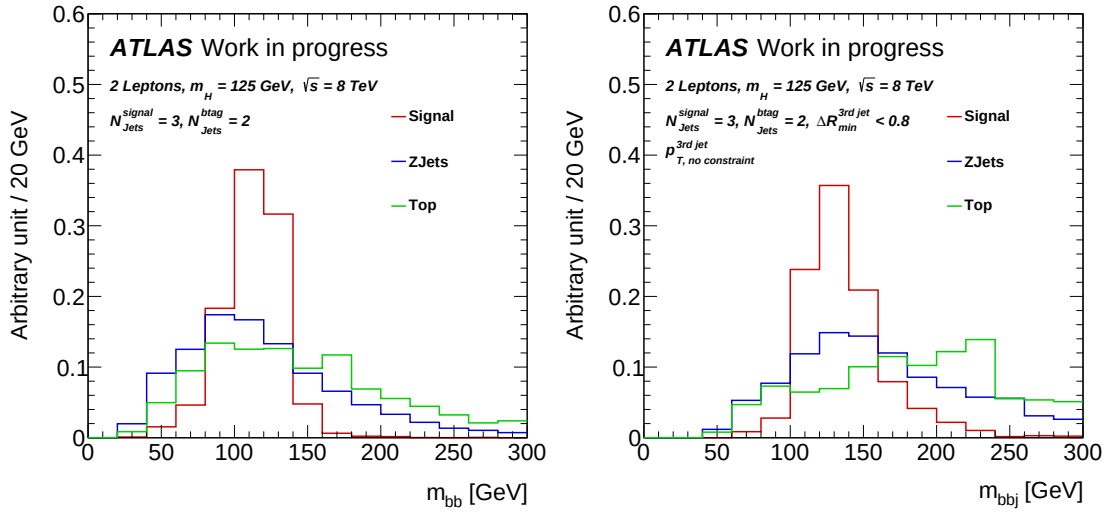

Figure 4.22: Signal and background m_{bb} distributions for the 3-jet signal regions (left), and the FSR 3-jet region (right). Normalisations have been scaled to one.

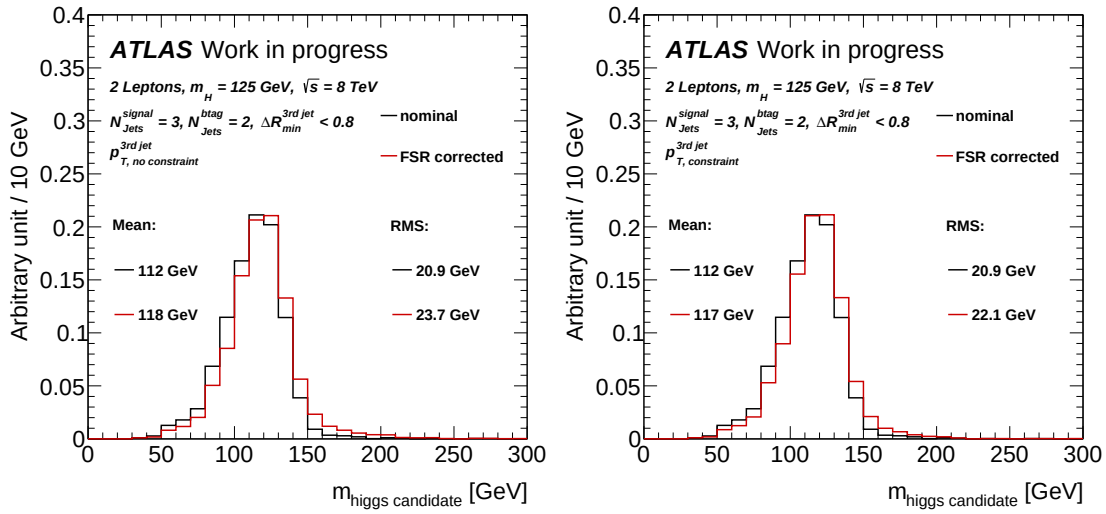

Figure 4.23: Distribution of the reconstructed Higgs mass in the 3-jet region with (left) and without (right) constraint on $p_T^{3rd\ jet}$. Normalisations have been scaled to one.

	nominal	no $p_T^{3rd\,jet}$ constraint	with $p_T^{3rd\,jet}$ constraint
exp.	$3.17^{+1.24}_{-0.88}$	$3.16^{+1.24}_{-0.88}$	$3.17^{+1.24}_{-0.89}$
obs.	2.66	2.79	2.79

Table 4.11: Expected and observed exclusion limits of the nominal analysis, and with the FSR correction applied with and without $p_T^{3rd\,jet}$ constraint, as described in the text.

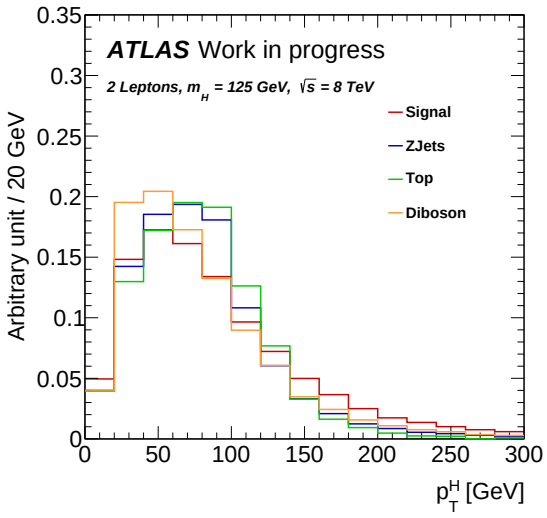

Figure 4.24: Distribution of the reconstructed Higgs p_T for the ZH $\rightarrow l\bar{l}b\bar{b}$ signal and the different backgrounds. Normalisations have been scaled to one.

4.5.3 Further Study of Cambridge-Aachen Jets in the Boosted Higgs Regime

This section presents a study on jet selection in the boosted Higgs boson regime. As already shown before (see Section 4.2.2) the sensitivity of the ZH $\rightarrow l\bar{l}b\bar{b}$ search increases when considering regions of high p_T^Z (see Fig. 4.1). The difference in sensitivity of the boosted and not boosted regime can also be seen in the distribution of the reconstructed Higgs boson p_T in Fig. 4.24.

A possible way to improve the boosted Higgs boson region of the analysis is the usage of the Cambridge-Aachen (CA) algorithm, as described in Section 3.3.1, which is optimised to a Higgs boson search in the boosted regime. To be able to make a comparison between jets selected by this algorithm and the anti-k_T algorithm used for the nominal analysis, a simple selection on the subjets, which are determined as outlined in Section 3.3.1, is performed. The selection on leptons, m_{ll}, E_T^{miss}, and ΔR_{jj} is kept the same (see Section 4.2.1 and 4.2.2). For

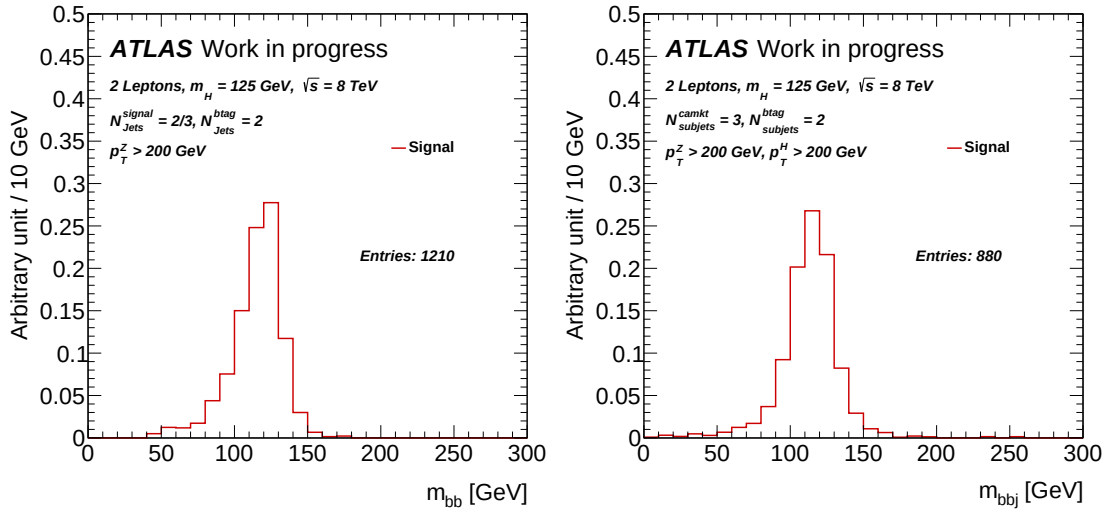

Figure 4.25: Distribution of the Higgs boson mass reconstructed by anti-k_T (left) and CA (right) jets. Normalisations have been scaled to one.

the reconstruction of the Higgs boson the highest p_T CA jet with exactly three subjets, with two of them being b-tagged, is selected. The mass of the Higgs boson is reconstructed by all three subjets. Additionally, a lower cut on the p_T of the Higgs boson of 200 GeV is applied. The high cut on p_T^H is required to suppress small mass contributions and ensure for a boosted Higgs boson regime.

The Higgs boson mass reconstructed by the two algorithms for the last p_T^Z region can be seen in Fig. 4.25. One problem becomes apparent immediately when looking at the number of events which pass the selection for the two different algorithms. A selection on CA jets yields $\sim$ 27% less signal events than the combined selection of anti-k_T jets in the 2-jet and 3-jet regions. This indicates, that only using CA jets instead of anti-k_T jets in this p_T^Z region may not give a significant improvement to the nominal analysis. The alternative is to combine the two jet types, by selecting either CA or anti-k_T jets first and then select the other jet type for events where the first selection was not successful. The event yields for the $ZH \to l\bar{l}b\bar{b}$ signal with $m_H = 125$ GeV and the different backgrounds can be seen in Tab. 4.12. Combining the two jet types improves the signal yield by $\sim$ 19 - 22% depending on which type is used first, since there is a big overlap between the two jet types for signal events. The overlap of background yield, however, is much smaller than for the signal, thus the event yield for the backgrounds increases as well by $\sim$ 128 - 131%. Due to these numbers no significant improvement is to be expected by combining CA and anti-k_T jets.

To estimate an improvement for the analysis, the limit fit in Section 4.5.1 is

	anti-k_T	CA	anti-k_T after CA	CA after anti-k_T
$ZH \to l\bar{l}b\bar{b}$	1.7	1.3	0.78	0.33
Zb	34	49	23	37
Zc	15	31	9.6	24
Zl	11	27	5.7	22
Top	0.28	0.038	0.28	0.038
Diboson	5.6	4.2	2.6	1.1
$\frac{S}{B}$	0.03	0.01	0.02	0.004

Table 4.12: Event yields for the selection of anti-k_T jets, CA jets, anti-k_T jets if no selection was made with CA jets, and CA jets if no selection was made with anti-k_T jets. To estimate an improvement by the CA selection, the first and fourth column combined or the second and third column combined have to be compared to the nominal yield (first column).

	anti-k_T 2-jet + 3-jet	anti-k_T first	CA first	only CA
exp.	$3.24^{+1.27}_{-0.91}$	$3.23^{+1.26}_{-0.90}$	$3.41^{+1.34}_{-0.95}$	$3.61^{+1.42}_{-1.01}$
obs.	2.52	2.42	2.49	3.15

Table 4.13: Expected and observed exclusion limits for the combined 2-jet and 3-jet signal region, for the selection of anti-k_T jets first, the selection on CA jets first, and the selection on only CA jets

performed with the implementation of CA jets. Since the separation in 2-jet and 3-jet signal regions is not possible for CA jets with the implementation described before, a signal region which combines these two regions is chosen as input for the fit. The contributions of the two jet types to the signal region are given in two separate regions in the last p_T^Z region, one for CA jets and one for anti-k_T jets. The result of the limit fit with statistical uncertainties only for a Higgs boson of mass 125 GeV is shown in Tab. 4.13. As expected the implementation of CA jets in the analysis gives no significant improvement to the exclusion limits. The result for only using CA jets is given as well, which also shows no improvement to the nominal analysis. The m_{bb} distributions of the respective selections on CA or anti-k_T jets can be seen in Fig. 4.26.

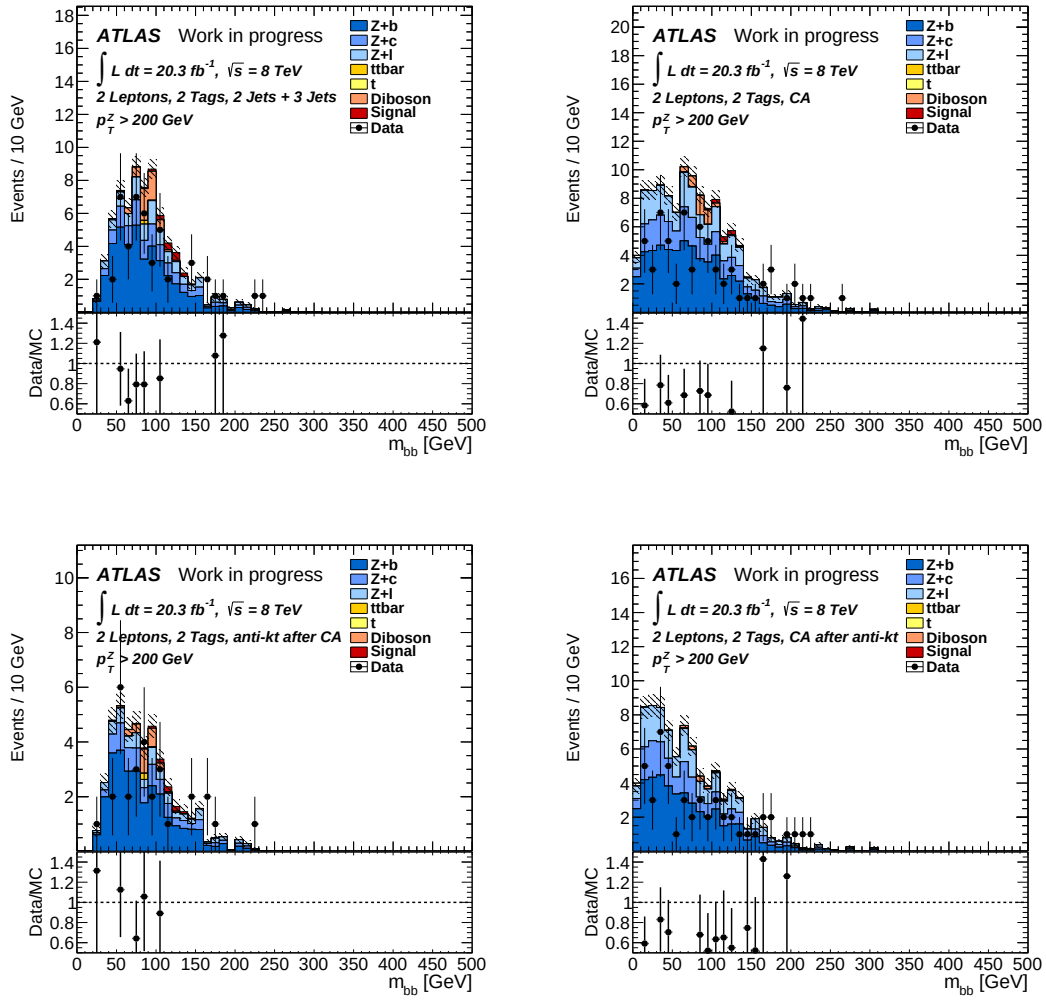

Figure 4.26: Distributions of m_{bb} for the 2-jet and 3-jet combined signal region (top left), selection of CA jets (top right), selection of anti-k_T jets if no CA was selected (bottom left), and selection of CA jets if no anti-k_T jet was selected in the last p_T^Z bin.

Chapter 5

Conclusion and Outlook

In this thesis a search for a Standard Model Higgs boson in the $ZH \to l\bar{l}b\bar{b}$ channel for the full data recorded in 2012 by ATLAS at a centre-of-mass energy of $\sqrt{s} = 8\,\text{TeV}$, corresponding to an integrated luminosity of approximately $20.3\,\text{fb}^{-1}$, was presented. The main region of interest is characterised by two leptons of same flavour and different charge to reconstruct the Z boson, and two or three jets, with two of them being b-tagged, to reconstruct the Higgs boson. In addition to these two signal regions (2-jet and 3-jet), multiple control regions were defined to constrain the different backgrounds for this channel in a binned likelihood fit, which was used to determine an upper exclusion limit of the signal strength $\mu = \frac{\sigma}{\sigma_{SM}}$. This fit was performed over a mass-range of the Higgs boson of 110 - 150 GeV, taking only statistical uncertainties into account and then also considering dominant systematic uncertainties. A Standard Model Higgs boson in the $ZH \to l\bar{l}b\bar{b}$ channel with mass 125 GeV could be excluded for cross-sections higher than $2.66 \cdot \sigma_{SM}$ at 95% C. L. when considering only statistical uncertainties. For a fit, where the systematic uncertainties considered are taken into account, the fit produces an exclusion limit at 95% C. L. of $2.40 \cdot \sigma_{SM}$. As discussed in Section 4.5.1, however, the stability of the fit with systematic uncertainties is heavily affected by correlations.

Two additional studies were presented, regarding a correction on final state radiation (FSR) events in the 3-jet signal region, and the implementation of the Cambridge-Aachen (CA) algorithm for jet selection in the boosted Higgs regime. For the study on FSR correction, a parameter was found to distinguish 3-jet events coming from FSR from other processes which generate a third jet in the signature. This allowed to take this third jet into account for the reconstruction of the Higgs boson mass, which improved the distribution of the reconstructed Higgs mass in the 3-jet signal region to be in a better agreement to the one in the 2-jet signal region. But the contribution of this FSR corrected 3-jet region to the combined 2-jet and 3-jet region was shown to be very small. This limits a possible improvement to

the whole analysis. To test if the correction on third jets coming from FSR events gives an improvement to the analysis, the likelihood fit was performed with the introduction of a separate FSR corrected 3-jet region. The results from this fit show no significant improvement for the implementation of the FSR correction in 3-jet events.

For the study of CA jets in the boosted Higgs regime, a comparison was made between a selection of the anti-k_T jets, used in the nominal analysis, and a selection of CA jets. For the selection with the CA jets, an approach described in [16] was taken. Subjets within a CA jet, which are constructed by reversal of the clustering of the jet, were used to reconstruct the Higgs boson. This procedure has been stated to be very promising for the search of a Higgs boson in the boosted regime of the ZH and WH channel [16]. The signal yields for the highest p_T^Z bin of the analysis ($p_T^Z > 200\,\text{GeV}$) have been taken into consideration. The yields from the selection of CA has been found to be $\sim 27\%$ lower than the yield from the selection of anti-k_T jets. This indicates, that using only CA instead of anti-k_T jets may not give an improvement to the analysis. By combining the selections for the two jet types, however, an increase of $\sim$ 19 - 22% for signal events has been found. Thus a combination of these two jet types to improve the analysis could be taken into consideration. The background yield, however, has been found to also increase by $\sim$ 128 - 131%. To test if the implementation of CA jets for the boosted Higgs regime gives an improvement to the analysis, the likelihood fit was performed by including an additional region in the last p_T^Z bin for the selection of CA jets. Since the selection of CA jets cannot be separated into a 2-jet and 3-jet region, the fit had to be performed with a combined 2-jet and 3-jet signal region. The results from performing this fit show no significant improvement for the implementation of CA jets in the boosted Higgs regime, neither by the combined approach nor by using only CA jets. This allows for the conclusion, that anti-k_T jets are sufficient for the Higgs boson search in the $ZH \to l\bar{l}b\bar{b}$ channel in the highest p_T^Z bin, and the analysis does not significantly improve by the implementation of the approach with CA jets described in [16].

The Higgs production channel with an associated vectorboson (either W or Z) is one of the most promising channels to observe direct coupling of the Higgs boson to fermions at the LHC. The signal yield for the $ZH \to l\bar{l}b\bar{b}$ channel is smaller than for the production with an associated W boson, since the production cross-section for the WH channel is about 10 times larger than for the ZH channel. But the $ZH \to l\bar{l}b\bar{b}$ channel has a much cleaner signature, due to the high suppression of the backgrounds coming from $t\bar{t}$ and multijet events, which still makes it a very interesting channel to study. The combination of these two channels, and additionally the ZH channel, where the Z boson decays into neutrinos, already gives very promising results in observing the direct coupling of the Higgs boson to

fermions. With the anticipated integrated luminosity after the current shutdown of the LHC, an observation of the Higgs boson in the $H \to b\bar{b}$ channel is very much to be expected.

Bibliography

[1] David Griffiths. *Introduction to Elementary Particles*. John Wiley & Sons, 1987.

[2] Joern Bleck-Neuhaus. *Elementare Teilchen - Moderne Physik Von Den Atomen Bis Zum Standard-Modell*. Springer DE, 2010.

[3] Picture of elementary particles in the standard model. http://en.wikipedia.org/wiki/File:Standard_Model_of_Elementary_Particles.svg. Accessed: 2013-09-10.

[4] Eric W Weisstein. "group generators." from mathworld – a wolfram web resource. http://mathworld.wolfram.com/GroupGenerators.html. Accessed: 2013-09-10.

[5] Francis Halzen and Alan D. Martin. *QUARK & LEPTONS: AN INTRODUCTORY COURSE IN MODERN PARTICLE PHYSICS*. John Wiley & Sons, 1984.

[6] Chris Quigg. Unanswered Questions in the Electroweak Theory. *Ann.Rev.Nucl.Part.Sci.*, 59:505–555, 2009.

[7] S. Dittmaier et al. Handbook of LHC Higgs Cross Sections: 1. Inclusive Observables. 2011.

[8] S Heinemeyer et al. Handbook of LHC Higgs Cross Sections: 3. Higgs Properties. 2013.

[9] The ATLAS Collaboration. Observation of a new particle in the search for the standard model higgs boson with the atlas detector at the lhc. Phys.Lett. B716 (2012) 1-29, 2012.

[10] Search for the bb decay of the standard model higgs boson in associated w/zh production with the atlas detector. Technical Report ATLAS-CONF-2013-079, CERN, Geneva, Juli 2013.

[11] C Lefevre. Lhc: the guide (english version). guide du lhc (version anglaise). Feb 2009.

[12] Lyndon Evans and Philip Bryant. LHC Machine. *JINST*, 3:S08001, 2008.

[13] Cern homepage. http://home.web.cern.ch/about. Accessed: 2013-08-01.

[14] G. Aad et al. The ATLAS Experiment at the CERN Large Hadron Collider. *JINST*, 3:S08003, 2008.

[15] G. Aad et al. Expected Performance of the ATLAS Experiment - Detector, Trigger and Physics. 2009.

[16] Jonathan M. Butterworth, Adam R. Davison, Mathieu Rubin, and Gavin P. Salam. Jet substructure as a new Higgs search channel at the LHC. *Phys.Rev.Lett.*, 100:242001, 2008.

[17] Matteo Cacciari, Gavin P. Salam, and Gregory Soyez. The Anti-k(t) jet clustering algorithm. *JHEP*, 0804:063, 2008.

[18] Torbjorn Sjostrand, Stephen Mrenna, and Peter Z. Skands. A Brief Introduction to PYTHIA 8.1. *Comput.Phys.Commun.*, 178:852–867, 2008.

[19] Paolo Nason. A New method for combining NLO QCD with shower Monte Carlo algorithms. *JHEP*, 0411:040, 2004.

[20] Borut Paul Kersevan and Elzbieta Richter-Was. The Monte Carlo event generator AcerMC versions 2.0 to 3.8 with interfaces to PYTHIA 6.4, HERWIG 6.5 and ARIADNE 4.1. *Comput.Phys.Commun.*, 184:919–985, 2013.

[21] G. Corcella, I.G. Knowles, G. Marchesini, S. Moretti, K. Odagiri, et al. HERWIG 6: An Event generator for hadron emission reactions with interfering gluons (including supersymmetric processes). *JHEP*, 0101:010, 2001.

[22] T. Gleisberg, Stefan. Hoeche, F. Krauss, M. Schonherr, S. Schumann, et al. Event generation with SHERPA 1.1. *JHEP*, 0902:007, 2009.

[23] Glen Cowan, Kyle Cranmer, Eilam Gross, and Ofer Vitells. Asymptotic formulae for likelihood-based tests of new physics. *Eur.Phys.J.*, C71:1554, 2011.

Appendix A

MC Samples

The following MC samples were used in the analysis described in this thesis:

Sample	Name	Cross-section	k-factor	Filter-efficiency
161824	Pythia8_AU2CTEQ6L1_ZH110_llbb	0.04409	1.0	1.0
161825	Pythia8_AU2CTEQ6L1_ZH115_llbb	0.03632	1.0	1.0
161826	Pythia8_AU2CTEQ6L1_ZH120_llbb	0.02933	1.0	1.0
161827	Pythia8_AU2CTEQ6L1_ZH125_llbb	0.02297	1.0	1.0
161828	Pythia8_AU2CTEQ6L1_ZH130_llbb	0.01732	1.0	1.0
161829	Pythia8_AU2CTEQ6L1_ZH135_llbb	0.01254	1.0	1.0
161830	Pythia8_AU2CTEQ6L1_ZH140_llbb	0.00868	1.0	1.0
161831	Pythia8_AU2CTEQ6L1_ZH145_llbb	0.00568	1.0	1.0
161832	Pythia8_AU2CTEQ6L1_ZH150_llbb	0.00342	1.0	1.0
167749	Sherpa_CT10_ZeeMassiveCBPt0_BFilter	1110	1.12	0.027969
167750	Sherpa_CT10_ZeeMassiveCBPt0_CFilterBVeto	1109.6	1.12	0.28322
167751	Sherpa_CT10_ZeeMassiveCBPt0_CVetoBVeto	1108.7	1.12	0.68824
167752	Sherpa_CT10_ZmumuMassiveCBPt0_BFilter	1110	1.12	0.02796
167753	Sherpa_CT10_ZmumuMassiveCBPt0_CFilterBVeto	1110.3	1.12	0.28353
167754	Sherpa_CT10_ZmumuMassiveCBPt0_CVetoBVeto	1109	1.12	0.68892
167755	Sherpa_CT10_ZtautauMassiveCBPt0_BFilter	1110	1.12	0.027935
167756	Sherpa_CT10_ZtautauMassiveCBPt0_CFilterBVeto	1110.1	1.12	0.2833
167757	Sherpa_CT10_ZtautauMassiveCBPt0_CVetoBVeto	1109.4	1.12	0.68928
180543	Sherpa_CT10_ZeeMassiveCBPt40_70_BFilter	70.493	1.12	0.070638
180544	Sherpa_CT10_ZeeMassiveCBPt40_70_CFilterBVeto	70.53	1.12	0.34197
180545	Sherpa_CT10_ZeeMassiveCBPt40_70_CVetoBVeto	70.431	1.12	0.58761
180546	Sherpa_CT10_ZmumuMassiveCBPt40_70_BFilter	70.511	1.12	0.070707

Table A.1

Sample	Name	Cross-section	k-factor	Filter-efficiency
180547	Sherpa_CT10_ZmumuMassiveCBPt40_70_CFilterBVeto	70.469	1.12	0.34141
180548	Sherpa_CT10_ZmumuMassiveCBPt40_70_CVetoBVeto	70.534	1.12	0.58768
180549	Sherpa_CT10_ZtautauMassiveCBPt40_70_BFilter	70.441	1.12	0.070859
180550	Sherpa_CT10_ZtautauMassiveCBPt40_70_CFilterBVeto	70.538	1.12	0.34163
180551	Sherpa_CT10_ZtautauMassiveCBPt40_70_CVetoBVeto	70.528	1.12	0.58755
167797	Sherpa_CT10_ZeeMassiveCBPt70_140_BFilter	29.494	1.12	0.082517
167798	Sherpa_CT10_ZeeMassiveCBPt70_140_CFilterBVeto	29.487	1.12	0.35497
167799	Sherpa_CT10_ZeeMassiveCBPt70_140_CVetoBVeto	29.491	1.12	0.56262
167800	Sherpa_CT10_ZmumuMassiveCBPt70_140_BFilter	29.491	1.12	0.082585
167801	Sherpa_CT10_ZmumuMassiveCBPt70_140_CFilterBVeto	29.447	1.12	0.35488
167802	Sherpa_CT10_ZmumuMassiveCBPt70_140_CVetoBVeto	29.521	1.12	0.56196
167803	Sherpa_CT10_ZtautauMassiveCBPt70_140_BFilter	29.489	1.12	0.082563
167804	Sherpa_CT10_ZtautauMassiveCBPt70_140_CFilterBVeto	29.499	1.12	0.35509
167805	Sherpa_CT10_ZtautauMassiveCBPt70_140_CVetoBVeto	29.494	1.12	0.56247
167809	Sherpa_CT10_ZeeMassiveCBPt140_280_BFilter	3.9901	1.12	0.095235
167810	Sherpa_CT10_ZeeMassiveCBPt140_280_CFilterBVeto	3.9811	1.12	0.36919
167811	Sherpa_CT10_ZeeMassiveCBPt140_280_CVetoBVeto	3.989	1.12	0.53431
167812	Sherpa_CT10_ZmumuMassiveCBPt140_280_BFilter	3.9842	1.12	0.095389
167813	Sherpa_CT10_ZmumuMassiveCBPt140_280_CFilterBVeto	3.9911	1.12	0.36999
167814	Sherpa_CT10_ZmumuMassiveCBPt140_280_CVetoBVeto	3.9841	1.12	0.53441
167815	Sherpa_CT10_ZtautauMassiveCBPt140_280_BFilter	3.9878	1.12	0.095807
167816	Sherpa_CT10_ZtautauMassiveCBPt140_280_CFilterBVeto	3.988	1.12	0.36953
167817	Sherpa_CT10_ZtautauMassiveCBPt140_280_CVetoBVeto	3.9871	1.12	0.53328
167821	Sherpa_CT10_ZeeMassiveCBPt280_500_BFilter	0.24182	1.12	0.10851
167822	Sherpa_CT10_ZeeMassiveCBPt280_500_CFilterBVeto	0.24128	1.12	0.38744
167823	Sherpa_CT10_ZeeMassiveCBPt280_500_CVetoBVeto	0.24158	1.12	0.50617
167824	Sherpa_CT10_ZmumuMassiveCBPt280_500_BFilter	0.24219	1.12	0.10802
167825	Sherpa_CT10_ZmumuMassiveCBPt280_500_CFilterBVeto	0.24169	1.12	0.38643
167826	Sherpa_CT10_ZmumuMassiveCBPt280_500_CVetoBVeto	0.24272	1.12	0.50549
167827	Sherpa_CT10_ZtautauMassiveCBPt280_500_BFilter	0.2412	1.12	0.10653
167828	Sherpa_CT10_ZtautauMassiveCBPt280_500_CFilterBVeto	0.24102	1.12	0.38481
167829	Sherpa_CT10_ZtautauMassiveCBPt280_500_CVetoBVeto	0.24147	1.12	0.5072
167833	Sherpa_CT10_ZeeMassiveCBPt500_BFilter	0.013235	1.12	0.11573

Table A.2

Sample	Name	Cross-section	k-factor	Filter-efficiency
167834	Sherpa_CT10_ZeeMassiveCBPt500_CFilterBVeto	0.013454	1.12	0.39846
167835	Sherpa_CT10_ZeeMassiveCBPt500_CVetoBVeto	0.013307	1.12	0.4848
167836	Sherpa_CT10_ZmumuMassiveCBPt500_BFilter	0.013161	1.12	0.11408
167837	Sherpa_CT10_ZmumuMassiveCBPt500_CFilterBVeto	0.01348	1.12	0.39857
167838	Sherpa_CT10_ZmumuMassiveCBPt500_CVetoBVeto	0.013264	1.12	0.48689
167839	Sherpa_CT10_ZtautauMassiveCBPt500_BFilter	0.013231	1.12	0.11524
167840	Sherpa_CT10_ZtautauMassiveCBPt500_CFilterBVeto	0.013308	1.12	0.39316
167841	Sherpa_CT10_ZtautauMassiveCBPt500_CVetoBVeto	0.013284	1.12	0.48562
117050	PowhegPythia_P2011C_ttbar	238.06	1.0	0.54298
110101	AcerMCPythia_P2011CCTEQ6L1_singletop_tchan_l	87.76	1.0	0.324
110119	PowhegPythia_P2011C_st_schan_lep	5.61	1.0	0.324
110140	PowhegPythia_P2011C_st_Wtchan_incl_DR	22.37	1.0	1.0
161996	Herwig_AUET2CTEQ6L1_WZ_NoLeptonFilter	22.6942	1.0	1.0
169492	Herwig_AUET2CTEQ6L1_ZZ_LepEF_METVeto	7.697	1.0	0.16491

Table A.3

Erklärung:

Hiermit erkläre ich, die vorliegende Arbeit selbständig verfasst zu haben und keine anderen als die in der Arbeit angegebenen Quellen und Hilfsmittel benutzt zu haben.

München, 26. September 2013

_____